

**New Arsenides and Antimonides as
Thermoelectric Materials and
Chalcogenides with Distorted Square Nets**

Hong Xu

A thesis
presented to the University of Waterloo
in fulfillment of the
thesis requirement for the degree of
Doctor of Philosophy
in
Chemistry

Waterloo, Ontario, Canada, 2010

©Hong Xu 2010

AUTHOR'S DECLARATION

I hereby declare that I am the sole author of this thesis. This is a true copy of the thesis, including any required final revisions, as accepted by my examiners.

I understand that my thesis may be made electronically available to the public.

Signature:

Abstract

Thermoelectric (TE) materials can be ranked by their figure-of-merit, ZT , which is defined as $ZT = (S^2\sigma T)/\kappa$. Herein, T is the average temperature between the cold (T_C) and hot sides (T_H) of the thermoelectric device, S is the Seebeck coefficient, σ and κ are electrical and thermal conductivity, respectively. Presently, the applications of TE devices are limited by their low energy conversion efficiencies. The energy conversion efficiency includes the Carnot term $[(T_H - T_C)/T_C]$, an unattainable upper limit of efficiency for any real system, and a loss term, which depends on the ZT value. A larger temperature difference will produce a larger Carnot efficiency, and a higher ZT value will improve the loss efficiency. Thus, the combination of a larger temperature difference and higher ZT will lead to higher energy conversion efficiency, e.g. with $ZT = 1$, $T_H = 1000$ K, $T_C = 300$ K, the efficiency can reach 17%. It is therefore important to explore TE materials that can be used at high temperatures (around 1000 K). Unfortunately there are very few materials that are stable and efficient under such strict conditions.

Our group commenced an investigation of the Ir_3Ge_7 family materials in the late 1990s. My thesis work had been focused on the synthesis and optimization of $\text{Mo}_3\text{Sb}_{7-x}\text{Te}_x$ and $\text{Re}_3(\text{Si}, \text{Ge}, \text{Sn}, \text{Pb})_x\text{As}_{7-x}$, the ternary substitution variants of Mo_3Sb_7 and Re_3As_7 . They exhibited the semiconductivity by partial Sb/Te or (Si, Ge, Sn, Pb)/As exchange, as predicted by electronic structure calculations (linear muffin-tin orbital method) and confirmed by physical property measurements. Furthermore, some transition metal atoms with the proper size, such as Fe, Co, Ni, and Cu, were intercalated into the existing cubic voids of the crystal structure in an attempt to reduce the phonon conductivity. Rietveld refinements using GSAS software were employed to analyze the

(Si, Sn, Pb)/As ordering and distribution preference. Partial characterizations were conducted at University of Waterloo on cold-pressed pellets. The high temperature measurements were performed on hot-pressed pellets at Clemson University.

Another project I worked on was about how to open a band gap by changing the bonding interactions. Some compounds containing the layered square nets structure may behave like a metal or like a semimetal. A band gap can be opened by distorting the square net into less symmetric layers, containing cis–trans or zig–zag chains, resulting in changes of the electronic structure around the Fermi level, therefore widening or opening a band gap. In some pnictide compounds, regular planar square nets of pnictogen atoms with half (“hypervalent” one-electron) bonding are prone to undergo Peierls distortions. Such materials are of great interest for thermoelectric energy conversion because the narrow band gap is advantageous for high-performance thermoelectric properties. The ternary and quaternary chalcogenides, LaAsSe and LaCu_xAsSe, were prepared and investigated in this thesis. Seebeck coefficient measurements proved they are semiconductors. Rietveld refinements indicated the As atoms adopt a cis-trans distortion, which changes the structure type from ZrSiS (space group *P4/nmm*) to GdPS (space group *Pnma*). Consequently, a band gap is opened, in accordance with the electronic structure calculation. Single crystal structure determination showed LaCu_{0.12(1)}AsSe adopts a derivative structure of the ZrSiS type, with deficient Cu sites inserted between La and As layers. The refinement based on As split sites is preferred.

Acknowledgements

At first, I absolutely pass my deepest gratitude to my supervisor, Prof. Holger Kleinke for his significant support in the past four years. I learned not only solid state chemistry knowledge, but also his dedication to research. I appreciate his great patience to guide me from the beginning till now. And I know he is always there when I need his advice. I cannot reach this step without his help.

I am heartily thankful to our department crystallographer, Dr. Jalil Assoud, who was postdoctoral member in our group when I joined the group. I built my knowledge on keeping bother him at the beginning. Thank you, Jalil. I am very grateful to thank our group research associate, Katja Kleinke. She is always very readily to help everyone in the group. Her excellent research ability and organization skills enable us to work comfortably and efficiently. I also would like to thank our previous member, Dr. Navid Soheilnia, who helped me a lot when I joined the group.

I am indebted to many of my colleagues and friends. I thank Jackie, Yanjie Tingting (they are all previous group members) and Bryan, Savitree, and Mayasree for their everlasting support and friendship. I thank all the postdoctoral fellows in our group, Dr. Raj Sankar, Dr. Michael Guch and Dr. Mariya Zelinska. It is my pleasure to work with so many wonderful people and all of you made my study life so memorable.

The last but not the least, I would like to express appreciation to my advisory committee members, Prof. Nazar, Prof. Lee and Prof. Preuss, for their consistently valuable suggestions and support during the past four years. I also appreciate my external examiner Prof. Mar and internal-external examiner Prof. Hawthorn, for their precious time to review my thesis and attend my defense.

Table of Contents

AUTHOR'S DECLARATION	ii
Abstract	iii
Acknowledgements	v
Table of Contents	vi
List of Figures	ix
List of Tables	xii
1 Introduction to thermoelectrics.....	1
1.1 Thermoelectric phenomena	1
1.2 Thermoelectric modules and application.....	4
1.3 Parameters involved in TE research	7
1.3.1 Figure-of-merit (ZT) and thermoelectric efficiency	7
1.3.2 Seebeck Coefficient.....	9
1.3.3 Electrical conductivity.....	10
1.3.4 Thermal conductivity.....	12
1.4 Developments in thermoelectric materials	13
1.4.1 Chalcogenides	14
1.4.2 Antimonides	17
1.4.3 Nanostructured bulk thermoelectric materials.....	19
1.4.4 Research background and objectives.....	22
2 Experimental techniques and physical property measurements	25
2.1 Synthetic methods	25
2.1.1 Solid-state reaction	25
2.1.2 Flux method.....	26
2.1.3 Chemical vapor transport	28
2.1.4 Experimental synthesis.....	29
2.2 Analysis techniques	30
2.2.1 Fundamentals of X-ray diffraction	31
2.2.2 Single crystal methods.....	35
2.2.3 Powder X-ray diffraction.....	38
2.2.4 Energy dispersive X-ray (EDX) analysis	42
2.2.5 Thermal analysis.....	44
2.2.6 Electronic structure calculation	46
2.2.7 Seebeck coefficient measurement	50

2.2.8	Electrical conductivity measurement.....	52
2.2.9	Power factor measuring system.....	54
2.2.10	Thermal conductivity measurement.....	55
2.3	Physical properties measurement at Clemson University.....	57
3	Thermoelectric properties of Mo_3Sb_7 series samples.....	58
3.1	Sample synthesis.....	58
3.2	Crystal structure.....	59
3.3	Investigation of $\text{Ni}_y\text{Mo}_3\text{Sb}_{7-x}\text{Te}_x$ and $\text{Fe}_{0.05}\text{Mo}_3\text{Sb}_{7-x}\text{Te}_x$	61
3.3.1	Rietveld refinement.....	61
3.3.2	Electronic structure calculations.....	62
3.3.3	Physical properties.....	66
3.4	Investigation of $A_{0.05}\text{Mo}_3\text{Sb}_{5.4}\text{Te}_{1.6}$ ($A = \text{Mn, Fe, Co, Ni}$).....	75
3.4.1	Electron Microscopy.....	76
3.4.2	Physical properties.....	78
3.4.3	Thermal analysis.....	82
4	Thermoelectric properties of Re_3As_7 series samples.....	85
4.1	Sample synthesis.....	85
4.2	Crystal structure.....	87
4.3	Rietveld refinements.....	87
4.3.1	Rietveld refinements on $\text{Re}_3\text{Sn}_x\text{As}_{7-x}$	87
4.3.2	Rietveld refinements on $\text{Re}_3E_x\text{As}_{7-x}$ ($E = \text{Si, Pb}$) and $\text{Mo}_{0.1}\text{Re}_{2.9}\text{As}_7$	91
4.4	Electronic structure calculation.....	94
4.5	Physical property measurements.....	98
4.5.1	$\text{Re}_3(\text{Sn,As})_7$ series samples.....	98
4.5.2	$\text{Re}_3(\text{Si, As})_7$, $\text{Re}_3(\text{Pb, As})_7$ and $(\text{Mo,Re})_3\text{As}_7$ series samples.....	104
5	LaAsSe and LaCu_xAsSe with the distorted square nets.....	106
5.1	Introduction of different structure types.....	106
5.2	Sample preparation.....	109
5.3	Characterization of lanthanum pnictide chalcogenide compounds.....	110
5.3.1	Determination of the properties of LaSbTe	110
5.3.2	LaAsSe	111
5.3.3	LaCu_xAsSe	114
6	Conclusions.....	120
	Appendix A.....	123

Bibliography 127

List of Figures

Fig. 1.1 Seebeck effect for power generation (left) and Peltier effect for cooling (right). ⁶	3
Fig. 1.2 Direction of charge flow in thermoelectric module. ⁷	4
Fig. 1.3 Waste heat harvesting from exhaust system of a vehicle through TEG device. ⁸	5
Fig. 1.4 Illustration of thermoelectric ambient energy harvester. ⁹	6
Fig. 1.5 A scheme of radioactive thermoelectric generator (RTG). ¹⁰	7
Fig. 1.6 Comparison of thermoelectric parameters between insulator, semiconductor and metal. ¹¹	8
Fig. 1.7 Crystal structure of CsBi ₄ Te ₆ .	15
Fig. 1.8 Crystal structure of Tl ₉ BiTe ₆ (left, Bi/Tl mixed occupy 4c site, grey spheres) and Tl ₂ SnTe ₅ (right).	16
Fig. 1.9 Crystal structure of skutterudite, where a guest atom occupies the center of void.	18
Fig. 1.10 Crystal structure of Yb ₁₄ MnSb ₁₁ .	19
Fig. 1.11 Comparison of figure-of-merit between current state-of-art bulk thermoelectric materials and nanostructured thermoelectric materials. ¹⁹	21
Fig. 1.12 Crystal structure of Ir ₃ Ge ₇ .	22
Fig. 2.1 Scheme of chemical vapor transport in a closed tube. Transport is from temperature T ₂ to T ₁ (T ₂ > T ₁).	29
Fig. 2.2 Steps for sample preparation. (a) glove box; (b) vacuum line; (c) H ₂ /O ₂ torch; (d) sealed tubes; (e) resistance furnace.	30
Fig. 2.3 The derivation of Bragg's law.	33
Fig. 2.4 SMART Apex CCD in the Department of Chemistry, Waterloo.	36
Fig. 2.5 The formation of a cone of diffracted beams in PXRD.	39
Fig. 2.6 Inel XRG 3000 powder X-ray diffractometer.	40
Fig. 2.7 An example of EDX spectrum.	43
Fig. 2.8 (a) NETZSCH STA 409PC Luxx apparatus; (b) DSC head within furnace.	44
Fig. 2.9 Schematic drawing of DSC curve for endothermic and exothermic reactions.	45
Fig. 2.10 Density of States (DOS) of a metal (left) and an insulator (right). The occupied levels are shown by shading.	50
Fig. 2.11 (a) Programmable Seebeck controller (SB-100) and temperature controller (K-20); (b) Seebeck system dewar with MMR cold stage mounted on the top.	50
Fig. 2.12 Picture of Seebeck stage.	51
Fig. 2.13 Homemade electrical conductivity measurement apparatus.	53
Fig. 2.14 Schematic drawing for four-point measurement method.	53

Fig. 2.15 (a) ULVAC ZEM-3 measuring system; (b) the sample placed between the electrodes with two probes contacts.....	54
Fig. 2.16 conceptual diagram for measurement of voltage and temperature differences.....	55
Fig. 2.17 Flash Line 3000 for thermal diffusivity measurement.....	56
Fig. 3.1 Crystal structure of $A_y\text{Mo}_3\text{Sb}_{7-x}\text{Te}_x$ (left) and its chains (right).....	60
Fig. 3.2 Rietveld refinement of $\text{Ni}_{0.10}\text{Mo}_3\text{Sb}_{5.5}\text{Te}_{1.5}$	62
Fig. 3.3 Density of states of Mo_3Sb_7 (left), $\text{Mo}_3\text{Sb}_{5.5}\text{Te}_{1.5}$ (center) and $\text{Mo}_3\text{Sb}_5\text{Te}_2$ (right); the dashed line represents Fermi level.	64
Fig. 3.4 Density of states of $\text{Fe}_{0.125}\text{Mo}_3\text{Sb}_5\text{Te}_2$ (left) and $\text{Ni}_{0.125}\text{Mo}_3\text{Sb}_5\text{Te}_2$ (right).	66
Fig. 3.5 Electrical conductivity of $\text{Ni}_y\text{Mo}_3\text{Sb}_{7-x}\text{Te}_x$	67
Fig. 3.6 Electrical conductivity of $\text{Fe}_{0.05}\text{Mo}_3\text{Sb}_{7-x}\text{Te}_x$	68
Fig. 3.7 Seebeck coefficient of $\text{Ni}_y\text{Mo}_3\text{Sb}_{7-x}\text{Te}_x$	69
Fig. 3.8 Seebeck coefficient of $\text{Fe}_{0.05}\text{Mo}_3\text{Sb}_{7-x}\text{Te}_x$	70
Fig. 3.9 Power factor (P.F.) of $\text{Ni}_y\text{Mo}_3\text{Sb}_{7-x}\text{Te}_x$	71
Fig. 3.10 Power factor (P.F.) of $\text{Fe}_{0.05}\text{Mo}_3\text{Sb}_{7-x}\text{Te}_x$	72
Fig. 3.11 Thermal conductivity of $\text{Ni}_y\text{Mo}_3\text{Sb}_{7-x}\text{Te}_x$	73
Fig. 3.12 Thermal conductivity of $\text{Fe}_{0.05}\text{Mo}_3\text{Sb}_{7-x}\text{Te}_x$	73
Fig. 3.13 Figure of merit (ZT) of $\text{Ni}_y\text{Mo}_3\text{Sb}_{7-x}\text{Te}_x$	74
Fig. 3.14 Figure of merit (ZT) of $\text{Fe}_{0.05}\text{Mo}_3\text{Sb}_{7-x}\text{Te}_x$	75
Fig. 3.15 SEM map screens of different elements of $\text{Ni}_{0.05}\text{Mo}_3\text{Sb}_{5.4}\text{Te}_{1.6}$	77
Fig. 3.16 TEM images of $\text{Ni}_{0.05}\text{Mo}_3\text{Sb}_{5.4}\text{Te}_{1.6}$	77
Fig. 3.17 Electrical conductivity of $A_{0.05}\text{Mo}_3\text{Sb}_{5.4}\text{Te}_{1.6}$ ($A = \text{Mn, Fe, Co, Ni}$) and $\text{Mo}_3\text{Sb}_{5.4}\text{Te}_{1.6}$. ..	78
Fig. 3.18 Seebeck coefficient of $A_{0.05}\text{Mo}_3\text{Sb}_{5.4}\text{Te}_{1.6}$ ($A = \text{Mn, Fe, Co, Ni}$) and $\text{Mo}_3\text{Sb}_{5.4}\text{Te}_{1.6}$	79
Fig. 3.19 Power factor (P.F.) of $A_{0.05}\text{Mo}_3\text{Sb}_{5.4}\text{Te}_{1.6}$ ($A = \text{Mn, Fe, Co, Ni}$) and $\text{Mo}_3\text{Sb}_{5.4}\text{Te}_{1.6}$	80
Fig. 3.20 Thermal conductivity of $A_{0.05}\text{Mo}_3\text{Sb}_{5.4}\text{Te}_{1.6}$ ($A = \text{Mn, Fe, Co, Ni}$) and $\text{Mo}_3\text{Sb}_{5.4}\text{Te}_{1.6}$	81
Fig. 3.21 Figure of merit ZT of $A_{0.05}\text{Mo}_3\text{Sb}_{5.4}\text{Te}_{1.6}$ ($A = \text{Mn, Fe, Co, Ni}$) and $\text{Mo}_3\text{Sb}_{5.4}\text{Te}_{1.6}$	82
Fig. 3.22 DSC curves of $\text{Ni}_{0.05}\text{Mo}_3\text{Sb}_{5.4}\text{Te}_{1.6}$ and Mo_3Sb_7	83
Fig. 3.23 Comparison of ZT values of three p -type thermoelectric materials.	84
Fig. 4.1 Crystal structure of Re_3As_7 . $E2$ presents As_2 , where can be partially occupied by Si, Ge, Sn and Pb	87
Fig. 4.2 Rietveld refinement on $\text{Re}_3\text{Sn}_{0.1}\text{As}_{6.9}$	88
Fig. 4.3 Sn composition dependence of the lattice parameter a (Å).	90
Fig. 4.4 Rietveld refinement on $\text{Re}_3\text{Si}_{0.1}\text{As}_{6.9}$	92
Fig. 4.5 Rietveld refinement on $\text{Re}_3\text{Pb}_{0.06}\text{As}_{6.94}$	93

Fig. 4.6 Rietveld refinement on $\text{Mo}_{0.1}\text{Re}_{2.9}\text{As}_7$.	93
Fig. 4.7 Density of States (DOS) of Re_3As_7 , Re_3SnAs_6 and $\text{Ni}_{0.5}\text{Re}_3\text{SnAs}_6$. The Fermi level E_F (dashed horizontal line) was arbitrarily placed at 0 eV.	95
Fig. 4.8 Sn ordering of five models for Re_3SnAs_5 . Sn: grey; As1: red (in model I and II); As2: pink (in model III, IV and V).	96
Fig. 4.9 The corresponding density of states of five models for Re_3SnAs_6 .	97
Fig. 4.10 Density of states of $\text{Re}_3\text{Pb}_{0.5}\text{As}_{6.5}$, Re_3PbAs_6 , $\text{Mo}_{0.5}\text{Re}_{2.5}\text{As}_7$ and MoRe_2As_7 .	97
Fig. 4.11 Temperature dependence of the Seebeck coefficient of selected cold-pressed arsenides.	99
Fig. 4.12 High-temperature measurements of Seebeck coefficient and electrical conductivity of hot-pressed $\text{Re}_3\text{Sn}_{0.2}\text{As}_{6.8}$.	100
Fig. 4.13 Thermal analysis of $\text{Re}_3\text{Sn}_{0.2}\text{As}_{6.8}$.	101
Fig. 4.14 Comparison of high temperature XRD patterns of $\text{Re}_3\text{Sn}_{0.3}\text{As}_{6.7}$.	102
Fig. 4.15 Comparison of power factors of $\text{Re}_3\text{Sn}_{0.2}\text{As}_{6.8}$, Re_3GeAs_6 and $\text{Re}_3\text{Ge}_{0.6}\text{As}_{6.4}$.	103
Fig. 4.16 Seebeck coefficient measurement for $\text{Re}_3(\text{SiAs})_7$ variants.	104
Fig. 4.17 Seebeck coefficient of $\text{Re}_3(\text{PbAs})_7$ variants (left) and $\text{Mo}_{0.1}\text{Re}_{2.9}\text{As}_7$ (right).	105
Fig. 5.1 Regular square net structures: ZrSiS (left) and HfCuSi_2 (right).	107
Fig. 5.2 Crystal structure of NbPS with distorted P layers.	108
Fig. 5.3 Crystal structure of CeAsS (left) and GdPS (right) with distorted square nets, contacts between Ce-As and Gd-P are not shown for clarity.	108
Fig. 5.4 Band structure (left) and Seebeck coefficient (right) of LaSbTe .	111
Fig. 5.5 Crystal structure of LaAsSe : left, along a axis; right, along c axis. La coordination environment is shown by the green polyhedron. La-As contacts are removed for clarity.	113
Fig. 5.6 DOS (left) and Seebeck coefficient (right) of LaAsSe .	114
Fig. 5.7 Crystal structure view of $\text{LaCu}_{0.12(1)}\text{AsSe}$: left, along the b axis; right, along the c axis. Dashed lines represent As-As hypervalent bonds.	116
Fig. 5.8 Left: crystal structure view of $\text{LaCu}_{0.12(1)}\text{AsSe}$ with As split sites (along the b axis); right: view of As layer surrounded by Cu atom (along the c axis).	117
Fig. 5.9 View of a possible ordered As layer with the surrounding Cu atoms along the c axis (pink: As atoms; blue: Cu atoms).	118
Fig. 5.10 Seebeck coefficient of $\text{LaCu}_{0.1}\text{AsSe}$.	119

List of Tables

Tab. 3.1 Rietveld refinement results of $\text{Ni}_{0.10}\text{Mo}_3\text{Sb}_{5.5}\text{Te}_{1.5}$	62
Tab. 4.1 Reaction list for preparation single crystals of $\text{Re}_3\text{Sn}_x\text{As}_{7-x}$	86
Tab. 4.2 Residual factors and refined Sn occupancies for both sites (12 <i>d</i> and 16 <i>f</i>).....	89
Tab. 4.3 Interatomic distances (Å) and lattice parameter (Å) of $\text{Re}_3\text{Sn}_x\text{As}_{7-x}$	91
Tab. 4.4 Residual factors and refined <i>E</i> occupancies on preferred site.....	94
Tab. 4.5 Comparison of Seebeck coefficient and electrical conductivity at 300 K.	98
Tab. 5.1 Comparison of ratios of long to short bond distance in the distorted square nets.	109
Tab. 5.2 Atomic positions and displacement parameters (Å ²) of LaAsSe.	112
Tab. 5.3 Atomic positions and displacement parameters (Å ²) of $\text{LaCu}_{0.12(1)}\text{AsSe}$ ($U_{11} = U_{22}$)....	115
Tab. 5.4 Atomic positions and displacement parameters (Å ²) of $\text{LaCu}_{0.12(1)}\text{AsSe}$ in As split sites model (U_{22} is equal to U_{11}).....	117
Tab. A.1 Crystallographic data for LaAsSe.....	123
Tab. A.2 Bond distances (Å) of LaAsSe.....	124
Tab. A.3 Crystallographic data for $\text{LaCu}_{0.12(1)}\text{AsSe}$	125
Tab. A.4 Comparison of selected bond distances (Å) of $\text{LaCu}_{0.12(1)}\text{AsSe}$ in square net model and split site model.	126

1 Introduction to thermoelectrics

With the current fossil fuel supply depletion and global warming caused by greenhouse gas emission, the need for renewable energy has sparked numerous research projects on alternative energy sources and developing diverse energy conversion techniques. Thermoelectric materials attract intensive interest with their potential to convert heat to electricity with temperature gradient or be used as a heat pump for electrical cooling when a voltage is applied. Any available heat sources from automotive exhaust or industrial processes could be converted to electricity by the thermoelectric technique. Some automotive companies, such as GM¹ and BMW², have worked on thermoelectric-based waste heat recovery to reduce fuel consumption. However the applications of thermoelectrics have been restricted for a long time due to their low efficiency (η), which depends on the working temperature difference and figure-of-merit (ZT) of materials. Therefore, exploring new thermoelectric materials or optimizing the existing bulk materials to achieve high efficiency is one of major challenges in this research field. Despite their low efficiency, thermoelectric devices have already been widely used in spacecrafts, medical devices and portable fridges, where reliability is more important than efficiency.

1.1 Thermoelectric phenomena

The thermoelectric effect originates from free moving of charge carrier in metals and semiconductors. These charge carriers also carry heat while moving. When a temperature differential is applied across the material, the charge carriers on the hot side tend to move to the cold side producing an electrical potential. An equilibrium will be reached between the

diffusion potential and electrostatic repulsion of accumulating charge carriers. This property is known as Seebeck effect, which is the basis of direct conversion of temperature difference to electric potential. Thermoelectric effects commonly comprise three separate terms: the Seebeck effect, Peltier effect and Thomson effect.

Thomas Johann Seebeck firstly discovered thermoelectricity in 1821.³ He found that a compass needle deflected if it was placed in the vicinity of a closed loop, composed of two dissimilar metals, when different temperatures were applied to the junctions of both sides of metals. This phenomenon described a voltage difference (ΔV) created by temperature difference (ΔT) between the two different materials. He also observed that the magnitude of deflection was proportional to the temperature gradient and depended on the types of materials. This relation was later defined as the Seebeck coefficient (S) or thermopower, as shown in equation (1-1). Experimental results demonstrate that metals usually present a very low Seebeck coefficient, as a few $\mu\text{V/K}$, while semiconductors/insulators typically show several hundred $\mu\text{V/K}$.

$$S = \frac{\Delta V}{\Delta T} \quad (1-1)$$

A related effect, Peltier effect, was discovered in 1834 by Jean Peltier. He described a temperature difference being produced at the junctions of two different conductors when an electrical current flows through the conductors. This finding was not understood until four years later, when Emil Lenz found that the direction of current flow determines the heat absorption or generation.⁴ The corresponding parameter, Peltier coefficient (Π) was defined as the ratio of heat flow rate (Q) to the current (I) as equation (1-2). The Seebeck coefficient

is related to Peltier coefficient by Kelvin relation [equation (1-3)], which was discovered by William Thomson (later Lord Kelvin) in 1851.⁵ Thomson observed experimentally the heating or cooling of a homogeneous current-carrying conductor in the presence of a temperature gradient. The direction of heat flow depends on the direction of the current flow.

$$\Pi = \frac{Q}{I} \quad (1-2)$$

$$\Pi = ST \quad (1-3)$$

The Seebeck effect is extensively employed for power generation and the reverse Peltier effect is widely utilized for electrical cooling or heating objects. Since the alternation of heating or cooling is simply tuned by the sign of the applied voltage, it is convenient to control the temperature by thermoelectric devices. The Seebeck effect and Peltier effect are illustrated in Fig. 1.1.⁶

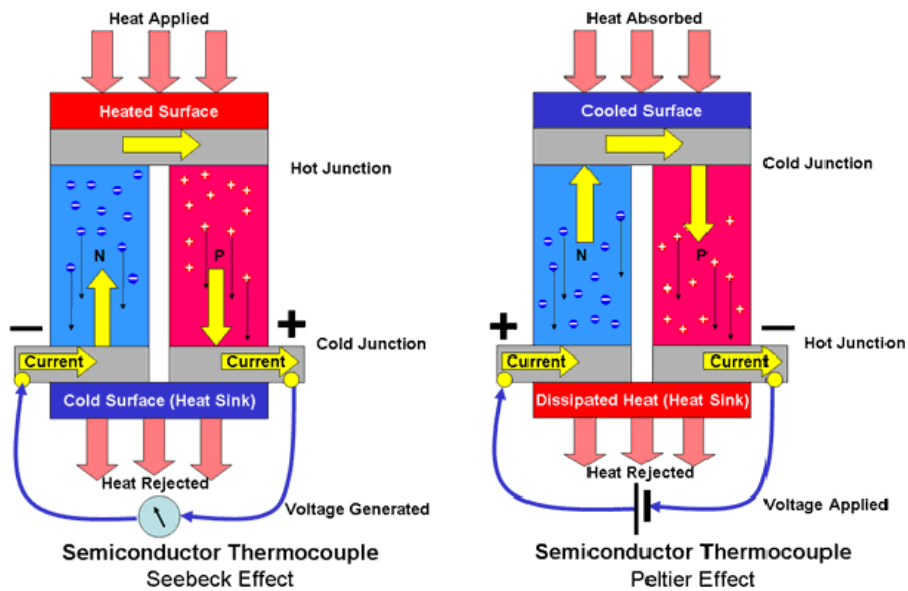


Fig. 1.1 Seebeck effect for power generation (left) and Peltier effect for cooling (right).⁶

1.2 Thermoelectric modules and application

Thermoelectric devices comprise many thermoelectric couples as shown in Fig. 1.2.⁷ Those thermoelectric couples consisting of n -type (free electrons) and p -type (free holes) materials are mounted electrically in series and thermally in parallel. Metalized ceramic substrates provide the platform for a pellet, while the pellets are connected by small conductive tabs. When a temperature gradient is applied across both sides of the device, a voltage gradient will be created and electricity will be exported by the Seebeck effect. If the external circuit is a d.c. power supply, the electric current will drive a heat flow, resulting in cooling down one of the surfaces to create a temperature gradient by Peltier effect.

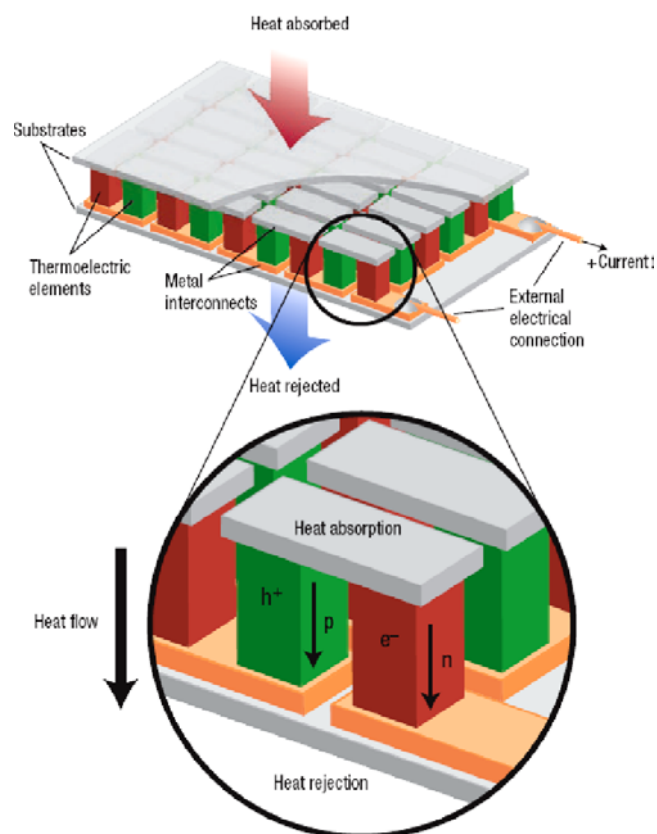


Fig. 1.2 Direction of charge flow in thermoelectric module.⁷

As mentioned at the beginning of this chapter, some automobile companies have been working on the recovery of waste heat energy by surrounding exhaust pipes of vehicles with thermoelectric devices (Fig. 1.3).⁸ BMW expects that 5% fuel efficiency can be achieved if the vehicle's lighting, climate control and some secondary electrical system are powered by electricity generated by the TEG device.



Fig. 1.3 Waste heat harvesting from exhaust system of a vehicle through TEG device.⁸

Recently, another novel application of thermoelectric generators is about conversion of ambient thermal energy into electricity for low-power uses. Many small individual thermocouples with a size of 1cm of height, 1.5cm width and a few micrometers thickness are mounted in a linked “chain” onto a thin, flexible plastic substrate, which is further assembled into a cylinder. These miniature ambient TEGs can make use of small temperature difference (>2 °C) occurring in a natural environment, such as interfaces between ground to air, water to air and skin to air. The output power depends on the temperature range and the numbers of thermocouples embedded in. This lifetime device can provide power to wireless sensors used for energy management in building and many other areas including automotive performance monitoring, biomedicine and agriculture management etc. An illustration of this ambient energy harvester is shown in Fig. 1.4.⁹

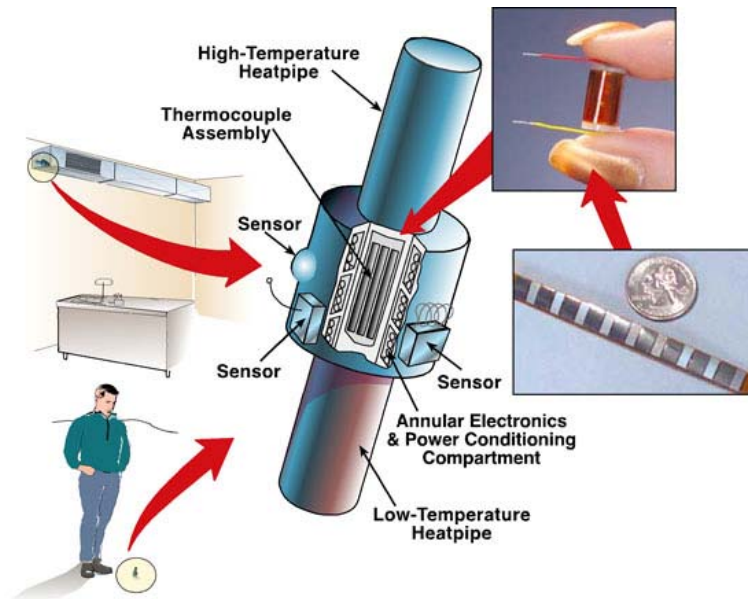


Fig. 1.4 Illustration of thermoelectric ambient energy harvester.⁹

The most notable and ground-breaking application for TEG devices is their use as a power supply for spacecraft. Due to their durability and reliability, they have been widely employed in Pioneer, Voyager, Galileo and Cassini, etc.¹⁰ These devices (as shown in Fig. 1.5), called radioactive thermoelectric generators (RTG), produce electricity by the released heat of the decay of a radioactive material (^{238}Pu , ^{90}Sr). RTGs are usually the most desirable power supplies for unmaintained situations, where a few hundred watts are needed for long durations.

Thermoelectric cooling (TEC) is an environmental-friendly method for small-scale cooling utilization. A Peltier device is mainly used for thermoelectric cooling, which acts as a solid-state heat pump to transfer heat from one side to another with consumption of electricity. They are used for making portable coolers and fridges and provide precise thermal management for optoelectronics and medical instruments. TEC can cool down a

CPU when it is placed between the CPU and heat sink. Thermoelectric devices possess many exclusive advantages, such as scalability, reliability, maintenance-free and harmlessness to environment. However, their existing low efficiency (around 10% Carnot efficiency) is a significant restriction for wide application.

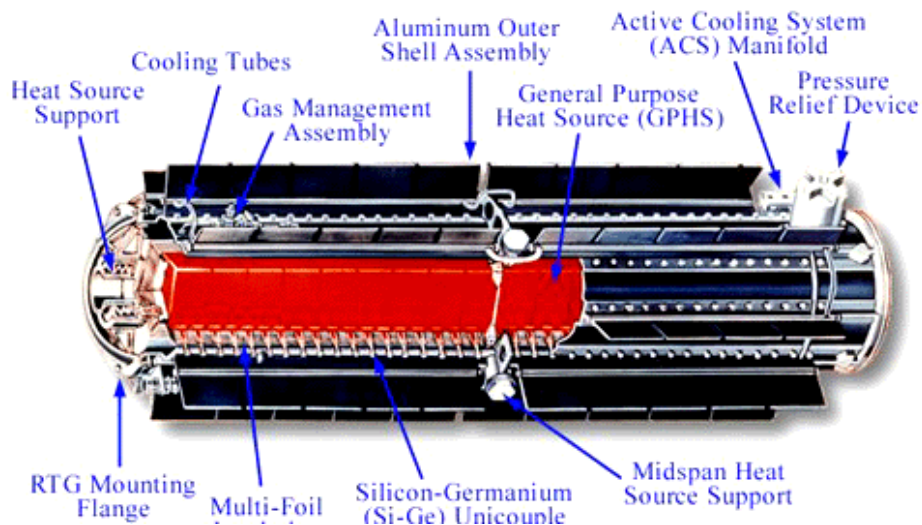


Fig. 1.5 A scheme of radioactive thermoelectric generator (RTG).¹⁰

1.3 Parameters involved in TE research

The main challenge of optimizing thermoelectric property is to balance a variety of conflicting parameters. In order to maximize figure of merit (ZT), a large Seebeck coefficient, high electrical conductivity and low thermal conductivity are required.

1.3.1 Figure-of-merit (ZT) and thermoelectric efficiency

The dimensionless figure-of-merit (ZT) determines the potential of a material used for thermoelectric application, which is defined in equation (1-4). S is the Seebeck coefficient, σ the electrical conductivity, T the average absolute temperature of hot side and cold side, κ the

total thermal conductivity, including lattice (κ_l) and electronic (κ_e) contributions, respectively.

$$ZT = \frac{S^2 \sigma T}{\kappa} \quad (1-4)$$

Based on the definition of ZT , one can clearly conclude that high Seebeck coefficient, high electrical conductivity and low thermal conductivity are beneficial for high ZT . However, because of the strong correlation between these parameters, high ZT can only be achieved with a compromise. Fig. 1.6¹¹ depicts that the peak ZT value is obtained for semiconductor due to its maximum product of $S^2 \sigma$. Neither a metal nor an insulator is a good candidate for thermoelectric material.

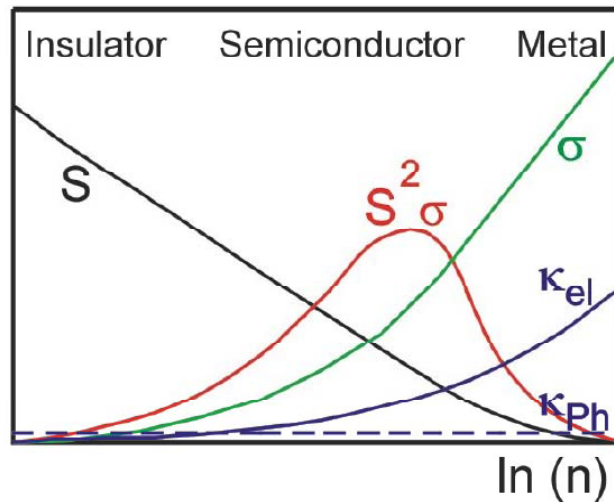


Fig. 1.6 Comparison of thermoelectric parameters between insulator, semiconductor and metal.¹¹

For a thermoelectric power generator, the efficiency (η) is described as the ratio of electrical power output (W) to thermal power supplied (Q_H), as shown in equation (1-5).³ For all heat engines, the upper limit of power generation efficiency is the Carnot efficiency, $[(T_H-$

T_C/T_H], where T is the average temperature of hot side (T_H) and cold side (T_C). η is proportional to $(1+ZT)^{1/2}$ and it would approach the Carnot efficiency if ZT could reach infinity. Therefore, applying a large temperature gradient and improving ZT are both effective means to increase the power generation efficiency.

$$\eta = \frac{W}{Q_H} = \frac{T_H - T_C}{T_H} \cdot \frac{\sqrt{1+ZT} - 1}{\sqrt{1+ZT} + T_C/T_H} \quad (1-5)$$

The efficiency of a thermoelectric refrigerator, is the ratio of cooling rate (Q_C) over the power supplied (W), expressed by the coefficient of performance (COP) in equation (1-6). The COP at Carnot efficiency is $[T_C/(T_H-T_C)]$, where T_H and T_C are the temperatures of ambient environment and the coldest part of the refrigerator, respectively. The real efficiency is often given as a percentage of Carnot efficiency. Present thermoelectric cooling devices can only reach about 10% of Carnot efficiency.¹²

$$\phi = \frac{Q_C}{W} = \left(\frac{T_C}{T_H - T_C} \cdot \frac{\sqrt{1+ZT} - 1}{\sqrt{1+ZT} + 1} \right) - \frac{1}{2} \quad (1-6)$$

1.3.2 Seebeck Coefficient

The Seebeck coefficient of a material, also called thermopower, is a measure of the magnitude of an induced voltage in response to a temperature difference across the material. Referring to equation (1-1), the Seebeck coefficient has a unit of volts per Kelvin (V/K), although the unit of microvolts per Kelvin ($\mu\text{V/K}$) is more often used.

Semiconductors have two types of charge carriers, namely electrons (inducing a negative Seebeck coefficient) and holes (causing a positive Seebeck coefficient). A single

type of carrier may ensure a large Seebeck coefficient since the mixed n -type and p -type conduction can lead to cancellation. Doping the semiconductors with either donor or acceptor elements to create extrinsic semiconductors is a quite common strategy to optimize the thermoelectric properties. In order to maintain the high Seebeck coefficient, it is important to minimize the contribution of the minority carriers. A typical Seebeck coefficient for good thermoelectric performance is within 150-250 $\mu\text{V/K}$ range or greater for a semiconductor.¹³

For metals or degenerate semiconductors, the Seebeck coefficient is given in equation (1-7), where n is the carrier concentration, m^* is the effective mass of the carrier and k_B is Boltzmann constant.⁷ Insulators and semiconductors have low carrier concentration resulting in a large Seebeck coefficient but low electrical conductivity.

$$S = \frac{8\pi^2 k_B^2}{3eh^2} m^* T \left(\frac{\pi}{3n} \right)^{2/3} \quad (1-7)$$

1.3.3 Electrical conductivity

Electrical conductivity (σ) is a measure of a material's ability to conduct an electric current. It is defined as the ratio of the current density (J) to the electric field strength (E) as shown in equation (1-8). Since $J = \frac{I}{A}$ and $E = -\frac{dV}{dx}$, the equation (1-8) can be rewritten as the form of equation (1-9), where l is length and A is area of cross-section of a conductor. The inverse of σ is electrical resistivity (ρ).¹⁴

$$\sigma = \frac{J}{E} \quad (1-8)$$

$$\sigma = \frac{1}{\rho} = \frac{l}{RA} \quad (1-9)$$

The electrical conductivity is also related to the carrier concentration (n) and the carrier mobility (μ) [equation (1-10)]. The carrier mobility is defined as equation (1-11), where τ is the mean scattering time between the collisions of the carriers.¹⁴ The equation (1-10) is of great importance in the theory of conductivity and explains the difference between the electrical properties of metals and semiconductors. In metals, where all the valence electrons are free at all temperature, n is a constant and the temperature variation of σ is the temperature variation of μ . However, in semiconductors the carriers must be thermally promoted across a band gap for conduction to occur. Therefore, n always varies with the temperature and in fact, the temperature plays an even more important role in the semiconductors.

$$\sigma = ne\mu \quad (1-10)$$

$$\mu = \frac{e\tau}{m^*} \quad (1-11)$$

Since the carrier concentration has a conflicting effect on Seebeck coefficient and electrical conductivity, the peak ZT typically occurs at carrier concentrations between 10^{19} to 10^{21} carriers/cm³, which makes the heavily doped semiconductors and narrow band gap semiconductors the most promising candidates for thermoelectric applications.

Referring to equation (1-7) and (1-11), the effective mass of charge carriers is another conflicting factor, as large effective mass produces a high Seebeck coefficient but low

electrical conductivity. Heavier carriers always move with slower velocities, thereby causing small mobility and lower electrical conductivity.

1.3.4 Thermal conductivity

The thermal conductivity (κ) is related to the heat transfer through materials by electron/hole transporting (κ_e) and phonons travelling (κ_l), as shown in equation (1-12). The electronic thermal conductivity (κ_e) is expressed through Wiedemann-Franz law as equation (1-13), where L is the Lorenz number, $2.44 \times 10^{-8} \text{ W}\Omega\text{K}^{-2}$ for free electrons.⁷ The lattice (phonon) contribution (κ_l) of thermal conductivity is described in equation (1-14) with v_{ph} the velocity of phonon, C the heat capacity and L_{ph} the mean free path of the phonons.¹⁵

$$\kappa = \kappa_e + \kappa_l \quad (1-12)$$

$$\kappa_e = L\sigma T \quad (1-13)$$

$$\kappa_l = \frac{1}{3} v_{ph} C L_{ph} \quad (1-14)$$

Good thermoelectric materials evidently require a low thermal conductivity to prevent a significant portion of heat from flowing down the temperature gradient. Most research works are focused on reducing thermal conductivity without disrupting electrical conductivity. However, it is challenging because a significant portion of thermal conductivity originates from the electrons or holes contribution, especially in the heavily-doped semiconductors. In order to solve this problem, the concept of “phonon-glass electron-crystal” (PGEC) was provided, i.e. that a material would have the electrical property of a crystalline and the thermal property of an amorphous material.¹⁶ In another words, PGEC

materials possess short mean free paths of the phonons and long mean free paths of electrons, thus good thermoelectric properties will be achieved by increasing phonon scattering without significantly disturbing the electron mobility.

A lot of research has been focused on reducing the lattice part to minimum total thermal conductivity, which can be accomplished when all the phonons have a mean free path equal to the inter-atomic spacing of the constituent atoms. This strategy has been tackled by scattering phonons in different frequency ranges by using a variety of methods, such as intercalating heavy atoms in the empty voids of the crystal structure (rattling effect),¹⁷ creating significant phonon diffusion by mass fluctuations and impurities or point defects,¹⁸ reducing the mean free path of phonons by increasing grain boundaries in nano-scale materials¹⁹ and interface scattering in thin films or multilayer systems.²⁰

In general, the good thermoelectric materials should possess some specific characteristics. Typically, good thermoelectric materials are narrow band gap semiconductors ($E_g = 0.1 \sim 1.0$ eV at 300 K), with high mobility of the carriers ($\mu \approx 2000$ cm²V⁻¹s⁻¹), while the thermal conductivity is minimized. To maintain the high mobility, the difference of electronegativity between the elements of the material must be as small as possible, such as between the elements Bi, Sb, Se, Te, Ge, Sn, etc. The minimum thermal conductivity (κ_{min}) refers to a value, $\kappa_{min} \approx 0.25\text{-}0.5$ Wm⁻¹K⁻¹, when the phonon mean free path is close to the phonon wavelength.²¹

1.4 Developments in thermoelectric materials

Some materials systems attract broad attention because of their outstanding thermoelectric properties. These materials exhibit good electrical conductivity, relatively

high Seebeck coefficient and moderate low thermal conductivity, which endow them with a high figure-of-merit. Many investigations have been concentrated on one or more of these materials to further optimize their thermoelectric properties. Some of these materials, with a variety of development strategies, are summarized herein, including the materials that are closely related to my research work.

1.4.1 Chalcogenides

1.4.1.1 CsBi₄Te₆

Chalcogenide compounds are remarkable semiconductors for thermoelectric application, such as Bi₂Te₃ and its solid solutions Bi_{2-x}Sb_xTe₃ and Bi₂Te_{3-x}Se_x, have a ZT values around 1 at 350 K.^{22, 23} Some other binary tellurides (Sb₂Te₃, PbTe and GeTe) and the doped variants have been an active research area continuously.²⁴⁻²⁷ Another prominent tellurium compound that needs to be mentioned here is CsBi₄Te₆,²⁸ a derivative of Bi₂Te₃. This compound has a lamellar structure with slabs of (Bi₄Te₆)⁻¹ alternating with layers of Cs⁺ ions (Fig.1.7), featured with exceptional transport properties in one direction. The optimized CsBi₄Te₆ with 0.05% SbI₃ doping has a maximum ZT (225 K) = 0.8 along the growth axis, which is a competitive value for low temperature application. Various doping can move ZT_{\max} to the lower temperature of 180 K.²⁹

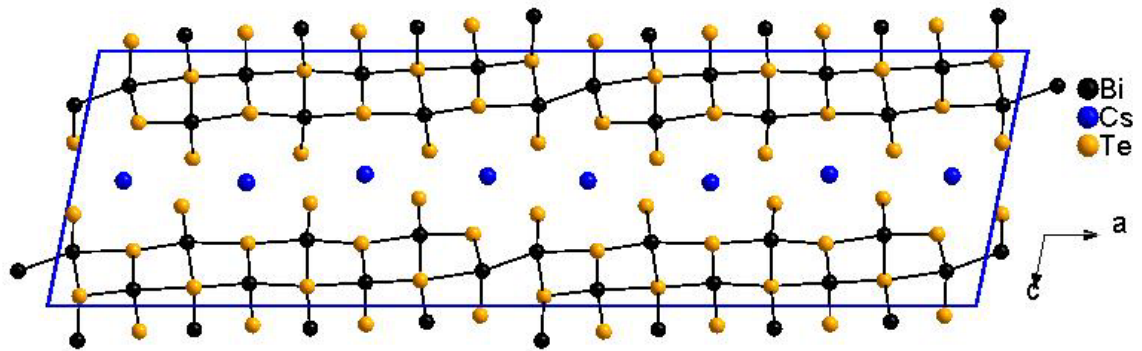


Fig. 1.7 Crystal structure of CsBi_4Te_6 .

1.4.1.2 $\text{AgPb}_m\text{SbTe}_{m+2}$

In 2004, Hsu *et al.* published the thermoelectric properties of $\text{AgPb}_m\text{SbTe}_{m+2}$ (LAST-*m*; LAST stands for lead, antimony, silver and tellurium), $\text{AgPb}_{18}\text{SbTe}_{20}$ reaches ZT of ~ 2.2 at 800 K and $\text{AgPb}_{10}\text{SbTe}_{12}$ obtains ZT_{max} of 1.2 at 700 K.³⁰ A number of isostructural compositions can be generated by varying m . This family of compounds possesses the NaCl structure type (space group $Fm\bar{3}m$), with the Ag, Pb, and Sb metals disordered on the Na sites, while the Te atoms occupy the Cl sites. However, a subsequent investigation of structure revealed that $\text{AgPb}_m\text{SbTe}_{m+2}$ has inhomogeneous phases at the nanoscale with two coexisting phases, including Ag and Sb rich minor phases embedded in Ag and Sb poor major phases.³¹ A large number of nanocrystalline-matrix interfaces could impede the phonon transmission in the bulk materials, thereby inducing the enhancement of ZT . It has been proved by the low lattice thermal conductivity of this family compounds, ranging from $2.1 \text{ Wm}^{-1}\text{K}^{-1}$ around 300 K to $0.75 \text{ Wm}^{-1}\text{K}^{-1}$ at 750 K (actual values depend on m).³²

1.4.1.3 Tl-containing telluride

In the last decade, it was shown that some thallium chalcogenides present very low thermal conductivity. Tl_9BiTe_6 ,³³ a substitution variant of Tl_5Te_3 , exhibits the maximum $ZT \sim 1.2$ around 500 K because of its extremely low thermal conductivity ($0.39 \text{ W m}^{-1}\text{K}^{-1}$ at 300 K), which is due to the strong phonon scattering caused by valence disorder (Tl^+ and Bi^{3+} occupy statistically mixed the $4c$ sites). Tl_2SnTe_5 and Tl_2GeTe_5 ³⁴ are isostructural compounds with the columns of Tl ions along the c axis and the chains of $(\text{SnTe}_5)^{2-}$ or $(\text{GeTe}_5)^{2-}$ running parallel to each other between Tl ions. The chains can be described as $(\text{Sn/Ge})\text{Te}_4$ tetrahedra linked by Te atoms that are in square planar coordination. Both demonstrate very low thermal conductivity. Tl_2SnTe_5 reaches ZT around 0.85 at 400 K. The crystal structure of Tl_9BiTe_6 and Tl_2SnTe_5 are shown in Fig. 1.8.

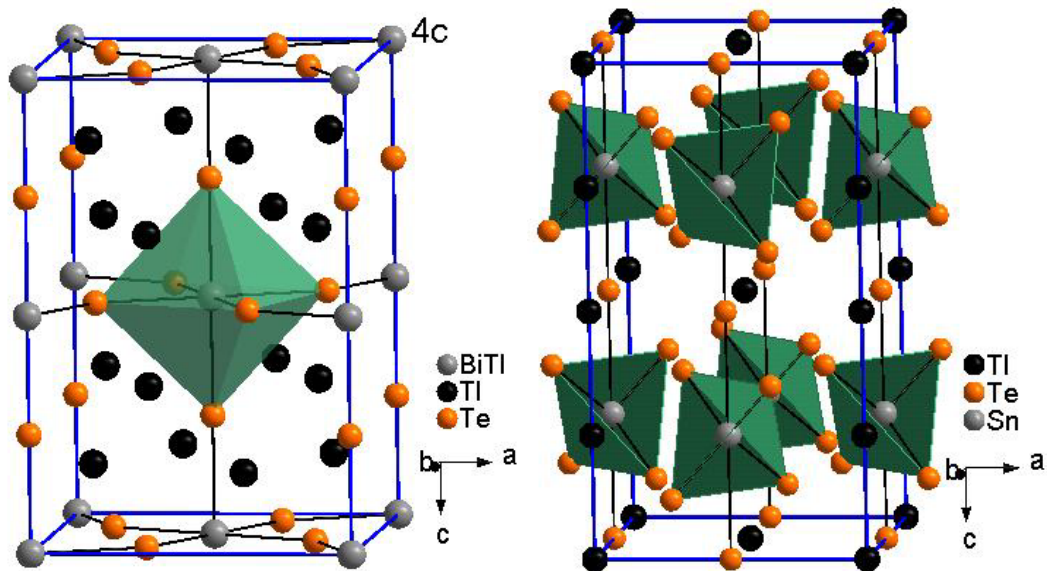


Fig. 1.8 Crystal structure of Tl_9BiTe_6 (left, Bi/Tl mixed occupy $4c$ site, grey spheres) and Tl_2SnTe_5 (right).

Another interesting Tl-containing compound is Ag_9TlTe_5 ,³⁵ a substitution variant of Ag_2Te . It has very low thermal conductivity of $0.23 \text{ Wm}^{-1}\text{K}^{-1}$ at room temperature, leading to a $ZT = 1.23$ at 700 K. However, Tl-containing compounds cause a lot of environmental concerns due to thallium toxicity; therefore they are unlikely to be accepted for practical applications.

1.4.2 Antimonides

1.4.2.1 Filled skutterudites

Skutterudites received intensive attention since the 1990s because of their significant reduction in thermal conductivity by “void fillers”. The skutterudite type (CoAs_3 type) structure is a cubic structure comprising eight corner shared MX_6 ($\text{M} = \text{Co}, \text{Rh}, \text{Ir}; \text{X} = \text{P}, \text{As}, \text{Sb}$) octahedra, as depicted in Fig. 1.9. The linked octahedra create a void at the center of $(\text{MX}_6)_8$ unit, which may be occupied by relatively large metal atoms, resulting in the formation of filled skutterudites.¹⁷ Many different elements, such as lanthanide, alkali, alkaline-earth elements and group 14 elements have been intercalated into the voids as “rattlers”.³⁶⁻³⁸ These guest atoms act as phonon scattering centers to reduce the lattice thermal conductivity, thus leading to an enhancement of thermoelectric properties. For instance, 5% La or Ce filling in the voids can reduce ~50% thermal conductivity of CoSb_3 .^{39,40} Compared with the fully filled skutterudites, partially filled ones can obtain the higher power factors by optimizing the charge carrier concentration, thereby improving ZT value.^{41,42} $\text{LaFe}_3\text{CoSb}_{12}$ and $\text{CeFe}_3\text{CoSb}_{12}$ demonstrated the high ZT values at the elevated temperature, e.g. $\text{LaFe}_3\text{CoSb}_{12}$ reached $ZT \approx 1$ at 800 K.¹⁷

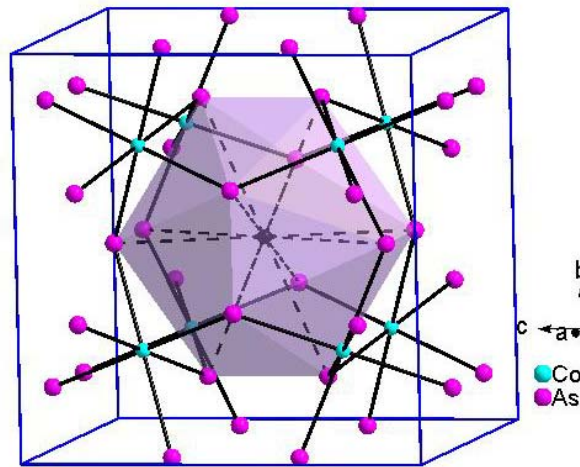


Fig. 1.9 Crystal structure of skutterudite, where a guest atom occupies the center of void.

1.4.2.2 $\text{Yb}_{14}\text{MnSb}_{11}$

In 2006, Brown *et al.*⁴³ reported the thermoelectric properties of a complex Zintl compound, $\text{Yb}_{14}\text{MnSb}_{11}$, attaining $ZT = 1.1$ at 1275 K. This *p*-type high-temperature thermoelectric material has been further investigated by NASA for potential application in spaceships.⁷ $\text{Yb}_{14}\text{MnSb}_{11}$ crystallized in $\text{Ca}_{14}\text{AlSb}_{11}$ structure type (space group $I4_1/acd$), containing MnSb_4 tetrahedra and linear Sb_3 units, as shown in Fig. 1.10. $\text{Yb}_{14}\text{MnSb}_{11}$ exhibits a very low thermal conductivity, $0.9 \text{ Wm}^{-1}\text{K}^{-1}$ at 300 K, likely caused by the complexity of the structure (limiting the phonon mean-free path) and heavy atomic mass (reducing the lattice thermal conductivity). Partial substitution of Yb with La⁴⁴ and Mn with Zn⁴⁵ and Al^{46, 47} can improve the thermoelectric properties in the order of 10%.

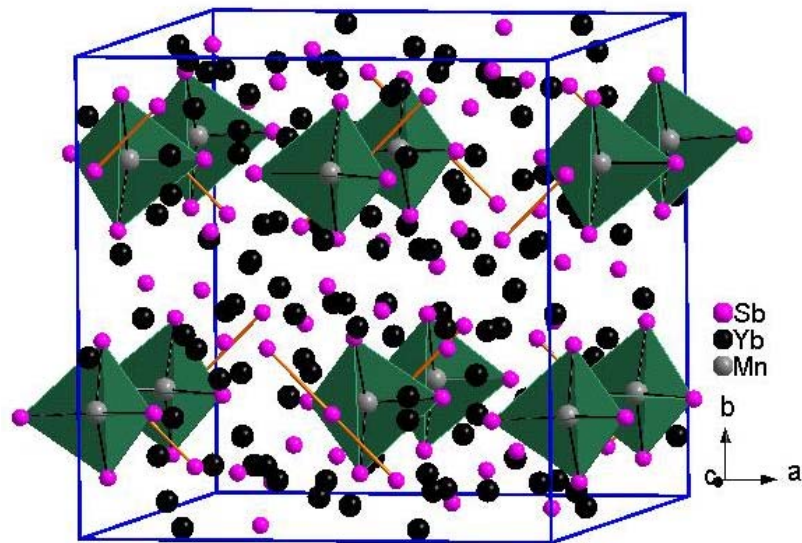


Fig. 1.10 Crystal structure of $\text{Yb}_{14}\text{MnSb}_{11}$.

1.4.3 Nanostructured bulk thermoelectric materials

Although a high ZT has been achieved in a broad range of nanostructured materials, such as superlattices,⁴⁸ quantum dots⁴⁹ and nanowires,^{50, 51} these materials cannot be used for large-scale commercial applications, since they are mostly fabricated by atomic layer deposition, an expensive and slow fabrication process. Therefore, how to make a nanostructured material by a bulk process rather than a nanofabrication method became of great interest in the past decades.^{7, 12, 52, 53}

The term “nanocomposite” was introduced to describe the nanostructured bulk materials structures, including the nanoparticles embedded in a host or heterostructure geometry with the nanoparticles adjacent to each other. Hicks and Dresselhaus introduced the idea of improving ZT using lower dimensional structures in 1993.⁵⁴ The theory behind is the

nanoparticles have smaller grain sizes than the mean free paths of the phonons, but greater than the mean free paths of the electrons and holes, thus the phonons can be more strongly scattered by the interfaces than electrons/holes, leading to a significant reduction of lattice thermal conductivity while maintaining the reasonable electrical conductivity, thereby leading to an enhancement of ZT .¹⁹

The Kanatzidis group successfully developed a method to create bulk nanocomposites by forming the nanoscale domains via a thermal process, which is favorable for phonon scattering (as discussed in section 1.4.1.2).^{26, 30, 55, 56} These techniques have been applied to several different systems to achieve high ZT values, such as n -type $\text{AgPbTe}_2/\text{PbTe}$,³⁰ n -type $\text{Pb}_{1-x}\text{Sn}_x\text{Te}/\text{PbS}$,⁵⁶ and p -type $\text{Na}_{1-x}\text{Pb}_m\text{Sb}_y\text{Te}_{m+2}$.²⁶ All of these materials exhibited high ZT values with remarkably low thermal conductivity.

Another method uses a ball milling followed by hot pressing to produce nanocomposites.⁵⁷⁻⁶⁰ Raw elements are mixed and ground into a nanoscale dust using a ball milling machine, then the mixture is hot pressed at appropriate temperature and pressure to prepare the densified solid materials. The nanoparticles get fused together but the interfaces between them remain intact. This technique was successfully employed to prepare the nanostructured n -type and p -type Si-Ge solid solutions and different types of $\text{Bi}_x\text{Sb}_{2-x}\text{Te}_3$. Among these materials, n -type $\text{Si}_{80}\text{Ge}_{20}$ achieved ZT of 1.3 at 900 °C, which is about 40% higher than the commercial bulk alloys;⁵⁹ p -type $\text{Si}_{80}\text{Ge}_{20}$ reached ZT of 0.95 at 800 °C, which is about 50% higher than the reported value of bulk Si-Ge solid solution.⁶⁰ Nanostructured p -type $\text{Bi}_x\text{Sb}_{2-x}\text{Te}_3$ exhibited a peak ZT of 1.4 at 100 °C, which is 40% higher than the ZT of bulk $\text{Bi}_x\text{Sb}_{2-x}\text{Te}_3$.⁵⁷ The comparison of figure-of-merit between the current

state-of-art bulk thermoelectric materials and nanostructured materials is shown in Fig. 1.12.¹⁹

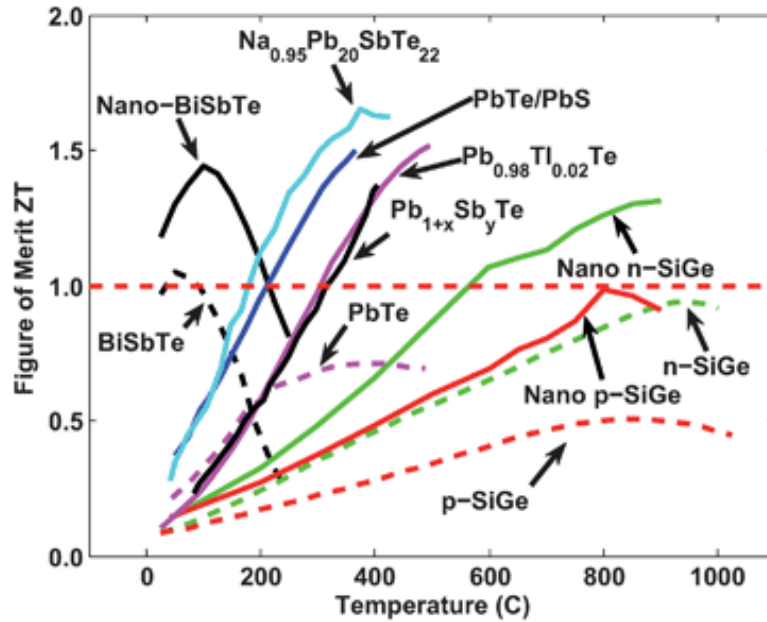


Fig. 1.11 Comparison of figure-of-merit between current state-of-art bulk thermoelectric materials and nanostructured thermoelectric materials.¹⁹

In general, there are two primary approaches to develop advanced thermoelectric materials. One strategy is developing the nanostructured materials with the minimized thermal conductivity, leading to an enhancement of thermoelectric properties.¹⁹ The other one is to create new materials with desired thermoelectric properties by modifying the crystal structure and optimizing the charge carrier concentration.⁷ My Ph. D work is mainly focused on improving the thermoelectric properties using the second strategy.

1.4.4 Research background and objectives

1.4.4.1 Modifications of representatives of Ir_3Ge_7 structure type materials

The Ir_3Ge_7 structure, with space group of $Im\bar{3}m$, contains three independent atomic positions: $12e$ (Ir), $12d$ (Ge1, red spheres) and $16f$ (Ge2, pink spheres), as shown in Fig. 1.12. The Ir atoms are located at the center of square antiprism formed by Ge1 and Ge2 atoms, and two such antiprisms share a square face comprised of Ge1 atoms. Eight Ge2 atoms form an empty cube, which acts as a junction unit.⁶¹ The known Ir_3Ge_7 structure type compounds have a narrow range of valence-electron count (VEC), between 51 to 56 electrons per formula unit.

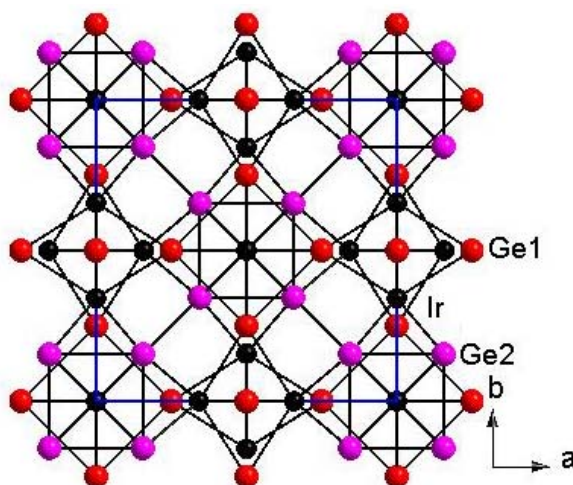


Fig. 1.12 Crystal structure of Ir_3Ge_7 .

Mo_3Sb_7 and Re_3As_7 both adopt the Ir_3Ge_7 structure type. Mo_3Sb_7 is metallic with its 53 valence electrons. Electronic structure calculation (LMTO) predicts the Fermi level can be lifted into the band gap (around 0.5 eV) if the number of valence electrons can be increased

up to 55, e.g. by substituting two Sb atoms with two Te atoms to form $\text{Mo}_3\text{Sb}_5\text{Te}_2$.⁶² The physical property measurement results confirmed the semiconductivity of $\text{Mo}_3\text{Sb}_{7-x}\text{Te}_x$. Meanwhile, intercalation of different elements (Mg, Cu, Ni) into the center of the Sb2 cube decreases the band gap.⁶³ Therefore, one of my research motivations is to explore how a variety of transition metal atoms (Mn, Fe, Co and Ni) will affect the thermoelectric properties and the effect of varying the Sb/Te ratio.

The isostructural Re_3As_7 demonstrates metallic properties with its 56 valence electrons. The electronic structure calculation indicates that the Fermi level can be lowered into the band gap if the number of valence electrons is reduced to 55 by As/Ge exchange, a ZT of 0.3 at 700 K is obtained for $\text{Re}_3\text{Ge}_{0.6}\text{As}_{6.4}$.⁶⁴ In my Ph. D work, other elements of group 14, e.g. Si, Sn, Pb, were chosen to partially replace As atoms for further investigation. In addition, the substitution on the cation site, such as Mo/Re exchange was also tackled.

1.4.4.2 Narrow gap semiconductors with square net distortions

An early comprehensive investigation of electronic structure of compounds containing square nets was published in 1987.⁶⁵ When a crystal structure changes from the ZrSiS type (with undistorted Si square nets) to the GdPS type (with distorted P layers), the symmetry is reduced from orthorhombic to monoclinic, resulting in an opened band gap. Similar cases occur in the compounds of NbPS type. For example, TiAsTe comprises As distorted square nets with the alternating As–As distances of 2.55 Å and 2.70 Å, which makes TiAsTe showing the physical properties between metal and semiconductor.⁶⁶

My research objective is to explore ternary and higher chalcogenide compounds which contain distorted As square nets, thereby leading to semiconducting properties. These

compounds are supposed to have large Seebeck coefficient and exhibit potential applications in thermoelectrics.

2 Experimental techniques and physical property measurements

There are a number of synthetic methods available to prepare different forms of solid materials. In this chapter, only the techniques involved in my research will be briefly discussed.

2.1 Synthetic methods

2.1.1 Solid-state reaction

The synthesis of solid materials, particularly the form of polycrystalline powder, is often performed by a solid state reaction. However, solid state reactions are always very slow and difficult to complete unless high temperatures are applied, enabling the internal atoms to diffuse easily to the contact surfaces of the grains. This procedure can be divided into two stages: nucleation of the reaction product and subsequent growth.⁶⁷ Nucleation is generally difficult because a structural rearrangement of the lattice of reactants is required to form nuclei of the product. This reorganization of atoms requires energy obviously, therefore it will only occur significantly at elevated temperatures. Once the nuclei of the product have formed, the growth of the product layer will depend on the diffusion of reactants ions, through the product layer to the reaction front.

The rate of thickness change of the product layer, $d(\Delta x)/dt$, is proportional to the ion flux (the number of ions passing through the unit area per unit time), and the growth rate is written as equation (2-1), where k is a rate constant.

$$\frac{d(\Delta x)}{dt} = \frac{k}{\Delta x} \quad (2-1)$$

This rate law can be integrated to give a parabolic equation: $(\Delta x)^2 = 2kt$, which has been confirmed experimentally, for example in the case of the formation of the spinel NiAl_2O_4 from NiO and Al_2O_3 .⁶⁸

The rate of solid-state reactions also depends on the surface area of contact between the solid reactants. Smaller particles can react faster and produce a more homogeneous sample. In my sample preparation, all the starting materials were thoroughly ground and mixed intimately to optimize homogeneity of the final products.

2.1.2 Flux method

In solid state chemistry, high temperature is often required to overcome the activation energy barrier and increase the reactant diffusion rate to form the new phase. Therefore, high temperature is the synthetic limitation. On the other hand, the fast cooling of reactants from high temperature is not favorable for crystal growing. Single crystals can sometimes form through the extended annealing. However, it is still difficult to obtain crystals with sufficient size for physicochemical characterizations in many cases.

Flux method is one of the most widely used approaches for growing single crystals in a molten salt medium.⁶⁹⁻⁷¹ Molten solids can be used as solvent to enhance the diffusion of reactants. Although many salts have high-melting temperatures, combinations of them usually offer the lower melting points. In some cases, these salt mixtures, called “reactive flux”, act not only as solvents, but also as reactants, being incorporated into the final

product.⁷² Since the diffusivity of the components is much higher in liquids than in solids, the reaction temperature and the reaction time are significantly reduced by using flux method.

Molten-salt synthesis (MSS) is a simple method for preparing, e.g. complex oxides with the desired composition in a low-melting point flux.⁷³ Molten-salts, such as LiCl, NaCl, KCl and RbCl, are usually used as a solvent or reaction species for chemical reaction.^{74, 75} Many complex oxides, such as LiNiO₂,⁷⁶ LiFePO₄,⁷⁷ LiNi_{0.5}Mn_{1.5}O₄,⁷⁸ Bi₅Ti₃FeO₁₅,⁷⁹ and LiCoO₂⁸⁰ have been successfully prepared by MSS. The morphology and size of particles can be controlled by the process parameters, such as temperature, time and amount of flux.⁷⁴ In my Ph. D. work, I used LiCl/ RbCl mixture as a flux to decrease the reaction temperature and enhance the growth of single crystals.

Another common flux medium is a liquid metal, which is usually used for synthesis of intermetallics and other non-oxide solids, such as carbides, nitrides and pnictides.^{81, 82} In order to apply metallic flux, some critical points must be met: 1) the metal should have low melting point to form a flux at a reasonable low temperature so that normal heating equipment and containers can be used; 2) the metal should have a large difference between its melting and boiling temperatures; 3) it should be possible to separate the metal from the product by physical or chemical methods; 4) the metal should not form any stable phase with any of the reactants.⁷²

Care must be taken to prevent the liquid metal from reacting with container in metal flux experiment. Aluminum is a highly reducing metal and can react with many conventional containers quickly, e.g. quartz ampoule. Less reactive metals, such as Sn, Ga, and In also react with silica if they are in contact for a period of time at high temperature. Thus, an inert

container, Tamman crucible (Al_2O_3), is more suitable for metal flux medium. The reactants and desired metal are usually loaded into an alumina crucible and placed into the silica tube. Then the silica tube will be sealed under vacuum. A graphite crucible is an alternative for Sn and Ga media. However, both alumina and graphite react with liquid alkali metals and therefore are not usable for them. For the high temperature reactions, tubes or crucibles made of high-melting metals (Nb, Ta, Mo, W) are utilized. In the molten-salt synthesis, alumina crucibles are also employed to prevent possible reaction between the molten salt and silica tube after “whitened” tubes were observed. In my work, I used alumina crucibles for both Sn flux and LiCl/RbCl molten-salt flux.

2.1.3 Chemical vapor transport

Chemical vapor transport (CVT) is another method where crystals are grown in a closed tube. Therein, the solid compound reacts with the gaseous medium to form a gaseous product, which undergoes a reverse reaction at a different part of the tube.⁸³ The equilibrium between the reaction and the reverse reaction depends on the temperature gradient, which is also the main driving force for mass transport by diffusion. The scheme of chemical vapor transport procedure is shown in Fig. 2.1.

With $T_2 > T_1$, and an endothermic reaction, the solid materials A will react with B to form gaseous AB at the higher temperature T_2 . Then, the reverse reaction occurs after AB migrates to the low temperature location T_1 , and A is deposited from the gas phase. For the exothermic reactions, the solid phase is transported in the reverse direction, $T_1 \rightarrow T_2$.⁸⁴ A variety of transport agents can be used depending on the different reactions, e.g. NH_4Cl ,

HgCl₂, AlCl₃, S, I₂ and gaseous O₂, CO, CO₂, Cl₂, Br₂ etc. In this thesis, I₂ was chosen as transporting agent to help to grow single crystals.

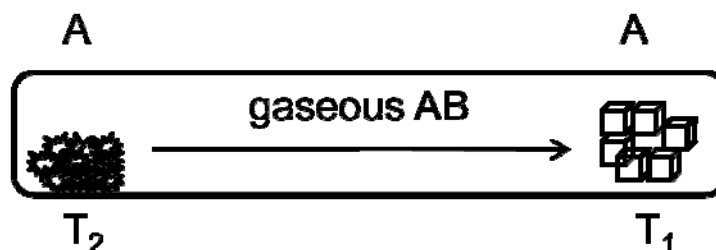


Fig. 2.1 Scheme of chemical vapor transport in a closed tube. Transport is from temperature T_2 to T_1 ($T_2 > T_1$).

2.1.4 Experimental synthesis

All the samples were prepared in an argon filled glove box to avoid contact with oxygen and moisture in the air. The powder or small chunks of starting material, as weighed with the desired stoichiometric ratios and loaded into a quartz tube. In the cases where the starting sample might react with the quartz tube to cause a so-called “tube attack” phenomenon, a Tamman crucible (Al₂O₃) was used to contain the starting materials and this was then inserted into the quartz tube. The quartz tube was evacuated to 10^{-3} mbar, and sealed using an oxyhydrogen torch. The sealed tubes were placed into the resistance furnace and heated under appropriate temperature for a period of several days to several weeks. In some cases, the samples were reheated to improve the homogeneity. The general steps of sample preparation are depicted in Fig. 2.2.



Fig. 2.2 Steps for sample preparation. (a) glove box; (b) vacuum line; (c) H₂/O₂ torch; (d) sealed tubes; (e) resistance furnace.

2.2 Analysis techniques

After the sample is prepared, the first step is to determine the crystal structure of an unknown compound by single crystal X-ray diffraction. If a compound has a known structure and some elements of this compound are partially substituted by other elements, powder X-ray diffraction (PXRD) can be utilized to check the change of diffraction pattern and inspect the purity of the sample. For some compounds wherein few single crystals formed, PXRD may be a useful tool to solve the structure, particularly if an appropriate model with a similar structure is known. Meanwhile, analysis from energy dispersive X-ray (EDX) can be applied

to approximately determine the composition and examine the morphology and homogeneity. If the sample is considered to be a pure compound, the physical property measurements will be carried out. These include the measurements of Seebeck coefficient, electrical conductivity and thermal conductivity. The thermal stability can be tested by differential scanning calorimetry (DSC). All the techniques mentioned above have been employed during my Ph.D. study. An introduction of the working principles of these instruments is briefly outlined below.

2.2.1 Fundamentals of X-ray diffraction

X-rays are photons, which are created when accelerated electrons strike a target (anode). X-rays were first described by German physicist Röntgen in 1896. A few years later, Sommerfeld measured the wavelength of X-rays to be about 0.4 Å. In 1912, von Laue, starting from the work of Ewald, a student of Sommerfeld, suggested the use of crystals as natural lattices for diffraction. This experiment was successfully conducted by the students of Röntgen, Friedrich and Knipping. In 1913, Bragg and von Laue firstly deduced the crystal structures of NaCl, KCl, KBr and KI using X-ray diffraction patterns. Since then, X-ray diffraction has become a powerful tool for crystal structure determination.⁸⁵ X-rays wavelengths range from 0.1 Å to 100 Å, corresponding to the energies of 100 keV to 0.1 keV. X-ray crystallography usually uses the wavelengths between 0.5 Å and 2.5 Å.

von Laue systematized the experimental results quantitatively by the following three conditions which must be met simultaneously for diffraction to occur:

$$a (\cos\alpha - \cos\alpha_0) = h \lambda$$

$$b (\cos\beta - \cos\beta_0) = k \lambda$$

$$c (\cos\gamma - \cos\gamma_0) = l \lambda$$

Therein, a , b and c are dimensions of unit cell, α_0 , β_0 and γ_0 the angles between the incident beam and the rows of atoms in the three directions, α , β and γ the angles between the diffracted beam and the rows of atoms in the three directions, h , k and l are Miller indices and λ is the wavelength of the X-rays. These relations are defined as Laue equations.⁸⁶ The path difference in each dimension, e.g. $a (\cos\alpha - \cos\alpha_0)$, must be an integral number of wavelengths if the scattered waves are in phase.

After Laue's work was published, W. L. Bragg proved that Laue's conditions were equivalent to the reflection from a lattice plane and then they can be expressed by a simpler equation (2-2), known as "Bragg's law".⁸⁷

$$n\lambda = 2d \sin\theta \quad (2-2)$$

Where n is an integer, λ the wavelength of the X-rays, d the interplanar spacing and θ the angle of incident beam on the plane. Bragg's law can be easily derived from the drawing in Fig. 2.3. Two X-ray beams, 1 and 2 are reflected from adjacent planes and the reflected beams 1' and 2' are in phase. Beam 22' traveled the extra distance ACB, compared with the distance of beam 11'. This ACB distance must be equal to $n\lambda$ if 1' and 2' are in phase, since $\angle AOC = \angle BOC = \theta$, $AC = BC$ and $2AC = n\lambda$. Considering $AC = d \sin\theta$, $2AC = 2d \sin\theta = n\lambda$, Bragg's law is deduced. According to Bragg's law, diffraction can be observed at any combination of θ and d that fits the equation.

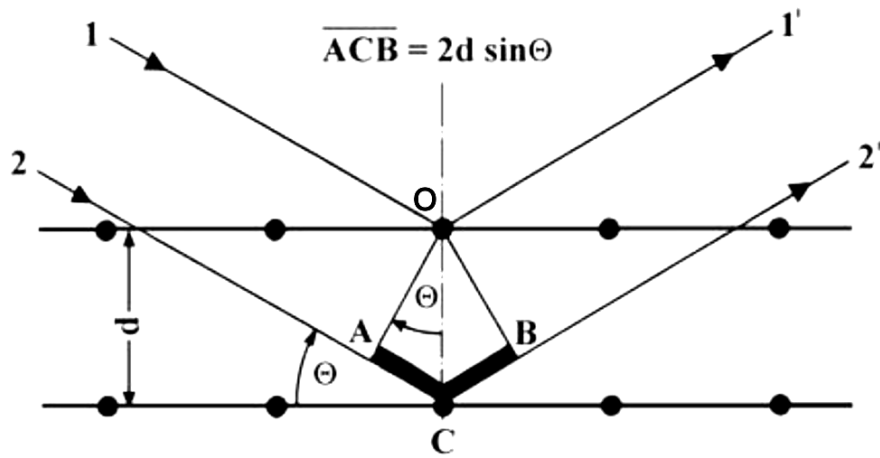


Fig. 2.3 The derivation of Bragg's law.

The interaction between X-rays and crystals involves the electrons within crystal. The more electrons an atom has, the stronger scattering occurs. The atomic scattering factor f_j is the efficiency of an atom j in scattering X-rays, which depends on the number of electrons of an atom, Bragg angle θ , the wavelength λ and the temperature factor (B_j), as shown in equation (2-3).⁸⁸ For a given atom j , $f_0 = Z_j$, the atomic number of atom j .

$$f_j = f_0 \exp(-B_j \sin^2 \theta / \lambda^2) \quad (2-3)$$

The temperature factor describes the thermal vibration of each atom in crystal, which is given by equation (2-4); U_j is the mean-square amplitude of the vibration of atom j around its equilibrium position. It is a function of temperature.

$$B_j = 8\pi^2 U_j \quad (2-4)$$

The structure factor $F(hkl)$ expresses the combined scattering of X-rays for all atoms in the unit cell in the (hkl) direction. It depends on the position of atoms (x_j, y_j, z_j) and their atomic scattering factors, as shown in equation (2-5).

$$F(hkl) = \sum_{j=1}^N f_j \exp[2\pi i(hx_j + ky_j + lz_j)] \quad (2-5)$$

Furthermore, the electron density distribution within a crystal can be expressed in a similar equation (2-6):

$$\rho(x, y, z) = \frac{1}{V} \sum_h \sum_k \sum_l F_{hkl} \exp[-2\pi i(hx + ky + lz)] \quad (2-6)$$

Where $\rho(x, y, z)$ is the electron density at a position (x, y, z) in the unit cell and V is the volume of the unit cell. In mathematical terms, the electron density is defined as the Fourier transform of the structure factors (equation 2-5) and vice versa. This relationship means that if the structure factors are known, the electron density distribution in the unit cell can be calculated, thereby the atomic positions.⁸⁹

The energy associated with a wave, in terms of intensity of the scattered wave, is proportional to the square of the amplitude of the wave. Since the amplitude of the wave is $|F(hkl)|$, the experimentally observed intensity is proportional to $|F(hkl)|^2$.

$$I_0 \propto |F_0(hkl)|^2 \quad (2-7)$$

Thus, the magnitude of structure factor can be written as:

$$|F_0(hkl)| \propto \sqrt{I_{hkl}} \quad (2-8)$$

It is a challenge to calculate the atomic positions only from the measured magnitudes of the structure factors (intensities), known as the “phase problem”, because the phase information is lost (see equation 2-8). Two main methods, the Patterson method and the direct method, are available to solve this problem.⁸⁸

Patterson reported Fourier series which was deduced directly from the experimental intensity data in 1934.⁹⁰ The results cannot be expressed as a set of atomic positions since the phase information is not available. However, a collection of interatomic vectors can be obtained from a common origin. Those atoms which are much heavier than their neighbors can be located easily because the corresponding peaks are much more intense. Structure factors of same type of atoms can be calculated and the approximate positions of a certain number of atoms are deduced. Therefore, the other atoms can be located by successive iterations via the interatomic vectors.⁹¹ The Patterson method is good for solving crystal structures containing heavy element. However, in the cases of large numbers of atoms in the unit cell or the elements having similar scattering factors, such as organic molecules, it is very difficult to identify specific atoms.

The direct method solves the phase problem directly using the relations between the intensity of reflections and the phases. Through statistical analysis of the amplitude of structure factors, information of the phases can be partially reconstituted and an approximate structure can be deduced. Direct method is usually selected to solve structures using the SHELXTL package.⁹²

2.2.2 Single crystal methods

The main use of single crystal methods is to find out the unit cell, space group and a full crystal structure solution based on the measured intensities of reflections. A good quality crystal with sufficient size (20 μm –400 μm) is selected and mounted on a glass fiber for data collection. Two area-detector systems, charge couple device (CCD) and imaging plate

(IPDS) are widely used at present. In the Department of Chemistry at University of Waterloo, the data collection is performed with a Bruker Smart Apex CCD detector with the radiation of graphite-monochromatized Mo $K\alpha_1$, as shown in Fig. 2.4.

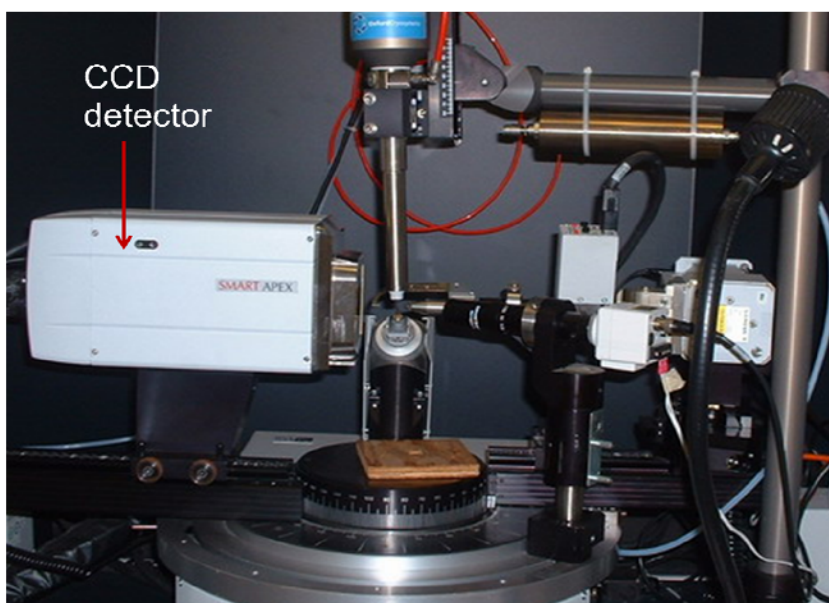


Fig. 2.4 SMART Apex CCD in the Department of Chemistry, Waterloo.

The SMART software, integrated with APEX2, is employed for data collection and unit cell determination.⁹³ The raw data is corrected using the SAINT program integrated in the APEX2⁹⁴ because the intensities depend on several factors, not only on the structure factor as shown in equation (2-6). This correction process is called “data reduction”. It includes the corrections of polarization factor, Lorentz factor, absorption factor and extinction.⁹⁵ The intensity of reflections is reduced because non-polarized X-ray beams become partly polarized on reflection; the intensity reduction depends on the angle of reflections. The Lorentz factor correction depends on the type of measurement. These two

corrections are generally combined and noted as LP-correction. When X-rays penetrate the materials, part of X-rays are absorbed by materials (particularly for the compounds containing heavy elements), thus the intensity of the reflections gets reduced. This reduction depends on the atomic scattering factor and the radiation wavelength. The absorption correction can be done by the SADABS⁹⁴ or XPREP⁹⁶ program. The extinction correction is mainly aimed at the reflections with high intensities. For powder XRD, the extinction factor affects the reflections with high intensities and low diffraction angles. After data reduction, the crystal structure can be solved and refined by utilizing the SHELXTL package.⁹²

The whole procedure for solving a single crystal structure is summarized below:

- After data collection, the size and shape of the unit cell is determined from rotation photography on the diffractometer.
- The reflections are indexed. The Bravais lattice and the translation symmetry elements can be determined from the systematic absences; therefore, the space group is determined.
- The intensities of the indexed reflections are measured and saved as a data file. Data reduction is applied to correct a variety of effects.
- The observed structure factors (F_o) are obtained based on the square roots of corrected intensity data (equation 2-8).
- Phase problem can be solved by Patterson methods or direct methods; hence atomic positions can be deduced from the measured electron density map.

- Once the atoms in a structure have been located, the calculated structure factors (F_c) are determined for comparison with F_o magnitudes. The positions of the atoms are refined using least-squares methods.⁸⁸

The residual index R_I and weighted factor (wR_2) provide measure of the difference between the observed and calculated structure factors, therefore they are usually used to evaluate how well the structure is refined. They are defined as equations of (2-9) and (2-10), where w is the weight factor and related to the precision of $|F_o(hkl)|$. A good structure determination should have low R values and low standard deviations of the atomic positions, meanwhile the bond lengths calculated from these positions must also be reasonable.

$$R_1 = \frac{\sum (|F_o| - |F_c|)}{\sum |F_o|} \quad (2-9)$$

$$wR_2 = \sqrt{\frac{\sum w(F_o^2 - F_c^2)^2}{\sum w(F_o^2)}} \quad (2-10)$$

2.2.3 Powder X-ray diffraction

Powder X-ray diffraction (PXRD) is usually used as a fingerprint method to detect the presence of a known phase by checking the frequently updated libraries of powder diffraction patterns, such as ICSD (the Inorganic Crystal Structure Database) and ICDD (the International Center for Diffraction Data). The PXRD is useful for qualitative analysis, like checking the purity of the sample approximately. However, it cannot detect an amorphous phase or impurities of less than 5%. Powder diffraction can be used to solve crystal structures

with simple and high symmetry. It may be difficult to index the overlapping peaks if the structure is complex.⁸⁹

The PXRD method, invented by Debye and Scherrer, involves the diffractions of monochromatic beams of X-rays by a polycrystalline powder sample. This polycrystalline sample is comprised of a large number of randomly oriented single crystals, with a particle size ranging from 1 μm to 10 μm . Thus, there are always a large number of lattice planes (hkl) with the angle θ to satisfy the Bragg's Law (equation 2-2).⁹¹ Suitable oriented micro-crystals diffract the beams and form a cone of angle 2θ to the incident beam, as shown in Fig. 2.5.

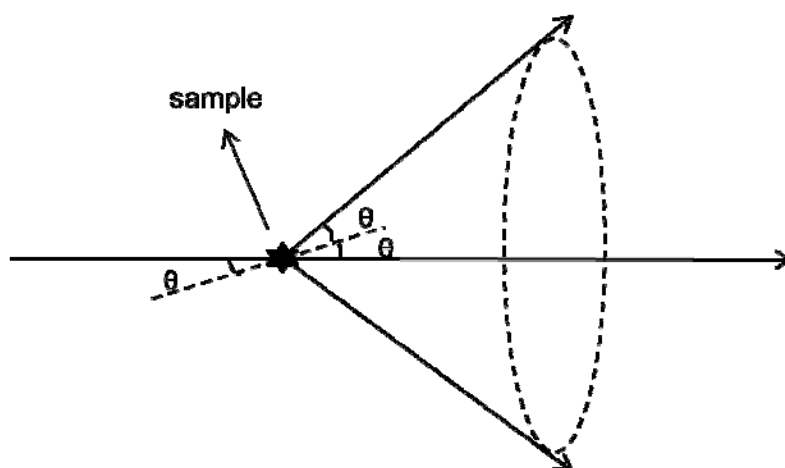


Fig. 2.5 The formation of a cone of diffracted beams in PXRD.

The classical Debye-Scherrer camera is hardly used now because of the long exposure time and the inaccurate measurements on the images. At present, many diffractometers can work quickly and interpret the data automatically. Examples include a proportional counter, linear detector or curved detector.⁹¹ Our lab is equipped with the Inel

XRG 3000 powder diffractometer with position sensitive (curved) detector, as shown in Fig. 2.6. For an unknown polycrystalline sample, PXRD can be used to determine the detailed structure information, such as lattice parameter, atomic position and thermal displacement parameters, by using Rietveld refinement, if an appropriate model is selected.

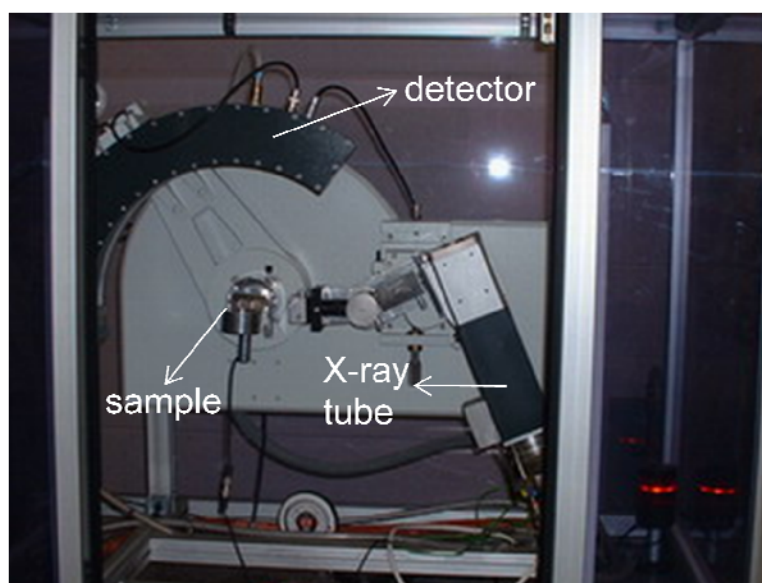


Fig. 2.6 Inel XRG 3000 powder X-ray diffractometer.

Rietveld refinement is a technique developed by Hugo Rietveld for refining crystal structures from neutron diffraction data.⁹⁷ Malmros and Thomas extended this method to powder X-ray diffraction profiles using different peak-shape functions.⁹⁸ The Rietveld analysis is based on profile refinement of the diffraction lines. From comparison with similar compounds, an initial structural model is proposed. This model is refined by point-by-point comparison between calculated and experimental profiles. From the peak positions, the unit cell parameters are deduced; a space group can be determined based on the peak indexing and systematic absences. The proposed structure is modified by changing atomic positions

and thermal displacement parameters of each atom, refined until the calculated pattern achieves a best-fit match with the measured pattern.⁹¹ This method works well if a suitable trial structure is chosen. For instance, the refinement will be conducted smoothly and converged easily if the unknown structure is only a slight modification of a known structure, like the cases of $\text{Re}_3\text{Sn}_x\text{As}_{7-x}$ and $\text{Mo}_3\text{Sb}_{7-x}\text{Te}_x$, which will be discussed in the following chapters.

The fit of the calculated pattern with the observed pattern can be estimated numerically, in terms of agreement indices (R), including the profile R_p , the weighted profile R_{wp} and the structure factor profile R_F . The equations of various R values are listed below, where y_{io} is the observed intensity at step i , and y_{ic} is the calculated intensity. w_i is weighing factor, defined as equation (2-13), where σ_{ip} is the standard deviation associated with the peak intensity and σ_{ib} is the standard deviation associated with the background intensity.⁸⁵ In both equations of R_p and R_{wp} , the numerator is the value that should be minimized during Rietveld refinement. R_F is of considerable use because it depends on the fit of structural factors more than profile parameter. R values are useful to evaluate the quality of a refinement, but they cannot be over-interpreted. The most important criteria for judging the quality of a refinement are the fits between the calculated pattern and observed data and the reasonable structure model, e.g. the atomic positions, bond distance and bond angle, etc.⁹⁹

$$R_p = \frac{\sum |y_{io} - y_{ic}|}{\sum |y_{io}|} \quad (2-11)$$

$$R_{wp} = \sqrt{\frac{\sum w_i (y_{io} - y_{ic})^2}{\sum w_i y_{io}^2}} \quad (2-12)$$

$$w_i = \frac{1}{\sigma_i^2} = \frac{1}{\sigma_{ip}^2 + \sigma_{ib}^2} \quad (2-13)$$

$$R_F = \frac{\sum |I_{hkl}(obs)^{1/2} - I_{hkl}(calc)^{1/2}|}{\sum (I_{hkl}(obs))^{1/2}} \quad (2-14)$$

The Rietveld refinements presented in this thesis were conducted using the GSAS (general structure analysis system) software^{100, 101} via the graphical user interface EXPGUI.¹⁰² The PXRD data used were all collected on the Inel diffractometer for over 15 hours and an instrument calibration was usually performed before data collection.

2.2.4 Energy dispersive X-ray (EDX) analysis

Energy dispersive X-ray spectroscopy is an analytical technique for elemental analysis of a sample, which is always in conjunction with scanning electron microscopy (SEM). When the incident high energy beam strikes the surface of materials, the characteristic X-rays will be emitted from a specimen. An atom within the sample has ground state electrons in discrete energy levels bound to the nucleus. The incident beam will eject an electron from the inner shell and leave a hole where the electron was. Hence, the electron from the higher energy level, outer shell, will fill this hole and release the energy difference between these two levels in the form of X-rays. Since the released energy is associated with the unique atomic structure, the elements can be identified by analyzing the emitted X-rays.

The energy of the incident beam is typically in the range of 10 keV–20 keV. The number and energy of the emitted X-rays can be measured by an energy dispersive spectrometer. An example spectrum of $\text{Re}_3\text{Sn}_{0.4}\text{As}_{6.6}$ is shown in Fig. 2.7. The x -axis is the X-ray energy scale, along which each peak corresponds to a particular element. The y -axis is an arbitrary pixel count, associated with the energy of emitted X-rays. The element peaks for analysis have been marked in red; the sum of the area under each element peak is proportional to elemental quantities.

The EDX analyses in this thesis were performed on a SEM (LEO 1530) integrated with EDX Pegasus 1200 in the Department of Chemistry at the University of Waterloo.

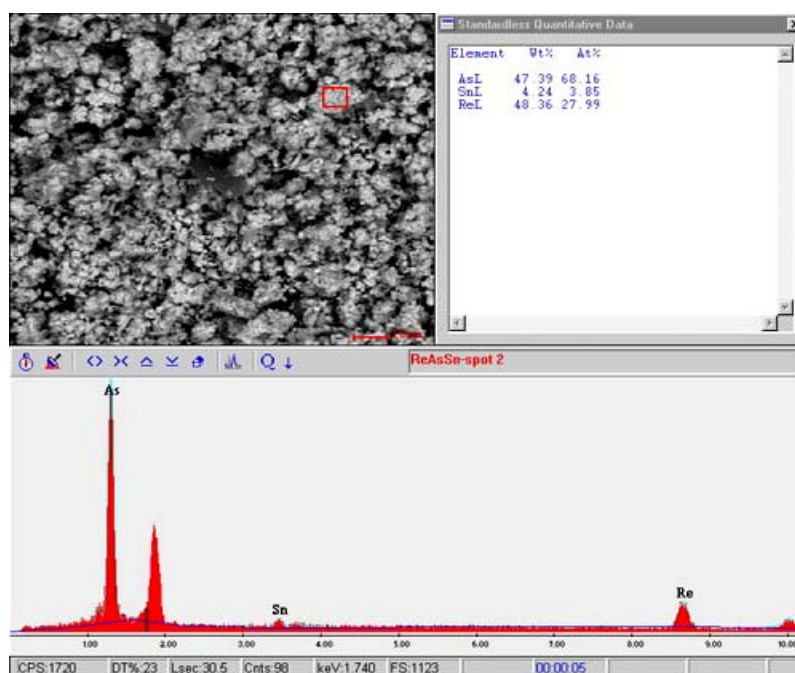


Fig. 2.7 An example of EDX spectrum.

2.2.5 Thermal analysis

Thermal analysis is often performed to investigate the thermal stability of a compound as a function of temperature. The thermal analysis methods used in my thesis are thermogravimetry (TG) and differential scanning calorimetry (DSC) techniques. Both of them can be conducted simultaneously on a computer-controlled NETZSCH STA 409PC Luxx instrument under a flow of argon, as shown in Fig. 2.8. A DSC head on a silver block is located in a furnace. The silver block ensures the complete and even heat dispersion. Two separate heaters underneath connect with the silver block of the reference holder and sample holder, respectively. The current required for keeping the differential thermocouple balance ($\Delta T = 0$) is measured and recorded with an auto-controlled program.

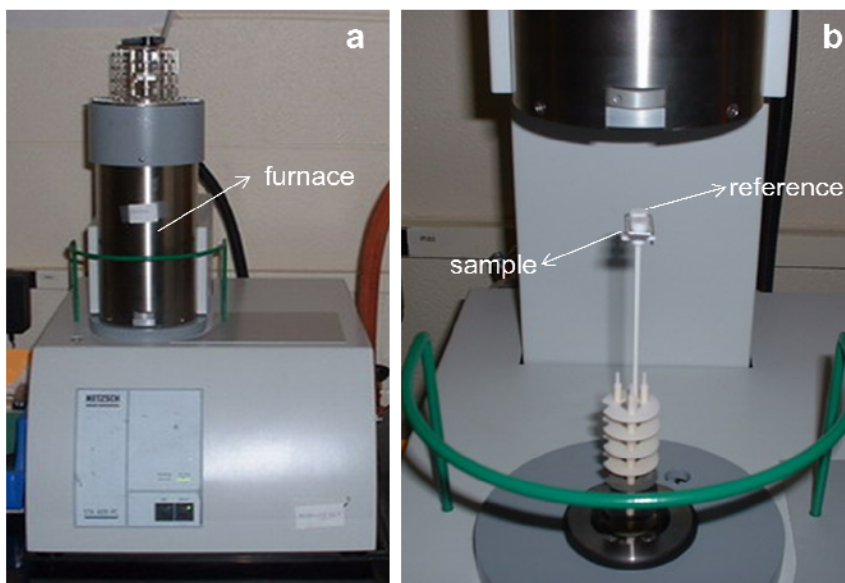


Fig. 2.8 (a) NETZSCH STA 409PC Luxx apparatus; (b) DSC head within furnace.

Thermogravimetric analysis (TGA) is usually used to measure the weight/mass changes of a sample as a function of temperature or time. A small amount of sample (around

30 mg ~ 50 mg) is put into an alumina crucible and placed on the sample holder pan, which is attached to a sensitive microbalance assembly. The balance will monitor the weight change continuously during the heating procedure. The profile is analyzed for the percentage of weight loss with the temperature change.

DSC is a technique to measure the difference of the amount of heat required to increase the temperature of a sample and reference as a function of temperature or time. The temperatures of sample and reference are maintained as the same during the heating procedure. Extra heat is input to sample or reference in order to maintain this balance, therefore enthalpy changes are measured directly. The main application of DSC is to detect phase transitions, such as melting, decomposition, or crystal structure change. The DSC curves present the changes of heat flow versus temperature, thus one can distinguish between exothermic and endothermic processes. For example, when materials start melting or decomposing at a certain temperature, more heat is absorbed to maintain the temperature balance, resulting in an endothermic peak. Conversely, with any procedure that involves heat generation, like crystallization, an exothermic peak will result, as illustrated in Fig. 2.9.

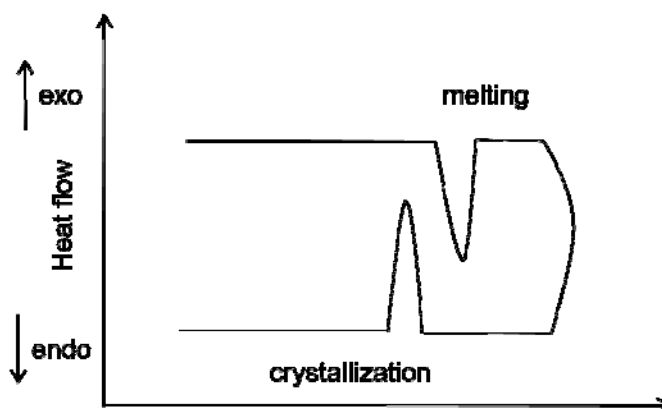


Fig. 2.9 Schematic drawing of DSC curve for endothermic and exothermic reactions.

2.2.6 Electronic structure calculation

Because of increasing computation capabilities, more and more complicated and time-consuming electronic structure calculations can now be realized. This technique already plays an important role in describing and predicting electrical properties of materials by modeling the band structures.

Band calculation techniques generally involve two main strategies. One uses a trial wave function formed by linear combination of basis functions, like plane waves in the NFE (nearly free electrons) method and orthogonalized plane waves in the OPW (orthogonalized plane wave) method. The other expands the wave function into a set of energy-dependent partial waves and applies a matching condition for partial waves at the muffin-tin sphere, such as APW (augmented plane wave) method and KKR (Korringa-Kohn-Rostoker) method. Both approaches have their advantages and disadvantages. The first two methods use energy-independent basis functions, allowing a fast computation in solving the secular equations; however a proper choice of basis function is important to construct a small basis set. The last two methods involve a complicated, non-linear energy dependent secular matrix. They are capable of calculating more accurately, but require a substantial computational effort to obtain self-consistent calculations.¹⁰³ In 1975, Andersen published the LMTO (linear muffin tin orbital) method for solving the band structure in a more efficient way.¹⁰⁴ The LMTO method was developed to combine the desired features of fixed-basis and partial-wave methods and has been recognized as one of the most efficient method with accuracy and a short computation time. The electronic structure calculations in this thesis were conducted via LMTO47c program installed on the server with LINUX operating system.¹⁰⁵

As stated above, KKR, APW and LMTO methods all involve muffin-tin approximation (MTA).¹⁰⁶ A crystalline compound is regarded to have closed packed atoms, thus the potential about each atom is weakly anisotropic. The atoms were considered to be non-overlapping, atom-centered spheres, so-called “muffin-tin” spheres. A potential is taken to be spherically symmetric inside and a constant outside in interstitial region, giving the approximate total energy as:

$$\text{For } \vec{r} \text{ inside sphere at } \vec{R}: \quad V(\vec{r}) = V_R \left| \vec{r} - \vec{R} \right| \quad (2-15)$$

$$\text{For } \vec{r} \text{ in interstitial region:} \quad V(\vec{r}) = V_0 \quad (2-16)$$

The LMTO method is based on density functional theory (DFT), which includes two fundamental theorems, provided by Kohn and Hohenberg in 1964.¹⁰⁷ One theorem states the *ground-state energy from Schrödinger’s equation is a unique functional of the electron density*. The second theorem states *the electron density that minimizes the energy of the overall functional is the true electron density corresponding to the full solution of the Schrödinger equation*. The second theorem indicated one could vary the electron density to achieve the minimum energy if the functional form were known. Kohn and Sham solved this problem in 1965. They showed that the right electron density can be obtained by solving a set of equations, in which each equation only involves a single electron, called Kohn-Sham equation.¹⁰⁸ Both Schrödinger equation (2-17) and Kohn-Sham equation (2-18) are described below:

$$\left[-\frac{\hbar^2}{2m} \sum_{i=1}^N \nabla_i^2 + \sum_{i=1}^N V(r_i) + \sum_{i=1}^N \sum_{j < i} U(r_i, r_j) \right] \Psi = E \Psi \quad (2-17)$$

In equation (2-17), m is the electron mass; the three terms in brackets in order are kinetic energy of each electron, the interaction energy between each electron and all the atomic nuclei, and the interaction energy between different electrons, constituting the Hamilton operator. Ψ is the electronic wave function, which is a function of the spatial coordinates of each electron. E is the ground state energy of the electrons.

$$\left[-\frac{\hbar^2}{2m} \nabla^2 + V(r) + V_H(r) + V_{XC}(r) \right] \psi_i(r) = \varepsilon_i \psi_i(r) \quad (2-18)$$

The Kohn-Sham equation is similar to Schrödinger equation except missing the summations, because the solution of Kohn-Sham equation is a single electron wave function depending on only spatial variables. V is the interaction between an electron and the collection of atomic nuclei; V_H is the Hartree potential and describes the Coulomb repulsion between an electron and all the other electrons. V_{XC} defines exchange and correlation contributions.

As the MTA mentioned above, the exact solutions to the Kohn-Sham equation for muffin-tin potential inside and outside sphere can be expressed as (2-19) and (2-20), respectively:

$$\left[-\frac{1}{2} \nabla^2 + V(\vec{r}) \right] \psi_i(\vec{r}) = \varepsilon_i \psi_i(\vec{r}) \quad (2-19)$$

$$\left[-\frac{1}{2} \nabla^2 + V_0 \right] \psi_i(\vec{r}) = \varepsilon_i \psi_i(\vec{r}) \quad (2-20)$$

Once the eigenvalue ε is known, ψ can be solved numerically. Anderson chose to fix ε values to construct the basis functions and deduce the linear combination functions and thereby showed that a method can be considered linear in energy, so called “linear muffin-tin orbital” method.¹⁰⁴

A further simplification is achieved using atomic-sphere approximation (ASA).¹⁰⁴ The muffin-tin spheres are made larger to slightly overlap and their total volume equals to the volume of the system. Hence, the overlapping volume equals the interstitial region volume. The LMTO calculation becomes more efficient by neglecting the overlapping and interstitial part, and the error can be removed by using combine-correction theory.¹⁰⁹

One of the main output results from band structure calculations is the density of states (DOS). DOS is a plot of number of energy levels, $N(E)$, as a function of energy E . In a metal, the conduction band is partially filled, hence electrons can move freely and lead to high electrical conductivity. An insulator has a full valence band and empty conduction band, separated by a large band gap of > 3 eV. Few electrons can be excited into the conduction band by thermal energy; therefore the electrical conductivity of an insulator is negligible. A semiconductor is an intermediate case, which possess a similar band structure to the insulator but with a smaller band gap range of < 3.0 eV. Electrons can be promoted into the empty band by sufficient thermal energy.¹¹⁰ The scheme of density of states of metal and insulator is shown in Fig. 2.10.

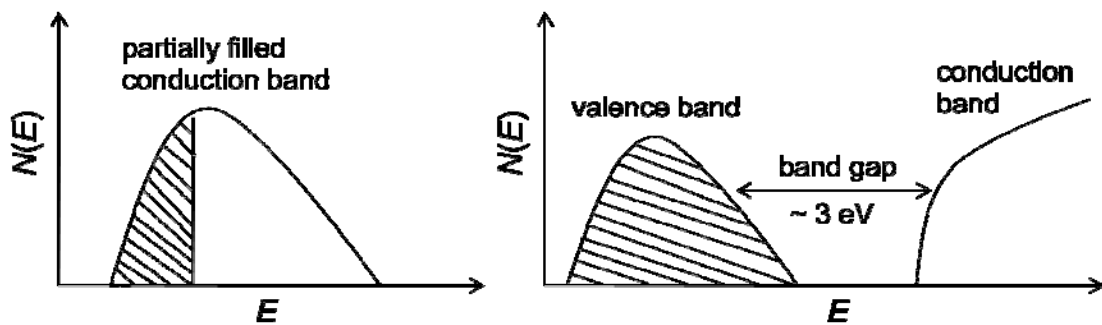


Fig. 2.10 Density of States (DOS) of a metal (left) and an insulator (right). The occupied levels are shown by shading.

2.2.7 Seebeck coefficient measurement

The Seebeck coefficient of a sample was measured between the temperatures of 300 K to 550 K in our laboratories on the MMR SB-100 Seebeck system, as shown in Fig. 2.11.

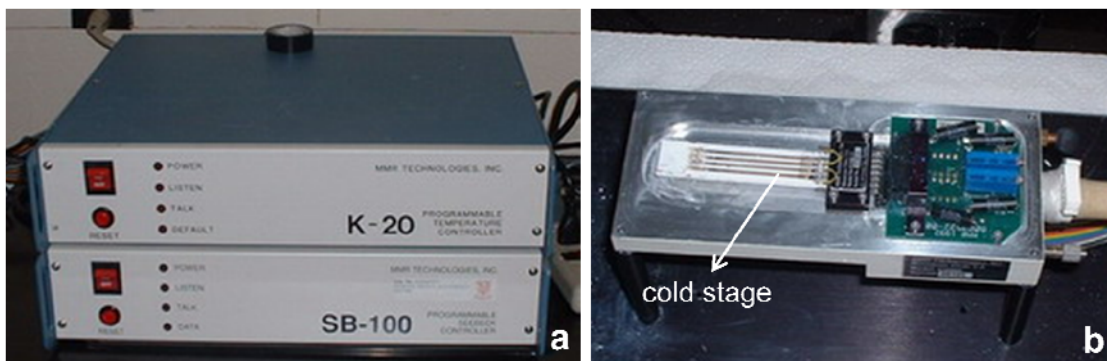


Fig. 2.11 (a) Programmable Seebeck controller (SB-100) and temperature controller (K-20); (b) Seebeck system dewar with MMR cold stage mounted on the top.

The Seebeck stage (Fig. 2.12) is placed on the top of the cold stage, which provides a given stable temperature for the measurement and is controlled by a K-20 apparatus. Two pairs of thermocouples, reference (constantan: Cu/Ni = 55/45 wt%) and sample pellet

($5*1*1\text{mm}^3$), are bound to the stage with Leitsilber 200 silver paint (from Ted Pella Inc) on both sides to make connections. A heater, controlled by SB-100, is located close to the working junctions of each pair and remote from the reference junctions of each pair.

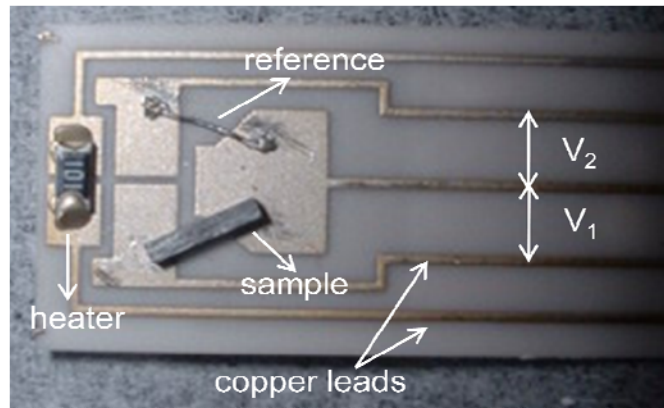


Fig. 2.12 Picture of Seebeck stage.

When power (P) is applied to the heater, a temperature gradient (ΔT) will be created between the working and reference junctions because they have different distances from the heater. Therefore, different thermo-voltages, V_1 and V_2 , will be generated in each pair, as listed below, where S_1 and S_2 are the Seebeck coefficient of the sample and the reference, respectively:

$$V_1 = S_1 * \Delta T (P)$$

$$V_2 = S_2 * \Delta T (P)$$

With the known Seebeck coefficient of the reference (S_2) and the same temperature difference, the sample's unknown Seebeck coefficient (S_1) can be deduced as: $S_1 = S_2 V_1 / V_2$. However, since a small temperature differential is applied, the values of V_1 and V_2 are small, resulting in a low accuracy measurement in view of the instrumental errors and any unwanted

effects from wires and connections, etc. These effects can be eliminated by taking measurements at two different temperatures using different power settings. Considering the offset voltage ΔV , the real values of V_1 and V_2 at different temperature (represented by power P_1 and P_2) are given as:

$$V_1 (P_1) = S_1 * \Delta T (P_1) + \Delta V_1$$

$$V_2 (P_1) = S_2 * \Delta T (P_1) + \Delta V_2$$

$$V_1 (P_2) = S_1 * \Delta T (P_2) + \Delta V_1$$

$$V_2 (P_2) = S_2 * \Delta T (P_2) + \Delta V_2$$

Subtracting the last two equations from the first two equations above, S_1 can be deducted as:

$$S_1 = S_2 [V_1 (P_1) - V_1 (P_2)] / [V_2 (P_1) - V_2 (P_2)]$$

Thus, the offset voltages are removed, assuming they are independent of power P .

2.2.8 Electrical conductivity measurement

The electrical conductivity was measured on a homemade instrument (Fig. 2.13) by the four-point method. Electrical conductivity could be measured with a two-point method. However, when measuring a low resistance, the contact resistance becomes a significant source of error. A four-point method eliminates this factor by only measuring the voltage between the middle contacts. In this thesis, the measurements were conducted under vacuum by a four-point method, and the measurement temperature range is 50 K–320 K. A helium compressor was employed to cool down the sample chamber. The results of the voltage measurement between the two middle contacts with temperature dependence were recorded, and the resistance can be calculated as $R = V/I$. Then, the electrical conductivity is obtained

by $\sigma = L/(R \cdot A)$, where A is the cross-section area of the pellet and L is the distance between the middle contacts, as shown in Fig. 2.14.

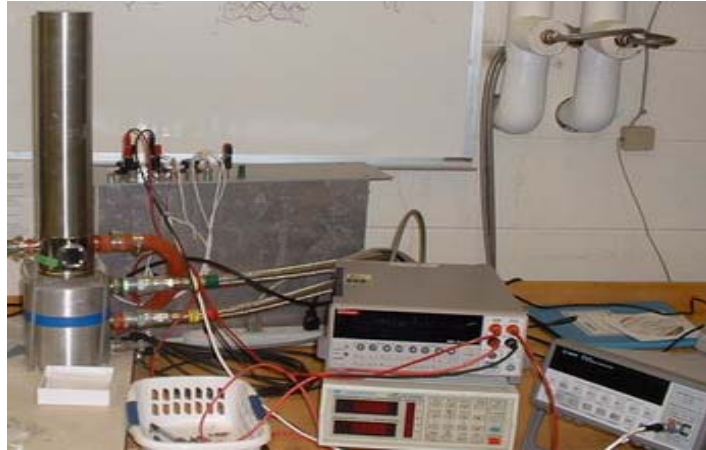


Fig. 2.13 Homemade electrical conductivity measurement apparatus.

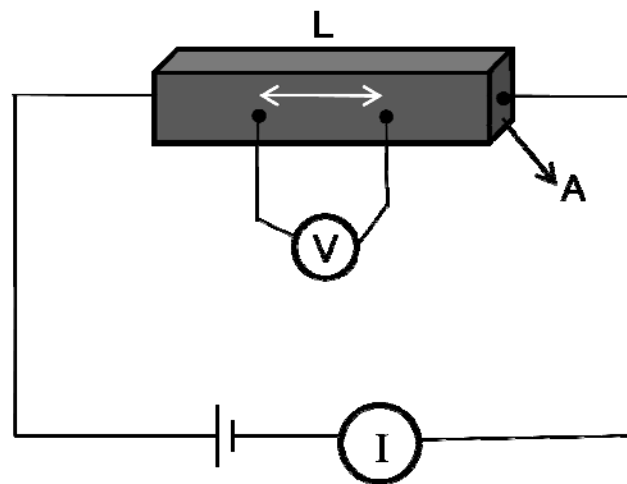


Fig. 2.14 Schematic drawing for four-point measurement method.

2.2.9 Power factor measuring system

Since July 2009, our laboratory has been equipped with the ULVAC ZEM-3 instrument (Fig. 2.15), which can measure both the Seebeck coefficient and the electrical conductivity simultaneously.



Fig. 2.15 (a) ULVAC ZEM-3 measuring system; (b) the sample placed between the electrodes with two probes contacts.

The conceptual diagram (Fig. 2.16) indicates that two probes A and B contacted to the sample pellet can measure the voltage and temperature differences between A and B. Thus, the Seebeck coefficient and the resistance value R (with known constant current) between A and B can be calculated. The integrated microscope accessory can assist in measuring the dimensions of the pellet and the distance between the two probes accurately. Therefore, the electrical conductivity can be calculated.

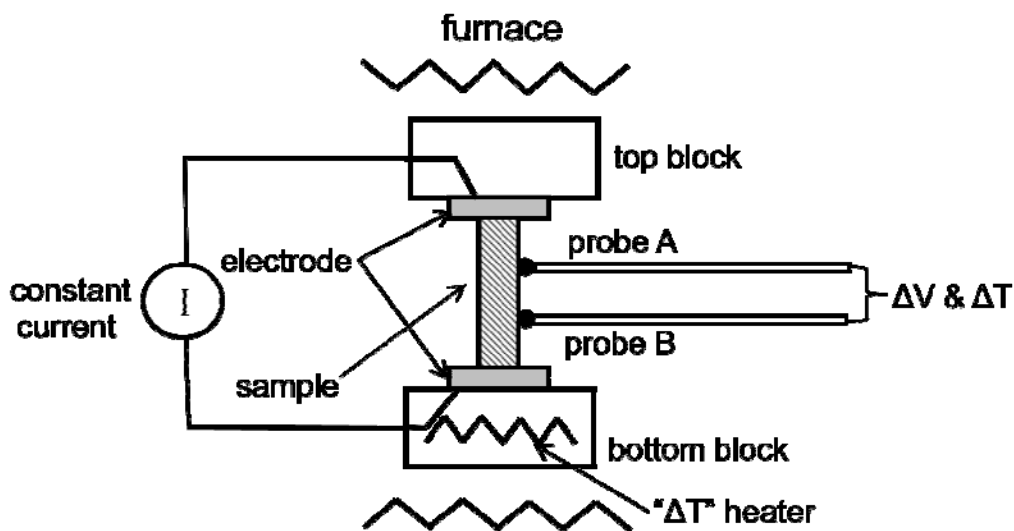


Fig. 2.16 conceptual diagram for measurement of voltage and temperature differences.

2.2.10 Thermal conductivity measurement

The thermal conductivity is described in equation (2-21).¹¹¹ The density ρ is easily calculated by mass over volume. Specific heat can, in principle, can be determined with the DSC system. The thermal diffusivity α is measured by laser flash method. In the laser flash technique, one face of a sample pellet is irradiated by a short laser pulse and the temperature rises on the opposite face. The temperature is monitored using IR detector. The thermal diffusivity can be calculated from the equation (2-22), where L is the thickness of sample and $t_{1/2}$ is the time required to reach half of the maximum temperature increase.²³

$$\kappa = \alpha \times \rho \times C_p \quad (2-21)$$

$$\alpha = 0.1388 \left(\frac{L^2}{t_{1/2}} \right) \quad (2-22)$$

Since the DSC system in our laboratory cannot reliably determine the specific heat, we usually calculate the specific heat by the Dulong-Petit Law,¹¹² as expressed in equation (2-23), wherein R is the gas constant and M is the averaged molar mass of the substance. Dulong and Petit found empirically that specific heat capacity for a number of substances was close to a constant, when divided by their molar mass. Thus they provided a simple relation to predict the specific heat of a solid substance at high temperature.

$$C_p = \frac{3R}{M} \quad (2-23)$$

The experiment was conducted on the Flash Line 3000 thermal diffusivity system (ANTER Corp.) under argon, as shown in Fig. 2.17. Liquid nitrogen was added frequently to cool down the IR detector. The values of $t_{1/2}$ were recorded at different temperatures and the thermal diffusivity was calculated automatically with the measured thickness of pellet.



Fig. 2.17 Flash Line 3000 for thermal diffusivity measurement.

2.3 Physical properties measurement at Clemson University

Because we are not equipped with a hot-pressing apparatus and the samples cannot form high density pellets with the cold press tool (Weber-Pressen Press), we sent part of our samples to the Complex and Advanced Materials Laboratories (CAML) at Clemson University for the preparation of hot-pressed pellets and subsequent physical property measurements.

At Clemson, each sample was firstly cold-pressed into a pellet, then placed into the graphite die and typically pressed under 175 MPa at 993 K with Mo rods for one hour in the Thermal Technology HP20-4560-20 press, finally forming a pellet with around 92% – 98% of the ideal density.

The Seebeck coefficient and electrical conductivity were determined simultaneously on Clemson's ULVAC ZEM-2 from room temperature to 1023K, which has the same working principle as the ZEM-3, as described in section 2.2.9. A prism shape pellet with dimensions of about $2 \times 2 \times (6-8)$ mm³ is cut from the hot-pressed round pellet for the ZEM-2 measuring system. The thermal conductivity data was calculated from the material density (ρ), thermal diffusivity (α) and specific heat (C_p) via equation (2-21). Thermal diffusivity was measured using a laser flash system (NETZSCH LFA 457). Specific heat was measured on NETZSCH DSC system by ratio method using a reference material with a known $C_{p(r)}$, as shown in equation (2-24),¹¹³ where $m_{(r)}$ and $m_{(s)}$ are the mass of reference and sample, respectively..

$$C_{p(s)} = \frac{m_{(r)}}{m_{(s)}} \times \frac{DSC_{(s)} - DSC_{baseline}}{DSC_{(r)} - DSC_{baseline}} \times C_{p(r)} \quad (2-24)$$

3 Thermoelectric properties of Mo₃Sb₇ series samples

Mo₃Sb₇ is one of the compounds that have the Ir₃Ge₇ (R₃E₇) structure type. Mo₃Sb₇ attracted our attention with its potential to be a semiconductor. Our group commenced to investigate Mo₃Sb_{7-x}Te_x as a new thermoelectric material in 1998 and proved that the semiconducting property can be achieved by Sb/Te exchange.⁶² The further optimizations, including the intercalation of different transition metal atoms¹¹⁴ and varying the Sb/Te ratio,¹¹⁵ were performed to advance the thermoelectric properties in this thesis.

3.1 Sample synthesis

All samples were prepared from the elements: molybdenum (powder, -100 mesh, 99.95%), antimony (powder, -100 mesh, 99.5%), tellurium (broken ingot, 99.99%), iron (powder, < 10 μm, 99.9%) and nickel (powder, -200 mesh, 99.9%) were acquired from Alfa Aesar; manganese (powder, -50 mesh, 99.9%) and cobalt (powder, -100 mesh, 99.9%) were purchased from Aldrich. All the elements were weighed in the desired stoichiometric ratio, then mixed and loaded into silica tubes in an argon-filled glove box. These tubes were evacuated and sealed under vacuum, followed by heating in resistance furnaces at 993 K over a period of ten days. The prepared samples were thoroughly ground and analyzed via X-ray powder diffraction, utilizing an Inel powder diffractometer. If any side product peaks were found, e.g. MoTe₂, NiTe₂, or unreacted Sb, the samples were reloaded into the new silica tubes to repeat the heating profile. In most cases, these peaks can be eliminated during a second heating run. Only samples without any detectable side products were sent to Clemson University for the preparation of hot-pressed pellets and physical property measurements.

The carrier concentrations of the sample are directly related to the Te content. We synthesized the samples of $A_y\text{Mo}_3\text{Sb}_{7-x}\text{Te}_x$ ($A = \text{Fe}, \text{Ni}$) with $x = 1.5, 1.6, 1.7$ and $y \leq 0.10$. Samples with $x > 1.7$ usually included traces of MoTe_2 . In addition, complete filling with transition metal atoms A into the empty Sb_2 cubes corresponds to $A_{0.5}\text{Mo}_3\text{Sb}_{7-x}\text{Te}_x$, because there is only one cube for every two Mo_3Sb_7 units. However, we could not make pure samples with $y > 0.10$, as the side product peaks of NiTe_2 started to appear in $\text{Ni}_y\text{Mo}_3\text{Sb}_{7-x}\text{Te}_x$ compounds. Even though the entire series compounds with systematical varying A and Te compositions were prepared and sent to Clemson University, not all of them were tested. The results we received and analyzed in the following section are from the compounds of $\text{Ni}_{0.08}\text{Mo}_3\text{Sb}_{5.5}\text{Te}_{1.5}$, $\text{Ni}_{0.10}\text{Mo}_3\text{Sb}_{5.5}\text{Te}_{1.5}$, $\text{Mo}_3\text{Sb}_{5.4}\text{Te}_{1.6}$, $\text{Ni}_{0.06}\text{Mo}_3\text{Sb}_{5.4}\text{Te}_{1.6}$, $\text{Ni}_{0.08}\text{Mo}_3\text{Sb}_{5.4}\text{Te}_{1.6}$, $\text{Ni}_{0.05}\text{Mo}_3\text{Sb}_{5.3}\text{Te}_{1.7}$, $\text{Fe}_{0.05}\text{Mo}_3\text{Sb}_{5.5}\text{Te}_{1.5}$, $\text{Fe}_{0.05}\text{Mo}_3\text{Sb}_{5.4}\text{Te}_{1.6}$ and $\text{Fe}_{0.05}\text{Mo}_3\text{Sb}_{5.3}\text{Te}_{1.7}$.

3.2 Crystal structure

$\text{Mo}_3\text{Sb}_{7-x}\text{Te}_x$ crystallizes in the Ir_3Ge_7 structure type with the space group $\overline{Im}3m$, wherein the Sb and Te atoms occupy the Ge sites. The detailed crystal structure information has been reported previously,⁶² thus the general structure description is provided herein. Mo atoms are coordinated with eight Sb/Te atoms in form of a square antiprism. Two such prisms share a face formed by Sb1/Te1 atoms, resulting in Mo–Mo bonding. The eight Sb_2 atoms form an empty cube, whose center may be occupied by a transition metal atom of appropriate size. Each face of the Sb_2 cube is part of a Mo (Sb/Te)₈ square antiprism. In general, the chains of $\text{Mo}_3\text{Sb}_{7-x}\text{Te}_x$ are comprised of Sb_2 cube–Mo–Sb1/Te square–Mo– Sb_2

cube–Mo... Three such chains inter-penetrate each other at the Sb2 cubes to construct a three dimensional structure. The overview and a fragment of a chain of the crystal structure are shown in Fig. 3.1.

There are three different interactions between the main group elements. The first is a Sb–Sb single bond distance of 2.9Å, which connects the Sb2 cubes pairwise in three dimensions. The second has an intermediate distance of 3.1Å between the Sb2 atoms along the cube edges. The third one is weak with 3.3 Å between the Sb1/Te atoms. Small transition metal atoms A ($A = \text{Mn, Fe, Co, Ni, Cu}$) can fit into the Sb2 cubes, forming A–Sb2 bonds of 2.6–2.7 Å.

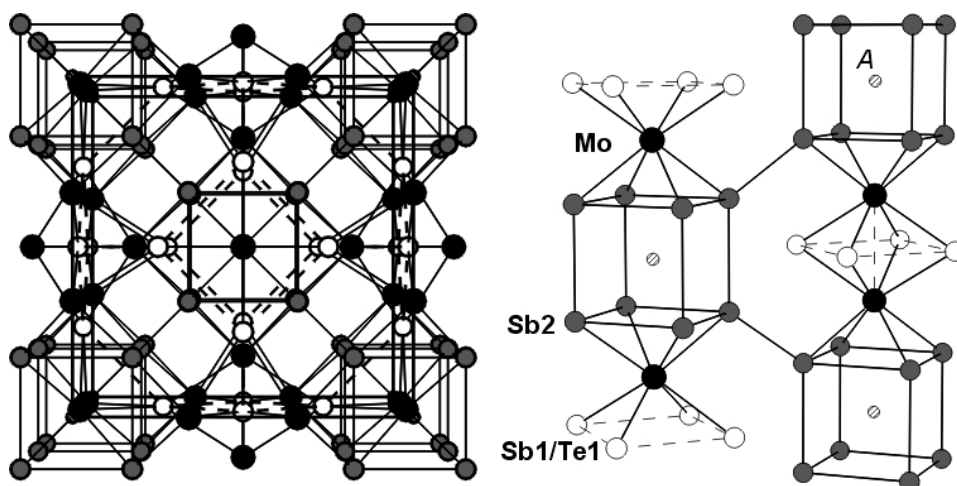


Fig. 3.1 Crystal structure of $A_y\text{Mo}_3\text{Sb}_{7-x}\text{Te}_x$ (left) and its chains (right)

The preference of Te atoms on the Sb1 site is due to Te has higher electronegativity than Sb, which translates as a preference for the site with less anion–anion bonding. Similar scenarios are observed for the S atoms in ZrSiS ¹¹⁶ and CeAsS .¹¹⁷ This deduction was also confirmed via neutron diffraction by Candolfi *et al.* in 2008.¹¹⁸

3.3 Investigation of $\text{Ni}_y\text{Mo}_3\text{Sb}_{7-x}\text{Te}_x$ and $\text{Fe}_{0.05}\text{Mo}_3\text{Sb}_{7-x}\text{Te}_x$

Previous work from our group demonstrated that adding Ni to $\text{Mo}_3\text{Sb}_{7-x}\text{Te}_x$ can improve simultaneously the Seebeck coefficient and the electrical conductivity, but fail to reduce the thermal conductivity as anticipated.¹¹⁹ In order to understand the effect related to adding Ni and varying Sb/Te ratio, a detailed analysis was conducted in this thesis and the results were further compared with those of $\text{Fe}_{0.05}\text{Mo}_3\text{Sb}_{7-x}\text{Te}_x$.

3.3.1 Rietveld refinement

A Rietveld refinement was performed on the sample with the nominal composition $\text{Ni}_{0.10}\text{Mo}_3\text{Sb}_{5.5}\text{Te}_{1.5}$ since it has the maximum Ni composition. The Rietveld refinement results provided further evidence of the absence of (crystalline) side products because the calculated model matches with the experimental observation very well (Fig. 3.2). Due to the high correlation between the occupancy and thermal displacement parameter of Ni atoms, we could not refine both parameters at the same time. In addition, the 20% filling with Ni of the hole corresponds to only $0.20 \times 30 = 6$ electrons, which is not much compared to the 51 electrons of each of the eight surrounding Sb atoms. Because the scattering power is proportional to the square of the electron number of the atom, the Ni occupancy could not be accurately refined. $\text{Ni}_{0.10}\text{Mo}_3\text{Sb}_{5.5}\text{Te}_{1.5}$ has the lattice parameter $a = 9.5626(7)$ Å. The different residual factors are: $R_p = 0.0608$, $wR_p = 0.0741$ and $R_F^2 = 0.0239$. The atomic positions and thermal displacement parameters are listed in Tab. 3.1.

Tab. 3.1 Rietveld refinement results of $\text{Ni}_{0.10}\text{Mo}_3\text{Sb}_{5.5}\text{Te}_{1.5}$.

Atom	site	x	y	z	occupancy	$U_{\text{eq}}/\text{\AA}^2$
Mo	12e	0.3435(4)	0	0	1.0	0.013(1)
Sb1/Te	12d	0.25	0	0.5	0.5/0.5	0.017(1)
Sb2	16f	0.1628(2)	0.1628(2)	0.1628(2)	1.0	0.016(1)
Ni	2a	0	0	0	0.07(1)	0.015

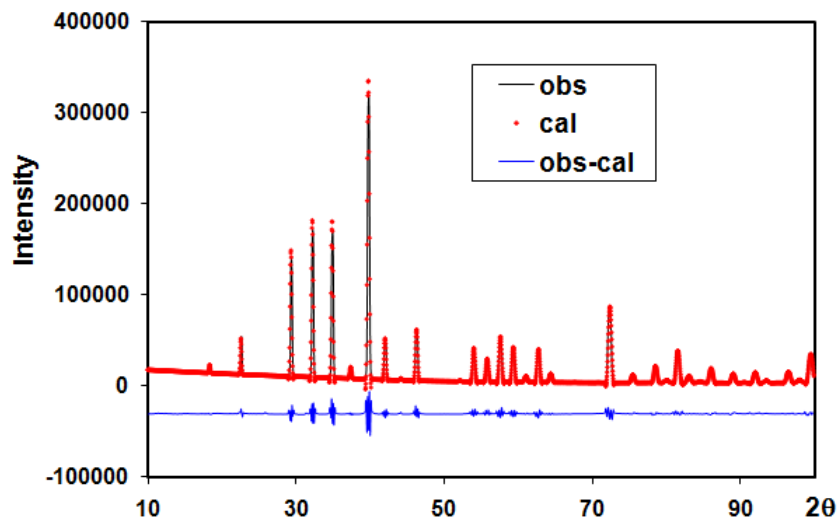


Fig. 3.2 Rietveld refinement of $\text{Ni}_{0.10}\text{Mo}_3\text{Sb}_{5.5}\text{Te}_{1.5}$.

3.3.2 Electronic structure calculations

The LMTO47c program package was utilized for the electronic structure calculations. This package is based on the self-consistent tight-binding first principles LMTO method with the atomic spheres approximation (ASA).^{105, 120} Therein, density functional theory is

employed utilizing the local density approximation (LDA) for the exchange and correlation energies.¹²¹ A recent computation¹²² showed that this method gives virtually the same results for Mo₃Sb₇ as the full potential WIEN2k method.¹²³ Various models were calculated, including Mo₃Sb₇, based on our crystallographic data from the year 2002,⁶² Mo₃Sb_{5.5}Te_{1.5} and Mo₃Sb₅Te₂, based on the Mo₃Sb₇ model, where part of the Sb1 atoms were replaced with the corresponding number of Te atoms. The substitutions required a symmetry reduction to *I4/mmm* in the case of Mo₃Sb₅Te₂ and to *Imm2* in the case of Mo₃Sb_{5.5}Te_{1.5}, leaving the unit cell size unchanged in both cases. Finally, we doubled the unit cell in order to fill only a quarter of the voids, thus modeling *A*_{0.125}Mo₃Sb₅Te₂ with *A* = Fe, Ni, space group *P4/mmm*. The following wavefunctions were used: for Fe and Ni *4s*, *4p*, and *3d*, for Mo *5s*, *5p* and *4d*, and *4f* included via the downfolding technique;¹²⁴ for Sb and Te *5s* and *5p*, and *5d* and *4f* (the last two downfolded). The *k* points of the first Brillouin zones (at least 300, depending on the zone size) were selected via an improved tetrahedron method.¹²⁵

The computed densities of states of Mo₃Sb₇, Mo₃Sb_{5.5}Te_{1.5} and Mo₃Sb₅Te₂ are compared in Figure 3.3. A band gap of 0.6 eV is directly at the Fermi level (*E_F*) for Mo₃Sb₅Te₂ with 55 valence electrons. Ignoring the interactions with interatomic distances longer than 3 Å between Sb1/Te1 and Sb1/Te1, the charges can be assigned as Mo⁵⁺, Sb1³⁻, Sb2²⁻, and Te²⁻, which results in the electron precise formula (Mo⁵⁺)₃(Sb1³⁻)(Sb2²⁻)₄(Te²⁻)₂ with 15 positive and 15 negative charges, thereby showing the possibility of semiconducting properties.

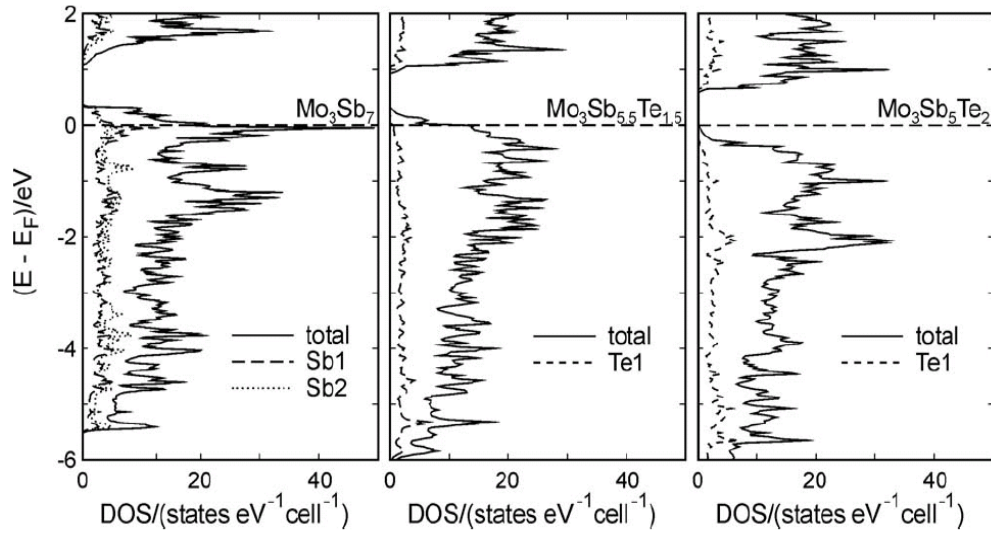


Fig. 3.3 Density of states of Mo_3Sb_7 (left), $\text{Mo}_3\text{Sb}_{5.5}\text{Te}_{1.5}$ (center) and $\text{Mo}_3\text{Sb}_5\text{Te}_2$ (right); the dashed line represents Fermi level.

$\text{Mo}_3\text{Sb}_{5.5}\text{Te}_{1.5}$ has fewer valence-electrons per formula unit, namely 54.5, which can be understood as a *p*-doped semiconductor. This was confirmed experimentally by low temperature Hall measurements. Hole charge carrier concentration of $\text{Mo}_3\text{Sb}_{5.4}\text{Te}_{1.6}$ shows a value of $4 \cdot 10^{21}/\text{cm}^3$ at 300 K,¹¹⁹ which compares well with the $4(2) \cdot 10^{21}/\text{cm}^3$ determined for $\text{Mo}_3\text{Sb}_{5.4}\text{Te}_{1.6}$ by Gascoin *et al.*¹²⁶ The more electron-deficient Mo_3Sb_7 (53 valence-electrons) has too many charge carriers to be a useful thermoelectric, which is reflected by its small Seebeck coefficient, e.g. $25 \mu\text{K}^{-1}$ at 300 K.⁶² However Mo_3Sb_7 is still considered as one of the best *p*-type thermoelectric metals.¹²⁷

Adding different metal atoms (*A*) into the cube will change the electronic structure consequently due to the interactions created between *A* and Sb as well as *A* and Mo. For example, the band gap almost disappears when the hole is completely filled with Mg atoms. This is a consequence of the weak Mg–Mo interaction of 3.3 \AA that significantly lowers the

conduction band of Mo-*d* character.⁶³ However, since we never succeeded in filling more than 20% of the holes, corresponding to the formula $A_{0.10}\text{Mo}_3\text{Sb}_{7-x}\text{Te}_x$, the impact of the hole filling is less significant.

Our particular interest is the effect of the additional small transition metal atoms (Ni, Fe) on the charge carrier concentration and density of states, which in turn strongly influence the thermoelectric properties. As shown in Fig. 3.4, adding Fe leads to a depopulation of the valence band because E_F is lowered into the valence band, while adding Ni does not change the electron count (E_F remains in the band gap). Considering that the materials investigated are *p*-doped because of the ratio of Sb/Te > 5/2, the charge carrier (hole) concentration should increase upon adding Fe into the cubic voids, as more states within the valence band are empty. The 3*d* electrons of Ni are in the valence band and Ni can be regarded as d^{10} , hence Ni^0 , which in turn explains why adding Ni does not change the nominal valence electron concentration. Therefore the Fermi level remains in the band gap when Sb/Te = 5/2. However, the Ni *d* states increase the DOS of the valence band, and thereby the charge carrier concentration when Sb/Te > 5/2. This calculation was confirmed by our Hall data: the charge carrier concentration of $\text{Ni}_{0.06}\text{Mo}_3\text{Sb}_{5.4}\text{Te}_{1.6}$ was determined to be 20% higher ($5 \times 10^{21}/\text{cm}^3$ at 300 K) than that of $\text{Mo}_3\text{Sb}_{5.4}\text{Te}_{1.6}$.¹¹⁹

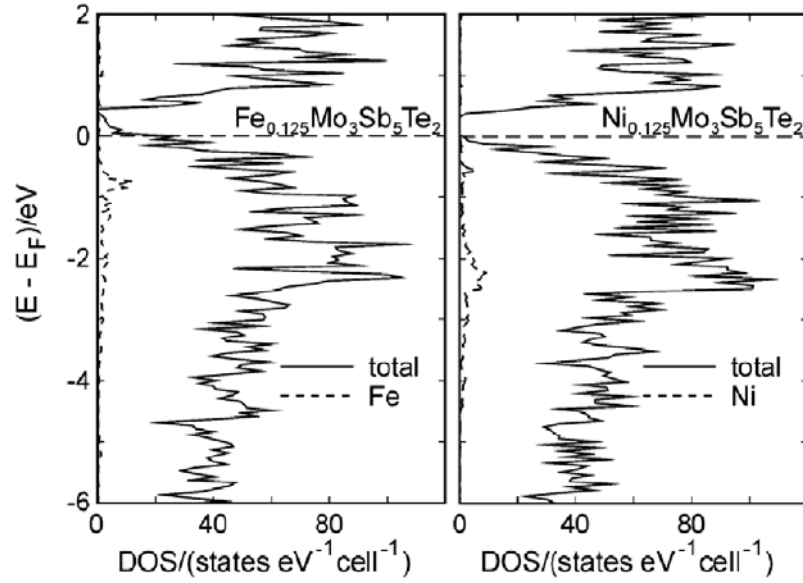


Fig. 3.4 Density of states of $\text{Fe}_{0.125}\text{Mo}_3\text{Sb}_5\text{Te}_2$ (left) and $\text{Ni}_{0.125}\text{Mo}_3\text{Sb}_5\text{Te}_2$ (right).

Moreover, because the $3d$ electrons of both iron and nickel contribute to the valence-band, the DOS around E_F changes its size and slope, which in turn influences the Seebeck coefficient according to the Mott equation (3-1).¹²⁸ Unfortunately the exact impact on the Seebeck coefficient is hard to predict, because the calculations might not have enough accuracy to yield quantifiable results, in particular considering the different, likely statistically disordered filling of the cubic holes with Ni atoms.

$$S \propto \frac{1}{DOS(E_F)} \left(\frac{\partial DOS(E)}{\partial E} \right)_{E=E_F} \quad (3-1)$$

3.3.3 Physical properties

The electrical conductivity curves of $\text{Ni}_y\text{Mo}_3\text{Sb}_{7-x}\text{Te}_x$ series compounds are typical for many thermoelectric materials – semiconductors with high charge carrier concentration. The

electrical conductivity, σ , is of the order of $2 \cdot 10^3 \Omega^{-1} \text{cm}^{-1}$ around 300 K, and decreases smoothly with increasing temperature in all cases studied here (Fig. 3.5). With $\text{Mo}_3\text{Sb}_5\text{Te}_2$ being the electron precise material, the p -type charge carrier concentration increases with decreasing Te content. Because σ is proportional to the charge carrier concentration (as well as to the charge carrier mobility), the samples with 1.5 Te per formula unit have the largest σ values, followed by the samples with 1.6 Te (intermediate) and the sample with 1.7 Te exhibiting the smallest σ values. For example, electrical conductivity of $\text{Ni}_{0.08}\text{Mo}_3\text{Sb}_{5.5}\text{Te}_{1.5}$ decreases from $2300 \Omega^{-1} \text{cm}^{-1}$ at 325 K to $1550 \Omega^{-1} \text{cm}^{-1}$ at 760 K; σ of $\text{Ni}_{0.05}\text{Mo}_3\text{Sb}_{5.3}\text{Te}_{1.7}$ from $1450 \Omega^{-1} \text{cm}^{-1}$ at 325 K to $980 \Omega^{-1} \text{cm}^{-1}$ at 760 K.

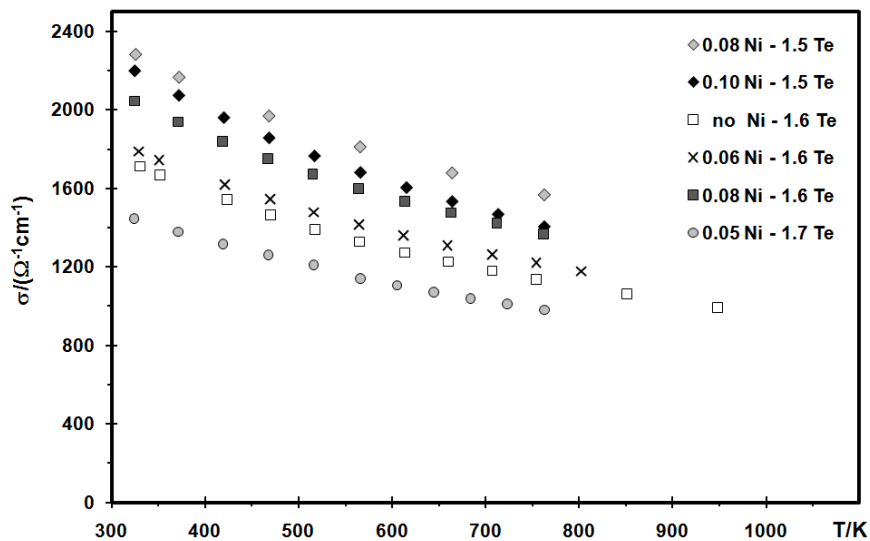


Fig. 3.5 Electrical conductivity of $\text{Ni}_y\text{Mo}_3\text{Sb}_{7-x}\text{Te}_x$.

No clear trend results from varying the Ni concentration. This may be associated with the experimental uncertainty related to the low concentration of Ni in the samples as well as

the similarity of the σ values. We expect σ of $\text{Ni}_y\text{Mo}_3\text{Sb}_{5.4}\text{Te}_{1.6}$ to be slightly higher than σ of $\text{Mo}_3\text{Sb}_{5.4}\text{Te}_{1.6}$, as is the case, because the DOS increases at E_F , the increase being caused by the addition of the $3d$ states of Ni. However, then $\text{Ni}_{0.10}\text{Mo}_3\text{Sb}_{5.5}\text{Te}_{1.5}$ should exhibit higher σ than $\text{Ni}_{0.08}\text{Mo}_3\text{Sb}_{5.5}\text{Te}_{1.5}$, but the opposite trend was observed in our experiments. The corresponding curves for $\text{Fe}_{0.05}\text{Mo}_3\text{Sb}_{7-x}\text{Te}_x$ exhibited similar shapes, with $\sigma(325\text{ K})$ ranging from $1900\ \Omega^{-1}\text{cm}^{-1}$ ($x = 1.5$) to $1090\ \Omega^{-1}\text{cm}^{-1}$ ($x = 1.7$), shown in Fig. 3.6. However, the Fe materials consistently possess lower σ values than the Ni materials of the same Te content x .

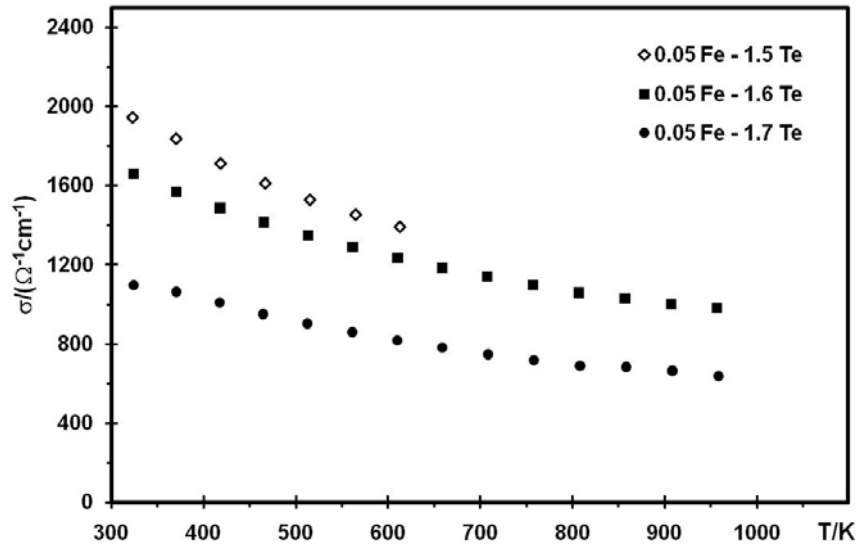


Fig. 3.6 Electrical conductivity of $\text{Fe}_{0.05}\text{Mo}_3\text{Sb}_{7-x}\text{Te}_x$.

The Seebeck coefficient measurements confirmed that the $\text{Ni}_y\text{Mo}_3\text{Sb}_{7-x}\text{Te}_x$ materials are p -type conductors, with Seebeck values, S , between $+49\ \mu\text{VK}^{-1}$ and $+68\ \mu\text{VK}^{-1}$ at 325 K (Fig. 3.7). In each case, S increases linearly with increasing temperature. For the most cases, S follows the trend opposite to σ , with the Te-poor samples exhibiting the smallest S values,

while $\text{Ni}_{0.06}\text{Mo}_3\text{Sb}_{5.4}\text{Te}_{1.6}$ is the notable exception, having slightly larger S values than $\text{Ni}_{0.05}\text{Mo}_3\text{Sb}_{5.3}\text{Te}_{1.7}$. The same general trend was found for the Fe series samples $\text{Fe}_{0.05}\text{Mo}_3\text{Sb}_{7-x}\text{Te}_x$ (Fig. 3.8), with comparable values, e.g. S (325 K) between $+56 \mu\text{VK}^{-1}$ ($x = 1.5$) and $+69 \mu\text{VK}^{-1}$ ($x = 1.7$).

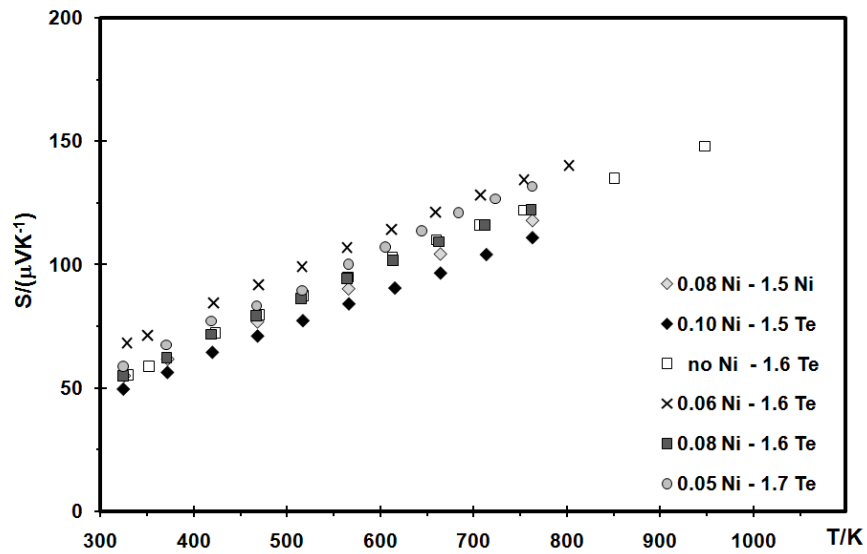


Fig. 3.7 Seebeck coefficient of $\text{Ni}_x\text{Mo}_3\text{Sb}_{7-x}\text{Te}_x$.

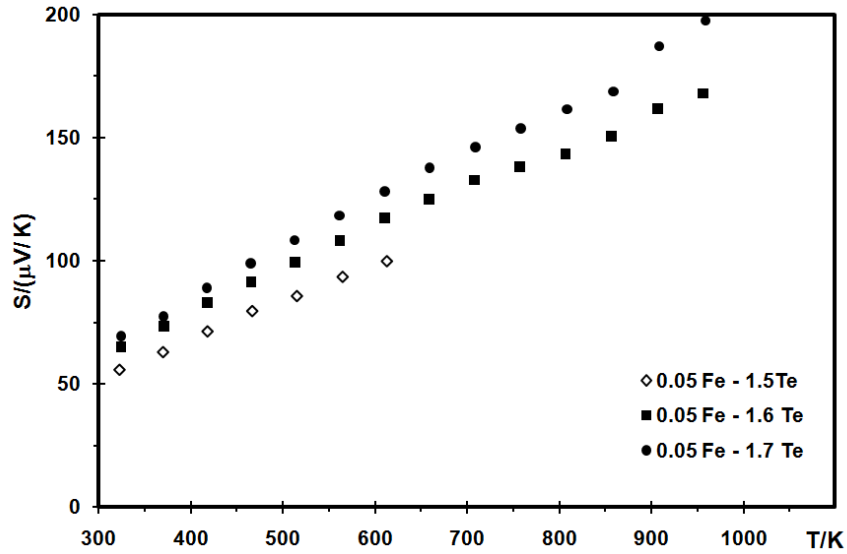


Fig. 3.8 Seebeck coefficient of $\text{Fe}_{0.05}\text{Mo}_3\text{Sb}_{7-x}\text{Te}_x$.

The electrical conductivity values reported here are comparable to or even higher than the values of the other leading high temperature thermoelectric materials. The room temperature σ values of $\text{AgPb}_{18}\text{SbTe}_{20}$ (LAST-18)³⁰ and $\text{Yb}_{14}\text{MnSb}_{11}$ ⁴³ are $1850 \Omega^{-1}\text{cm}^{-1}$ and $450 \Omega^{-1}\text{cm}^{-1}$, respectively. The Seebeck values of our materials, on the other hand, are smaller than the values of *n*-type LAST-18 ($-135 \mu\text{VK}^{-1}$), and comparable with *p*-type $\text{Yb}_{14}\text{MnSb}_{11}$ ($+60 \mu\text{VK}^{-1}$) at 300 K.

The combined impact of Seebeck coefficient and electrical conductivity on the thermoelectric performance is given by the numerator of ZT , the power factor $\text{P.F.} = S^2\sigma T$ (sometimes the power factor is also defined as $S^2\sigma$). The best power factor of the series of $\text{Ni}_y\text{Mo}_3\text{Sb}_{7-x}\text{Te}_x$ is exhibited by $\text{Ni}_{0.06}\text{Mo}_3\text{Sb}_{5.4}\text{Te}_{1.6}$, with a $\text{P.F.}(300 \text{ K}) = 0.23 \text{ Wm}^{-1}\text{K}^{-1}$, reaching $\text{P.F.} = 1.66 \text{ Wm}^{-1}\text{K}^{-1}$ at 750 K (Fig. 3.9). As $S^2\sigma$ increases proportional with the

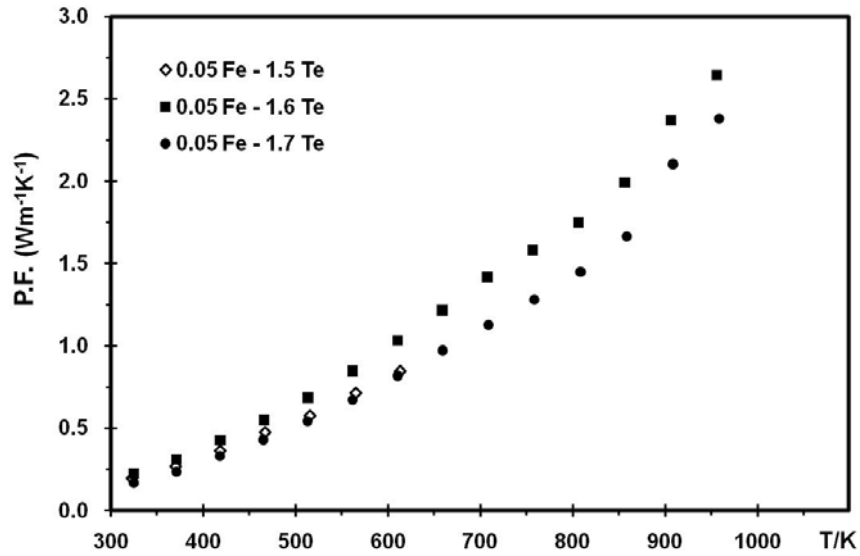


Fig. 3.10 Power factor (P.F.) of $\text{Fe}_{0.05}\text{Mo}_3\text{Sb}_{7-x}\text{Te}_x$.

The P.F. values of $\text{Ni}_y\text{Mo}_3\text{Sb}_{7-x}\text{Te}_x$ (and $\text{Fe}_{0.05}\text{Mo}_3\text{Sb}_{7-x}\text{Te}_x$) are all significantly higher than the values of $\text{Yb}_{14}\text{MnSb}_{11}$, where $\text{P.F.}(300\text{ K}) = 0.05\text{ Wm}^{-1}\text{K}^{-1}$ and $\text{P.F.}(1023\text{ K}) = 0.61\text{ Wm}^{-1}\text{K}^{-1}$ were observed.⁴³ The LAST compounds demonstrate values similar to those of $\text{Ni}_y\text{Mo}_3\text{Sb}_{7-x}\text{Te}_x$, with a maximum for LAST-18 of $\text{P.F.}(700\text{ K}) = 1.96\text{ Wm}^{-1}\text{K}^{-1}$.³⁰

While the large power factor is the main advantage of the $\text{Ni}_y\text{Mo}_3\text{Sb}_{7-x}\text{Te}_x$ compounds, the high total thermal conductivity, κ , is their main disadvantage, with values between $4.5\text{ Wm}^{-1}\text{K}^{-1}$ and $5.6\text{ Wm}^{-1}\text{K}^{-1}$ at 325 K (Fig. 3.11), noting that the corresponding thermal conductivity values of $\text{Fe}_{0.05}\text{Mo}_3\text{Sb}_{7-x}\text{Te}_x$ were intermediate, between the ranges of $5.1\text{ Wm}^{-1}\text{K}^{-1}$ to $5.4\text{ Wm}^{-1}\text{K}^{-1}$ at 325 K and $3.85\text{ Wm}^{-1}\text{K}^{-1}$ to $4.0\text{ Wm}^{-1}\text{K}^{-1}$ at 672 K (Fig. 3.12). Therefore, it can be concluded that the addition of A (Fe, Ni) atoms slightly increases the thermal conductivity instead of decreasing it. The increase of the thermal conductivity likely originates from hole filling resulting in a more dense material.

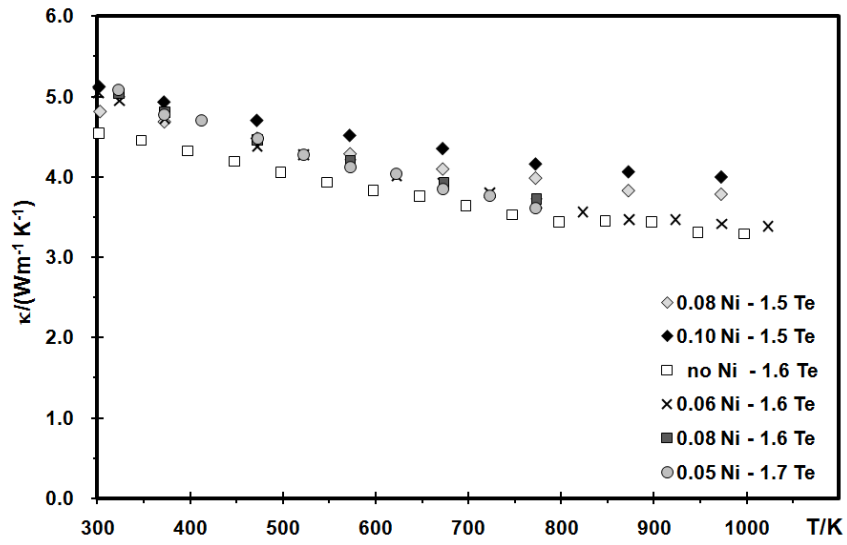


Fig. 3.11 Thermal conductivity of $\text{Ni}_y\text{Mo}_3\text{Sb}_{7-x}\text{Te}_x$.

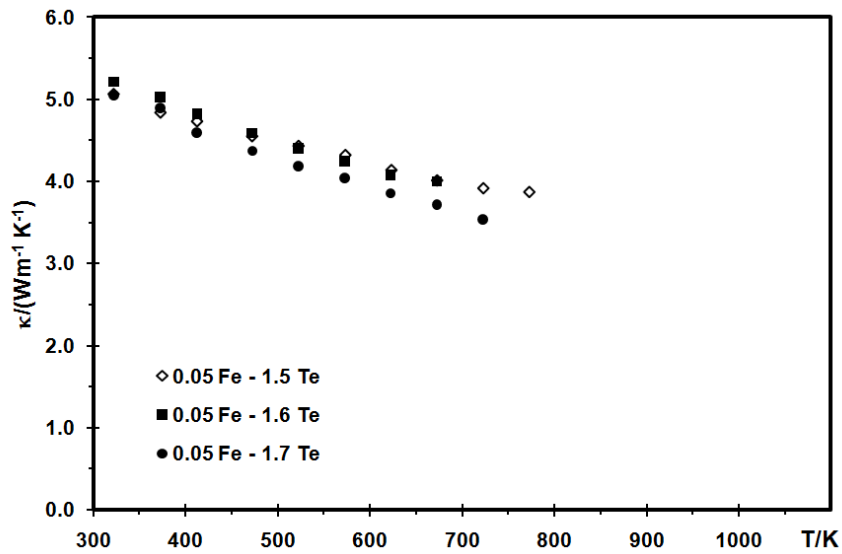


Fig. 3.12 Thermal conductivity of $\text{Fe}_{0.05}\text{Mo}_3\text{Sb}_{7-x}\text{Te}_x$.

Because κ was measured at slightly different temperatures than S and σ , we used the linear fits for the product $S^2\sigma$ together with the measured κ values to calculate the ZT values

as a function of the temperature. κ gradually decreases with the increasing temperature in each case, while the power factor increases continuously, the ZT curves show drastic increases at elevated temperatures. Within the series $\text{Ni}_y\text{Mo}_3\text{Sb}_{7-x}\text{Te}_x$ (Fig. 3.13), the samples with $x = 1.6$ exhibit the largest ZT values, and the ones with $x = 1.5$ display the smallest values. While the samples with $0 \leq y \leq 0.06$ in general have comparable ZT values, $\text{Ni}_{0.06}\text{Mo}_3\text{Sb}_{5.4}\text{Te}_{1.6}$ is at the top of the series, with $ZT = 0.93$ at 1023 K (assuming that $S^2\sigma$ continues to increase linearly beyond 800 K, as observed in case of $\text{Ni}_{0.05}\text{Mo}_3\text{Sb}_{5.4}\text{Te}_{1.6}$). At that temperature, ZT of $\text{Yb}_{14}\text{MnSb}_{11}$ is slightly below 0.9, and the ZT of LAST-18 is not reported. LAST-18 reaches $ZT = 2.2$ at 800 K, where $\text{Ni}_{0.06}\text{Mo}_3\text{Sb}_{5.4}\text{Te}_{1.6}$ exhibits $ZT = 0.51$, and $\text{Yb}_{14}\text{MnSb}_{11}$ $ZT = 0.48$. The highest ZT value of the series $\text{Fe}_{0.05}\text{Mo}_3\text{Sb}_{7-x}\text{Te}_x$ is observed for $\text{Fe}_{0.05}\text{Mo}_3\text{Sb}_{5.4}\text{Te}_{1.6}$ with $ZT = 0.31$ at 672 K, (Fig. 3.14), where the top line sample $\text{Ni}_{0.06}\text{Mo}_3\text{Sb}_{5.4}\text{Te}_{1.6}$ shows a ZT of 0.34 at that temperature.

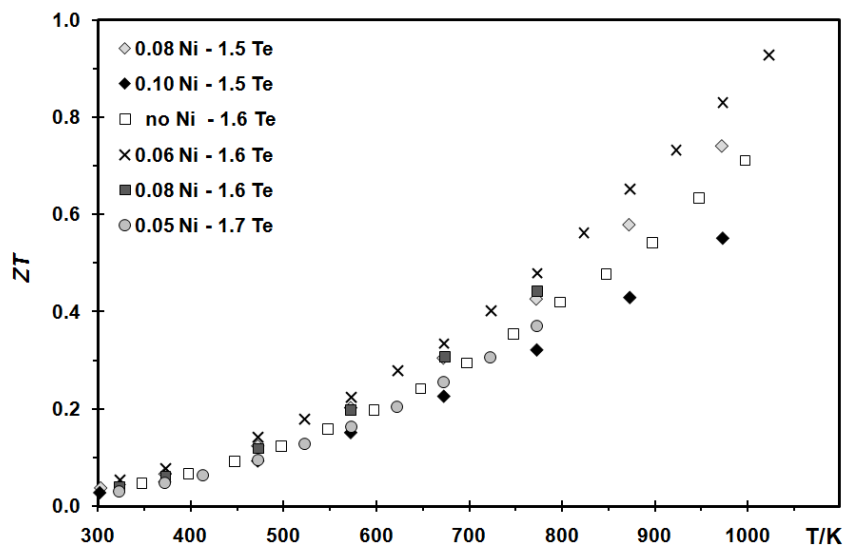


Fig. 3.13 Figure of merit (ZT) of $\text{Ni}_y\text{Mo}_3\text{Sb}_{7-x}\text{Te}_x$.

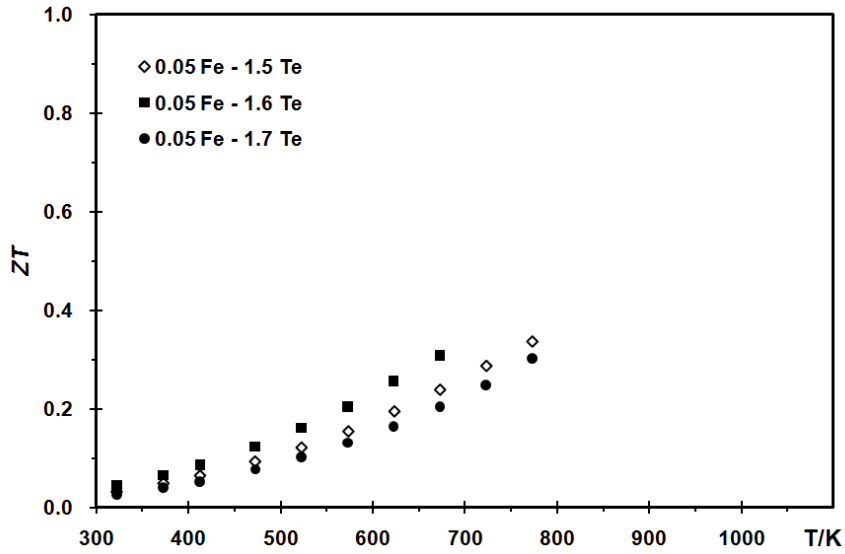


Fig. 3.14 Figure of merit (ZT) of $\text{Fe}_{0.05}\text{Mo}_3\text{Sb}_{7-x}\text{Te}_x$.

The materials discussed above are in general bestowed with large power factor values, leading to competitive ZT values at high temperature despite relatively high thermal conductivity. The addition of Ni and Fe does not decrease the thermal conductivity, but increases the power factor, thus an enhancement of thermoelectric properties can still be achieved at the right concentration. The best ratio of Sb/Te was deduced to be 5.4/1.6 for both $\text{Ni}_y\text{Mo}_3\text{Sb}_{7-x}\text{Te}_x$ and $\text{Fe}_{0.05}\text{Mo}_3\text{Sb}_{7-x}\text{Te}_x$. Therefore, we decided to conduct further research focused on the effect of different transition metal atoms on thermoelectric properties with the optimized $x = 1.6$.¹¹⁴

3.4 Investigation of $A_{0.05}\text{Mo}_3\text{Sb}_{5.4}\text{Te}_{1.6}$ ($A = \text{Mn, Fe, Co, Ni}$)

The sample preparation and the general crystal structure information have been described in section 3.1 and 3.2. The scanning electron microscope (SEM), high resolution

transmission electron microscope (HRTEM), transport property measurements and thermal analysis will be discussed below.

3.4.1 Electron Microscopy

A hot-pressed pellet of a nominal composition $\text{Ni}_{0.05}\text{Mo}_3\text{Sb}_{5.4}\text{Te}_{1.6}$ was analyzed using the LEO 1530 scanning electron microscope (SEM) with integrated EDAX Pegasus 1200, with an acceleration voltage of 20 kV. The SEM map screens of the composing elements of $\text{Ni}_{0.05}\text{Mo}_3\text{Sb}_{5.4}\text{Te}_{1.6}$ are shown in Fig. 3.15. The distribution of Ni, Mo, Sb and Te appeared to be quite homogeneous throughout the sample. A part of this pellet was sent to McMaster University for high resolution transmission electron microscope (HRTEM) analysis on the Cs corrected FEI Titan TEM with a 300 keV acceleration voltage. TEM samples were prepared by low angle wedge tripod polishing. The thin tip of the wedge was ion milled at liquid nitrogen temperature to electron transparency.

Bright field TEM images show large single crystal regions in the sample (Fig. 3.16). Bend contours are apparent in thin regions where the crystal lattice is strained. The residual strain in the lattice is likely due to the mechanical thinning process. The SAED pattern is in good agreement with that calculated¹²⁹ for the $\langle 102 \rangle$ zone axis orientation. The CBED pattern imaged down the same $\langle 102 \rangle$ zone axis displays $m\bar{3}m$ symmetry, consistent with the proposed space group $Im\bar{3}m$. Higher order Laue zones and Kikuchi lines are also visible in the CBED pattern and are in good agreement with the calculations. Finally, HRTEM phase contrast images reveal individual atomic columns in the lattice oriented down the $\langle 102 \rangle$ and $\langle 101 \rangle$ zone axis, indicating the high crystallinity of $\text{Ni}_{0.05}\text{Mo}_3\text{Sb}_{5.4}\text{Te}_{1.6}$. The somewhat

mottled appearance in Fig. 3.16(g) is likely due to the presence of a thin amorphous layer on the surface of the sample. No nanostructured domains were detected.

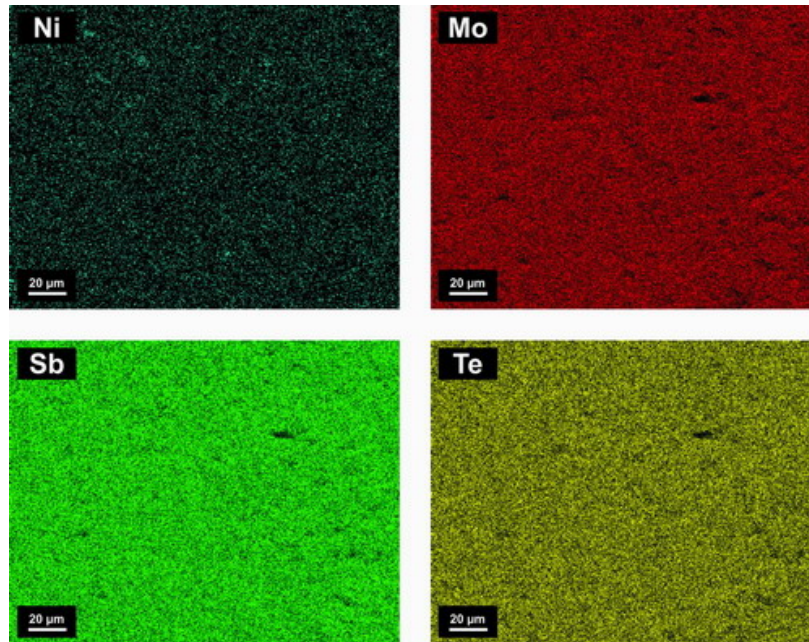


Fig. 3.15 SEM map screens of different elements of $\text{Ni}_{0.05}\text{Mo}_3\text{Sb}_{5.4}\text{Te}_{1.6}$.

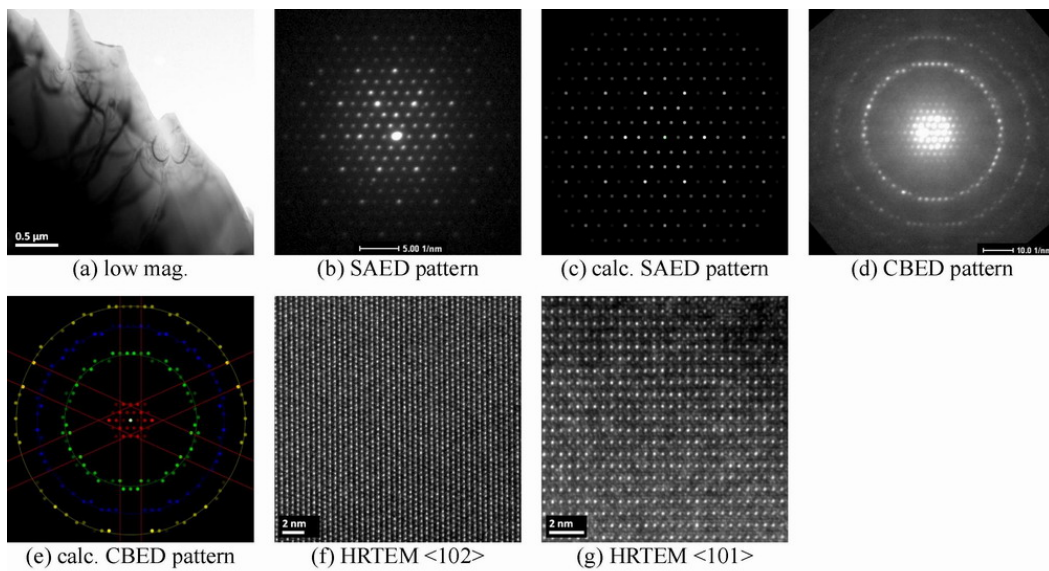


Fig. 3.16 TEM images of $\text{Ni}_{0.05}\text{Mo}_3\text{Sb}_{5.4}\text{Te}_{1.6}$.

3.4.2 Physical properties

All of our samples show reasonably high electrical conductivity values, above $1000 \Omega^{-1}\text{cm}^{-1}$ at 300 K. In each case, the electrical conductivity (σ) decreases with increasing temperature (Fig. 3.17), since the charge carrier concentration is basically independent of the temperature in degenerate semiconductors.¹¹⁹ $\text{Ni}_{0.05}\text{Mo}_3\text{Sb}_{5.4}\text{Te}_{1.6}$ demonstrates the highest σ ($1800 \Omega^{-1}\text{cm}^{-1}$ at 320 K), and $\text{Co}_{0.05}\text{Mo}_3\text{Sb}_{5.4}\text{Te}_{1.6}$ the lowest with $1500 \Omega^{-1}\text{cm}^{-1}$ at 320 K. The sample without a $3d$ element (called "no A") exhibits the second highest σ ($1740 \Omega^{-1}\text{cm}^{-1}$ at 320 K). $\text{Mn}_{0.05}\text{Mo}_3\text{Sb}_{5.4}\text{Te}_{1.6}$ and $\text{Fe}_{0.05}\text{Mo}_3\text{Sb}_{5.4}\text{Te}_{1.6}$ have virtually identical electrical conductivity values of $1650 \Omega^{-1}\text{cm}^{-1}$ at 320 K. With the increasing temperature, σ of $\text{Fe}_{0.05}\text{Mo}_3\text{Sb}_{5.4}\text{Te}_{1.6}$ decreases more slowly.

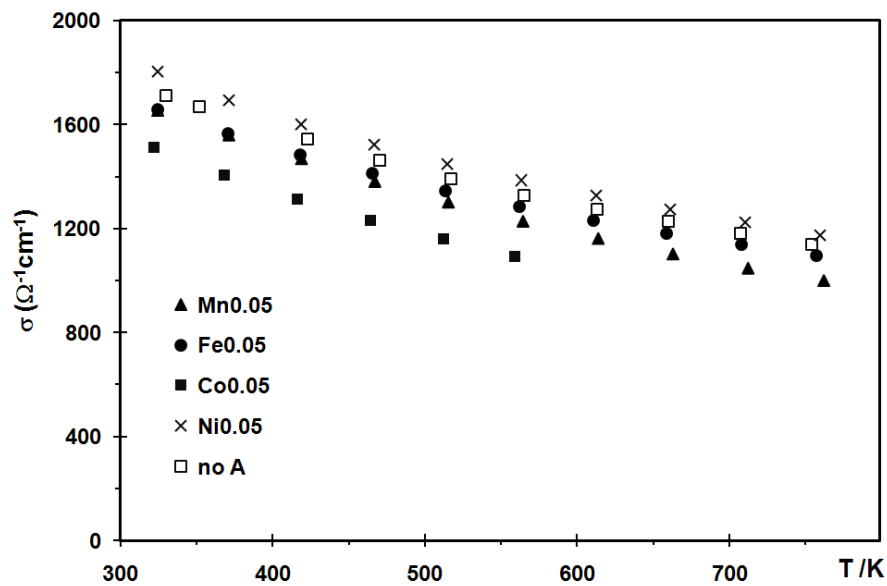


Fig. 3.17 Electrical conductivity of $A_{0.05}\text{Mo}_3\text{Sb}_{5.4}\text{Te}_{1.6}$ ($A = \text{Mn}, \text{Fe}, \text{Co}, \text{Ni}$) and $\text{Mo}_3\text{Sb}_{5.4}\text{Te}_{1.6}$.

All the samples have Seebeck values (S) between $55 \mu\text{VK}^{-1}$ and $65 \mu\text{VK}^{-1}$ around 320 K (Fig. 3.18). S increases in all cases with increasing temperature, typical for the samples with the constant charge carrier concentration, reaching a maximum of $170 \mu\text{VK}^{-1}$ at 950 K in case of $\text{Fe}_{0.05}\text{Mo}_3\text{Sb}_{5.4}\text{Te}_{1.6}$. The samples with the highest electrical conductivity, $\text{Ni}_{0.05}\text{Mo}_3\text{Sb}_{5.4}\text{Te}_{1.6}$ and $\text{Mo}_3\text{Sb}_{5.4}\text{Te}_{1.6}$, have the lowest Seebeck coefficient values. $\text{Fe}_{0.05}\text{Mo}_3\text{Sb}_{5.4}\text{Te}_{1.6}$ has the highest Seebeck coefficient.

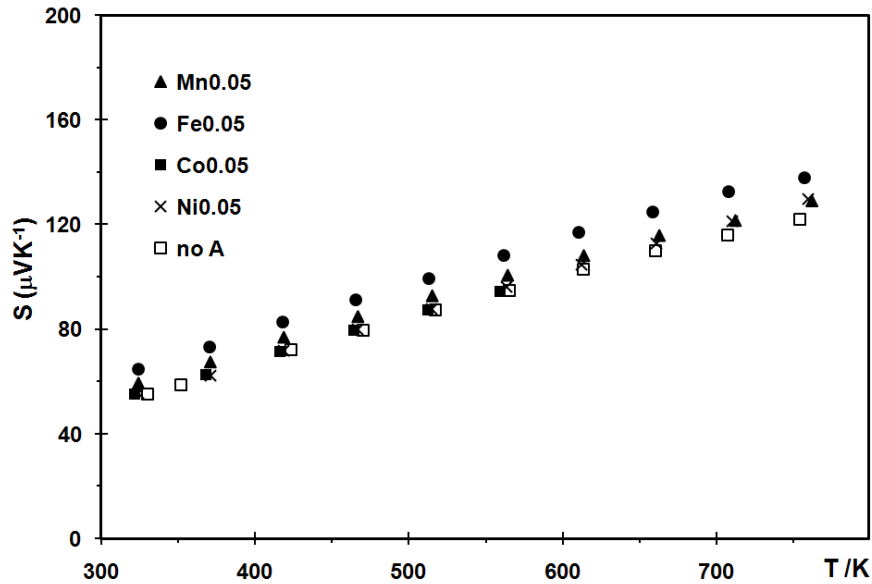


Fig. 3.18 Seebeck coefficient of $A_{0.05}\text{Mo}_3\text{Sb}_{5.4}\text{Te}_{1.6}$ ($A = \text{Mn}, \text{Fe}, \text{Co}, \text{Ni}$) and $\text{Mo}_3\text{Sb}_{5.4}\text{Te}_{1.6}$.

Because of its highest Seebeck coefficient and intermediate electrical conductivity, $\text{Fe}_{0.05}\text{Mo}_3\text{Sb}_{5.4}\text{Te}_{1.6}$ exhibits the highest power factor in the whole temperature range measured (Fig. 3.19), with $\text{P.F.}(324 \text{ K}) = 0.23 \text{ Wm}^{-1}\text{K}^{-1}$ and $\text{P.F.}(956 \text{ K}) = 2.64 \text{ Wm}^{-1}\text{K}^{-1}$. $\text{Ni}_{0.05}\text{Mo}_3\text{Sb}_{5.4}\text{Te}_{1.6}$, $\text{Mn}_{0.05}\text{Mo}_3\text{Sb}_{5.4}\text{Te}_{1.6}$ and $\text{Mo}_3\text{Sb}_{5.4}\text{Te}_{1.6}$ have comparable power factor values below 570 K. With rising temperature, P.F. of $\text{Ni}_{0.05}\text{Mo}_3\text{Sb}_{5.4}\text{Te}_{1.6}$ increases more

rapidly. For example, $\text{Ni}_{0.05}\text{Mo}_3\text{Sb}_{5.4}\text{Te}_{1.6}$ has a P.F.(760 K) = $1.51 \text{ Wm}^{-1}\text{K}^{-1}$, $\text{Mn}_{0.05}\text{Mo}_3\text{Sb}_{5.4}\text{Te}_{1.6}$ a P.F.(762 K) = $1.27 \text{ Wm}^{-1}\text{K}^{-1}$ and $\text{Mo}_3\text{Sb}_{5.4}\text{Te}_{1.6}$ a P.F.(754 K) = $1.28 \text{ Wcm}^{-1}\text{K}^{-1}$. $\text{Co}_{0.05}\text{Mo}_3\text{Sb}_{5.4}\text{Te}_{1.6}$ has the lowest power factor within this series of samples, mostly due to its lowest electrical conductivity.

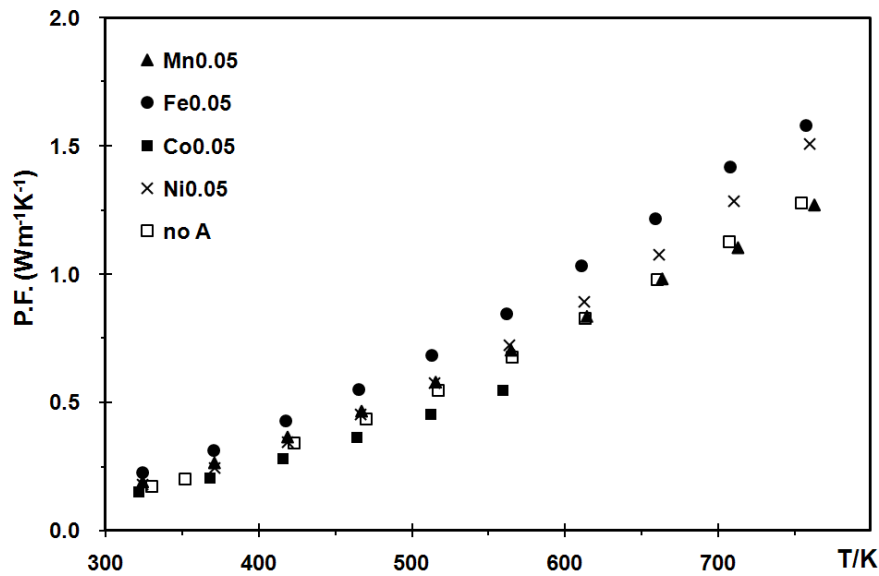


Fig. 3.19 Power factor (P.F.) of $A_{0.05}\text{Mo}_3\text{Sb}_{5.4}\text{Te}_{1.6}$ ($A = \text{Mn, Fe, Co, Ni}$) and $\text{Mo}_3\text{Sb}_{5.4}\text{Te}_{1.6}$.

All of these quaternary antimonide-telluride $A_{0.05}\text{Mo}_3\text{Sb}_{5.4}\text{Te}_{1.6}$ ($A = \text{Mn, Co, Fe, Ni}$) have higher thermal conductivity values than $\text{Mo}_3\text{Sb}_{5.4}\text{Te}_{1.6}$ (Fig. 3.20), with values between $5.2 \text{ Wm}^{-1}\text{K}^{-1}$ ($\text{Fe}_{0.05}\text{Mo}_3\text{Sb}_{5.4}\text{Te}_{1.6}$) and $5.6 \text{ Wm}^{-1}\text{K}^{-1}$ ($\text{Co}_{0.05}\text{Mo}_3\text{Sb}_{5.4}\text{Te}_{1.6}$) at 320 K and $4.0 \text{ Wm}^{-1}\text{K}^{-1}$ ($\text{Fe}_{0.05}\text{Mo}_3\text{Sb}_{5.4}\text{Te}_{1.6}$) to $4.3 \text{ Wm}^{-1}\text{K}^{-1}$ ($\text{Co}_{0.05}\text{Mo}_3\text{Sb}_{5.4}\text{Te}_{1.6}$) at 670 K. The thermal conductivity, being the sum of the lattice contribution (κ_l) and the contribution from the charge carriers (κ_e), is generally decreasing with increasing temperature, as κ_l is the major contribution and it decreases because of the increasing lattice.

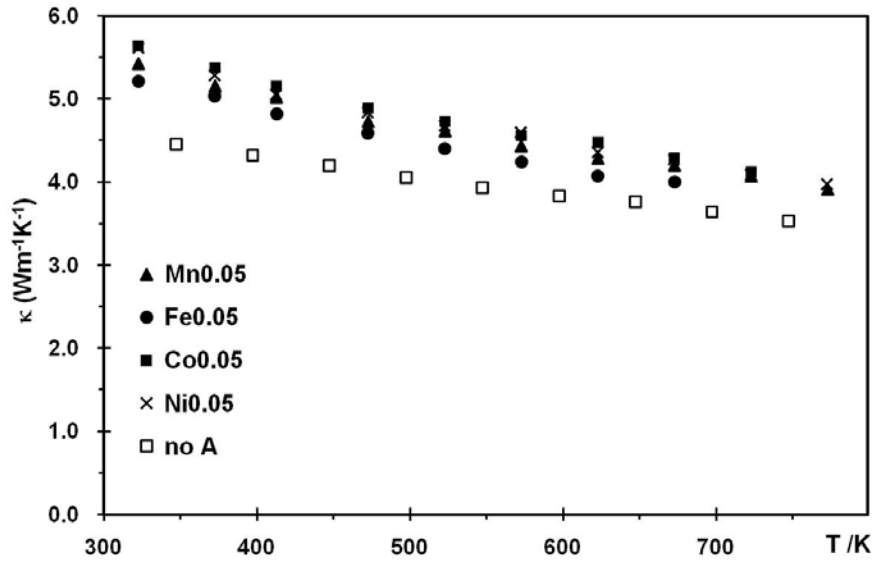


Fig. 3.20 Thermal conductivity of $A_{0.05}\text{Mo}_3\text{Sb}_{5.4}\text{Te}_{1.6}$ ($A = \text{Mn}, \text{Fe}, \text{Co}, \text{Ni}$) and $\text{Mo}_3\text{Sb}_{5.4}\text{Te}_{1.6}$.

Linear fits of the power factor ($S^2\sigma$) combined with the measured thermal conductivity (κ) were used to determine ZT . The uncertainty of the ZT values is estimated to be 5% - 7%. The calculated ZT curves increase rapidly with increasing temperature (Fig. 3.21) because of the simultaneous increase of P.F. and temperature, while decrease of κ . $\text{Fe}_{0.05}\text{Mo}_3\text{Sb}_{5.4}\text{Te}_{1.6}$ presents the largest ZT value here, namely 0.31 at 673 K, which may be extrapolated to reach $ZT = 0.85$ at 1023 K. Both $\text{Fe}_{0.05}\text{Mo}_3\text{Sb}_{5.4}\text{Te}_{1.6}$ and $\text{Yb}_{14}\text{MnSb}_{11}$ ⁴³ reach ZT around 0.8 at 1000 K. $\text{Co}_{0.05}\text{Mo}_3\text{Sb}_{5.4}\text{Te}_{1.6}$ has the lowest ZT , and $\text{Ni}_{0.05}\text{Mo}_3\text{Sb}_{5.4}\text{Te}_{1.6}$, $\text{Mo}_3\text{Sb}_{5.4}\text{Te}_{1.6}$ and $\text{Mn}_{0.05}\text{Mo}_3\text{Sb}_{5.4}\text{Te}_{1.6}$ exhibit very comparable ZT values varying from 0.03 at 322 K to 0.39 at 772 K within the whole range.

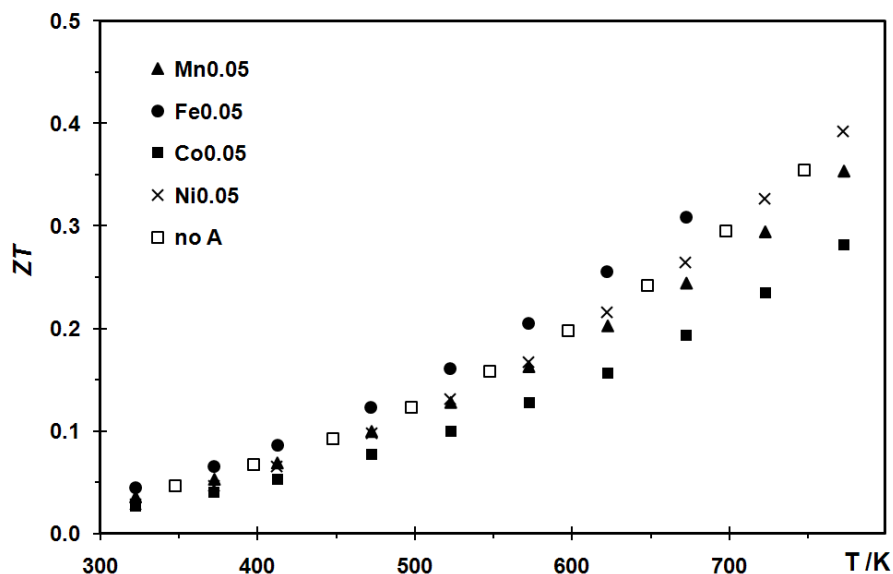


Fig. 3.21 Figure of merit ZT of $A_{0.05}\text{Mo}_3\text{Sb}_{5.4}\text{Te}_{1.6}$ ($A = \text{Mn, Fe, Co, Ni}$) and $\text{Mo}_3\text{Sb}_{5.4}\text{Te}_{1.6}$.

3.4.3 Thermal analysis

Differential scanning calorimetry (DSC) was used to investigate the thermal stability of Mo_3Sb_7 and $\text{Ni}_{0.05}\text{Mo}_3\text{Sb}_{5.4}\text{Te}_{1.6}$. The calorimetry experiment was performed between 300 K and 1473 K with the computer controlled NETZSCH STA 409PC Luxx at a heating rate of 10 K/min. The sample was sealed in a small silica ampoule under vacuum and placed into a flowing argon atmosphere for the measurement, as described previously.¹³⁰ DSC measurements for $\text{Ni}_{0.05}\text{Mo}_3\text{Sb}_{5.4}\text{Te}_{1.6}$ and Mo_3Sb_7 were carried out at the University of Waterloo. The downtrend of the $\text{Ni}_{0.05}\text{Mo}_3\text{Sb}_{5.4}\text{Te}_{1.6}$ curve below 1100 K is caused by an overcorrection of the baseline (Fig. 3.22). In case of Mo_3Sb_7 , the decomposition into the elements of Mo and Sb occurs at 1263 K, and the decomposition of $\text{Ni}_{0.05}\text{Mo}_3\text{Sb}_{5.4}\text{Te}_{1.6}$ peak at 1326 K. Both of these two temperatures are much higher than the earlier reported

decomposition temperature of Mo_3Sb_7 at 1073 K.¹³¹ The obtained Powder X-ray pattern after these experiments revealed the existence of Mo, Sb, $\text{Ni}_x\text{Mo}_3(\text{Sb},\text{Te})_7$ and MoTe_2 . Apparently $\text{Ni}_{0.05}\text{Mo}_3\text{Sb}_{5.4}\text{Te}_{1.6}$ can endure higher temperature than Mo_3Sb_7 , likely as a consequence of the additional filled bonding states because of the larger valence electron concentration.¹²²

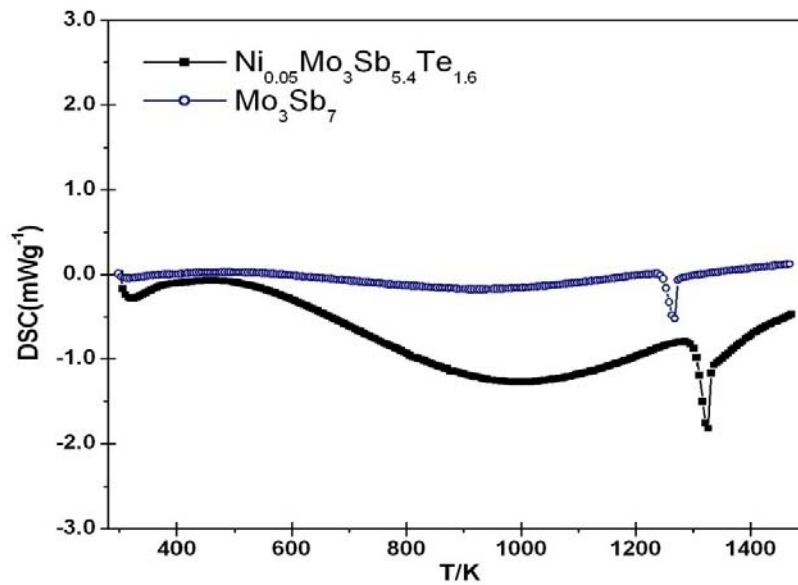


Fig. 3.22 DSC curves of $\text{Ni}_{0.05}\text{Mo}_3\text{Sb}_{5.4}\text{Te}_{1.6}$ and Mo_3Sb_7 .

Based on the results discussed above, an enhancement of the thermoelectric ZT value compared to $\text{Mo}_3\text{Sb}_{5.4}\text{Te}_{1.6}$, was achieved upon addition of Fe and Ni atoms. The best compound with 0.05 A , $\text{Fe}_{0.05}\text{Mo}_3\text{Sb}_{5.4}\text{Te}_{1.6}$, attains $ZT = 0.31$ at 673 K. This value is higher than that of $\text{Ni}_{0.05}\text{Mo}_3\text{Sb}_{5.4}\text{Te}_{1.6}$ ($ZT = 0.27$ at 673 K), but lower than the value of $\text{Ni}_{0.06}\text{Mo}_3\text{Sb}_{5.4}\text{Te}_{1.6}$ ($ZT = 0.34$ at 673 K).¹¹⁵

Compared with the conventional p -type bulk silicon-germanium solid solution (SiGe)¹³², both $\text{Yb}_{14}\text{MnSb}_{11}$ ⁴³ and $\text{Ni}_{0.06}\text{Mo}_3\text{Sb}_{5.4}\text{Te}_{1.6}$ ¹¹⁵ exhibit the much larger ZT values. $\text{Ni}_{0.06}\text{Mo}_3\text{Sb}_{5.4}\text{Te}_{1.6}$ even demonstrates the slightly higher ZT than the value of $\text{Yb}_{14}\text{MnSb}_{11}$

up to 1000 K (Fig. 3.23). Therefore, we conclude $\text{Ni}_{0.06}\text{Mo}_3\text{Sb}_{5.4}\text{Te}_{1.6}$ is a promising *p*-type thermoelectric material for high temperature application.

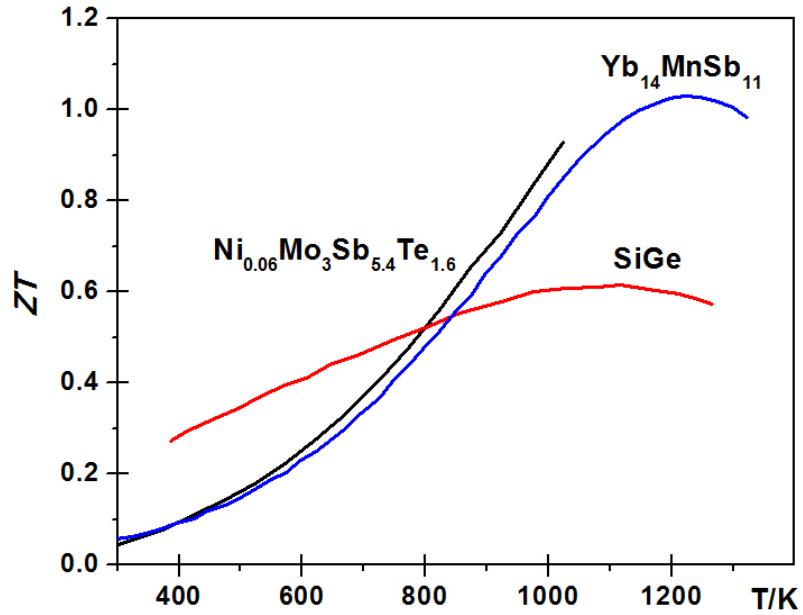


Fig. 3.23 Comparison of ZT values of three *p*-type thermoelectric materials.

4 Thermoelectric properties of Re_3As_7 series samples

Re_3As_7 is another member of Ir_3Ge_7 family, which is isostructural with Mo_3Sb_7 . Previous work in our group confirmed that $\text{Re}_3\text{Ge}_x\text{As}_{7-x}$ presents a good $ZT = 0.36$ at 648 K.⁶⁴ My research target was focused on further improvement of thermoelectric properties by partial substitution on cation and anion sites, such as Si/As, Sn/As, Pb/As exchange¹³³ and Mo/Re exchange. Adding transition metal atoms, e.g. Co, Ni, into the empty cubic center was investigated as well and described in this thesis.

4.1 Sample synthesis

The materials were synthesized from the mixtures of the pure elements: rhenium (powder, -325 mesh, 99.99%), molybdenum (powder, -100 mesh, 99.95%), arsenic (powder, -20 mesh, 99%), silicon (powder, -100 mesh, 99.9%), germanium (powder, -100 mesh, 99.999%), tin (powder, -325 mesh, 99.8%), lead (powder, -200 mesh 99.9%), nickel (powder, -200 mesh, 99.9%) were purchased from Alfa Aesar; cobalt (powder, -100 mesh, 99.9%) was acquired from Sigma Aldrich. Since trace amounts of As_2O_3 were found in the purchased arsenic, the arsenic powder was purified by soaking in 2M NaOH solution for a few minutes, followed by filtration and drying under vacuum before using. The mixtures were loaded into fused silica ampoules in an argon-filled glove box. The silica ampoules were then evacuated, sealed and put into a programmable box furnace. Phase pure compounds were obtained after heating the element mixtures at 973 K for 7 to 10 days.

Attempts at growing single crystals of $\text{Re}_3\text{Sn}_x\text{As}_{7-x}$ were conducted by the Sn flux method and chemical vapor transport with iodine as a medium. However, no good single

crystal was obtained. In the Sn flux method, binary tin arsenides always formed. Although the excess Sn from the flux could be dissolved in 2M hydrochloric acid, it was very difficult to exclusively select the $\text{Re}_3\text{Sn}_x\text{As}_{7-x}$ single crystals from the crystal mixtures of tin arsenide and $\text{Re}_3\text{Sn}_x\text{As}_{7-x}$. In addition, the single crystal quality was not good enough to provide a reliable crystal structure solution. Different flux media (Pb and molten salts) were applied in an attempt to grow Re_3As_7 single crystals (Tab. 4.1). None of these were successful at producing good single crystals of $\text{Re}_3\text{Sn}_x\text{As}_{7-x}$, therefore Rietveld refinement was implemented for structure determination.

Tab. 4.1 Reaction list for preparation single crystals of $\text{Re}_3\text{Sn}_x\text{As}_{7-x}$.

Starting materials	Product	Method and agent applied
$3\text{Re} + 7\text{As} + 3\text{Sn}$	powder mixture of $\text{Re}_3\text{Sn}_x\text{As}_{7-x}$ and tin arsenide	Sn flux HCl washed
$3\text{Re} + 7\text{As} + 10\text{Sn}$	plate crystal mixture of tin arsenide, $\text{Re}_3\text{Sn}_x\text{As}_{7-x}$ and Re	Sn flux HCl eroded
$3\text{Re} + 7\text{As} + 10\text{Pb}$	powder mixture of PbCl_2 and Re_3As_7	Pb flux hot HCl eroded
$3\text{Re} + 7\text{As} + 10(\text{KCl}/\text{KI})$	powder of Re_3As_7	molten salt water washed
$3\text{Re} + 7\text{As} + \text{trace SnCl}_2$	powder of Re_3As_7	vapor transport
$3\text{Re} + 7\text{As} + \text{trace I}_2$	powder of $\text{Re}_3\text{As}_7 + \text{Re}$	vapor transport

4.2 Crystal structure

Re_3As_7 crystallizes in space group $Im\bar{3}m$ (Ir_3Ge_7 type), isostructural with Mo_3Sb_7 , as shown in Fig 4.1. Two symmetry independent As sites, As1 (12*d*) and As2 (16*f*), exist in the structure. The As2 cubes are linked via short As2–As2 bonds (2.53 Å) to form infinite chains that interpenetrate each other at the cubes. The cubes could also be filled with some transition metals atoms, similar with the case of $A_y\text{Mo}_3\text{Sb}_{7-x}\text{Te}_x$.

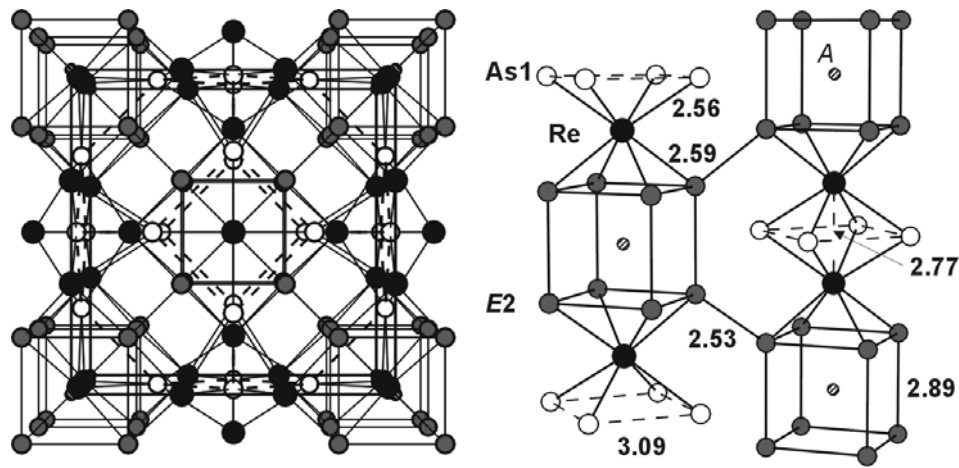


Fig. 4.1 Crystal structure of Re_3As_7 . *E2* presents As2, where can be partially occupied by Si, Ge, Sn and Pb.

4.3 Rietveld refinements

4.3.1 Rietveld refinements on $\text{Re}_3\text{Sn}_x\text{As}_{7-x}$

Rietveld refinements were performed on the $\text{Re}_3\text{Sn}_x\text{As}_{7-x}$ series. No extra peak from any secondary phase is observed in the case of $\text{Re}_3\text{Sn}_{0.1}\text{As}_{6.9}$ (Fig. 4.2).

In our investigations, we compared three models: the first one with Sn only occupying 12*d* sites (As1), the second one with Sn only sitting on 16*f* sites (As2), and the

third one with Sn distributed on both sites. The residual factors (R_p , wR_p , R_F^2) and Sn occupancies for the third model are listed in Tab. 4.2.

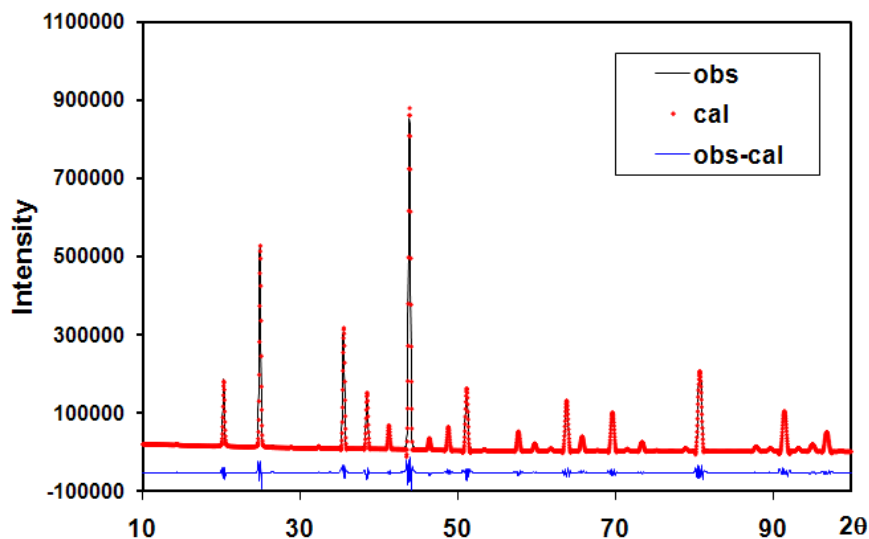


Fig. 4.2 Rietveld refinement on $\text{Re}_3\text{Sn}_{0.1}\text{As}_{6.9}$.

We found a direct relation between site preference and the amount of Sn present in the sample. In the case of $x = 0.1$, the refinement performed on both sites generated a negative occupancy on $16f$ site. The reasonable refinement results were obtained after the occupancy of $16f$ site was fixed as 0, which revealed that the $12d$ site is preferred. It may be due to the longer interatomic distances of between As1 atoms, noting that Sn is larger than As ($r_{(\text{Sn})} = 1.42 \text{ \AA}$; $r_{(\text{As})} = 1.21 \text{ \AA}$).¹³⁴ When more Sn atoms were added, as in the case of $x = 0.3$, Sn starts to occupy the $16f$ site. This is a consequence of Sn having the smaller electronegativity than As. The less electronegative atoms are more likely to occur on sites with stronger anion-anion interactions,^{64, 135} and the As2–As2 bonds exhibit the shortest distances (2.53 \AA) within the crystal structure. In the refined formula $\text{Re}_3\text{Sn}_{1.13(7)}\text{As}_{5.87}$, the $16f$ site shows a larger preference for Sn occupancy at the high Sn content.

Tab. 4.2 Residual factors and refined Sn occupancies for both sites (12*d* and 16*f*).

Nominal composition	Refinement composition	Residual factors and Sn Occupancy	
			Refined values
Re₃Sn_{0.1}As_{6.9}	Re₃Sn_{0.06(3)}As_{6.94}	R_p	0.0734
		wR_p	0.0643
		R_F^2	0.0186
		Sn on 12 <i>d</i> site	0.02(1)
		Sn on 16 <i>f</i> site	0
Re₃Sn_{0.2}As_{6.8}	Re₃Sn_{0.06(7)}As_{6.94}	R_p	0.0854
		wR_p	0.0737
		R_F^2	0.0325
		Sn on 12 <i>d</i> site	0.02(1)
		Sn on 16 <i>f</i> site	0.00(1)
Re₃Sn_{0.3}As_{6.7}	Re₃Sn_{0.29(7)}As_{6.71}	R_p	0.0716
		wR_p	0.0639
		R_F^2	0.0313
		Sn on 12 <i>d</i> site	0.03(1)
		Sn on 16 <i>f</i> site	0.05(1)
Re₃Sn₂As₅	Re₃Sn_{1.13(7)}As_{5.87}	R_p	0.0729
		wR_p	0.0748
		R_F^2	0.0305
		Sn on 12 <i>d</i> site	0.15(1)
		Sn on 16 <i>f</i> site	0.17(1)

For comparison, the site preference for 12*d* and 16*f* in the isostructural compound Ir₃Sn₇ depends on the nature of the occupants, e.g. Li¹³⁶ and Mg.¹³⁷ It was proved that both the atomic size and the bonding interactions need to be taken into account. The lattice parameter *a* increases almost linearly with the increasing Sn content in Re₃Sn_{*x*}As_{7-*x*} (Fig.

4.3), which strongly supports the presence of Sn in the crystal structure. The lattice parameter (a) with the varying Sn composition is also listed in Tab. 4.3.

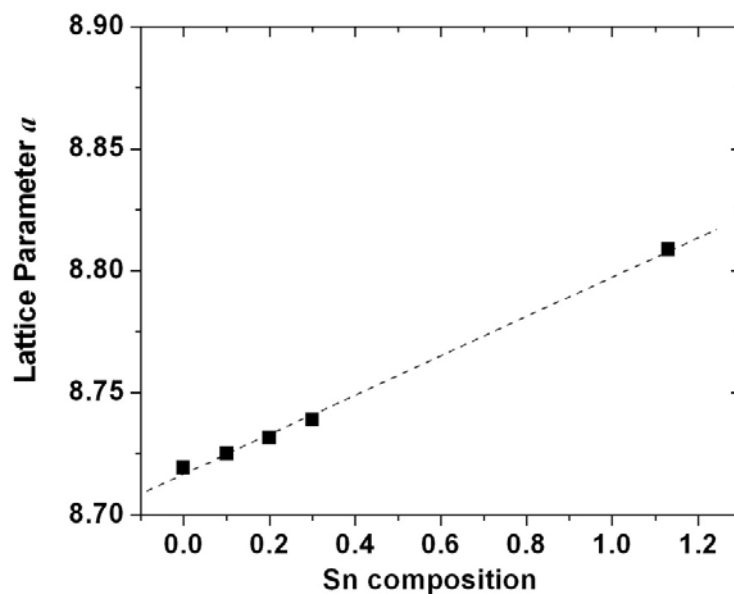


Fig. 4.3 Sn composition dependence of the lattice parameter a (Å).

The bond distances for the $\text{Re}_3\text{Sn}_x\text{As}_{7-x}$ series are listed in Tab. 4.3. We can conclude that the bond distances are usually lengthened because the cell size is enlarged by Sn/As substitution, with the exception of the short As2/Sn2–As2/Sn2 bond between the $E2$ cubes. These shortest bond distances become even shorter with increasing Sn composition due to the larger Sn radius, which also prove the Sn occupancy of the $16f$ ($E2$) site being favorable when more Sn atoms enter the crystal structure. In the case of the refined formula $\text{Re}_3\text{Sn}_{1.1}\text{As}_{5.9}$, the bonding distance between As2/Sn2–As2/Sn2 is longer than that of $\text{Re}_3\text{Sn}_{0.3}\text{As}_{6.7}$ even though it has larger Sn composition. That may be due to the significant increase in cell size of $\text{Re}_3\text{Sn}_{1.1}\text{As}_{5.9}$ which counteracts the effect of the large Sn radius.

Tab. 4.3 Interatomic distances (Å) and lattice parameter (Å) of $\text{Re}_3\text{Sn}_x\text{As}_{7-x}$.

Bonding type	Re_3As_7	$\text{Re}_3\text{Sn}_{0.1}\text{As}_{6.9}$	$\text{Re}_3\text{Sn}_{0.3}\text{As}_{6.7}$	$\text{Re}_3\text{Sn}_{1.1}\text{As}_{5.9}$
Lattice parameter a (Å)	8.7194(4)	8.7251(4)	8.7389(4)	8.8088(5)
Re–Re	2.785(3)	2.788(3)	2.788(3)	2.810(4)
Re–Sn1/As1	2.5866(8)	2.5885(9)	2.5917(9)	2.612(1)
Re–Sn2 /As2	2.547(2)	2.551(2)	2.560(2)	2.579(2)
Sn1/As1–Sn2/As2	3.0828(1)	3.0848(1)	3.0897(1)	3.1144(1)
Sn2/As2–Sn2/As2 (short)	2.554(7)	2.540(8)	2.515(8)	2.547(9)
Sn2/As2–Sn2/As2 (long)	2.885(4)	2.896(5)	2.917(5)	2.934(5)

4.3.2 Rietveld refinements on $\text{Re}_3E_x\text{As}_{7-x}$ ($E = \text{Si}, \text{Pb}$) and $\text{Mo}_{0.1}\text{Re}_{2.9}\text{As}_7$

Rietveld refinements on samples with Si/As and Pb/As exchanges were also performed. The Si substitution prefers As2 occupancy, possibly because the electronegativity effect is more important than size effect (Si has smaller radius than As, $r_{(\text{Si})} = 1.17 \text{ \AA}$ and $r_{(\text{As})} = 1.21 \text{ \AA}$). The Rietveld refinement pattern of $\text{Re}_3\text{Si}_{0.1}\text{As}_{6.9}$ is shown in Fig. 4.4. The residual factors and refined occupancy results are listed in Tab. 4.4. The lattice parameter, $a = 8.7221(4) \text{ \AA}$, is comparable with the value of Re_3As_7 and slightly smaller than that of $\text{Re}_3\text{Sn}_{0.1}\text{As}_{6.9}$.

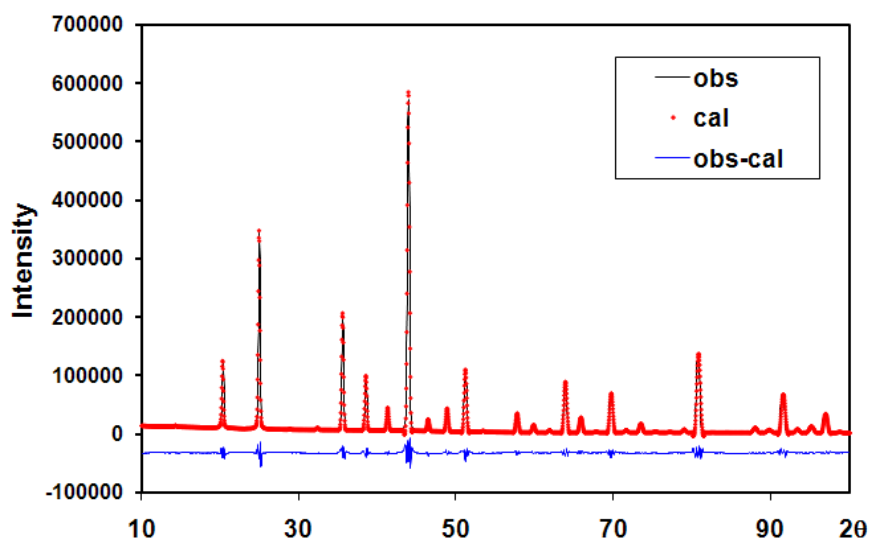


Fig. 4.4 Rietveld refinement on $\text{Re}_3\text{Si}_{0.1}\text{As}_{6.9}$.

The Pb substitution shows a similar trend as Sn substitution, with Pb preferring the As1 site at small Pb content. However, no pure $\text{Re}_3\text{Pb}_x\text{As}_{7-x}$ sample could be prepared when $x > 0.1$, most likely due to the large size difference between Pb and As atoms ($r_{\text{Pb}} = 1.50 \text{ \AA}$). The Rietveld refinement pattern of $\text{Re}_3\text{Pb}_{0.06}\text{As}_{6.94}$ is shown Fig. 4.5 and results are summarized in Tab. 4.4. The lattice parameter a , $8.7238(4) \text{ \AA}$, is also slightly larger than a of Re_3As_7 .

In the case of $\text{Mo}_x\text{Re}_{3-x}\text{As}_7$, MoAs_2 is always formed when $x > 0.1$. The Rietveld refinement pattern of $\text{Mo}_{0.1}\text{Re}_{2.9}\text{As}_7$ is shown in Fig. 4.6, with the refined results being included in Tab. 4.4. Mo has a similar size as Re ($r_{\text{Mo}} = 1.29 \text{ \AA}$; $r_{\text{Re}} = 1.28 \text{ \AA}$),¹³⁴ thus the lattice parameter a , $8.7220(3) \text{ \AA}$, is also close to the value of Re_3As_7 . It is difficult to refine the Mo fraction precisely, even with fixed thermal displacement parameters. It is possibly due to the very similar electron numbers of a Re site vs. a mixed Re/Mo site: Re has 75 electrons and the mixed occupied Re ($0.97\text{Re}+0.03\text{Mo}$) has 74 electrons.

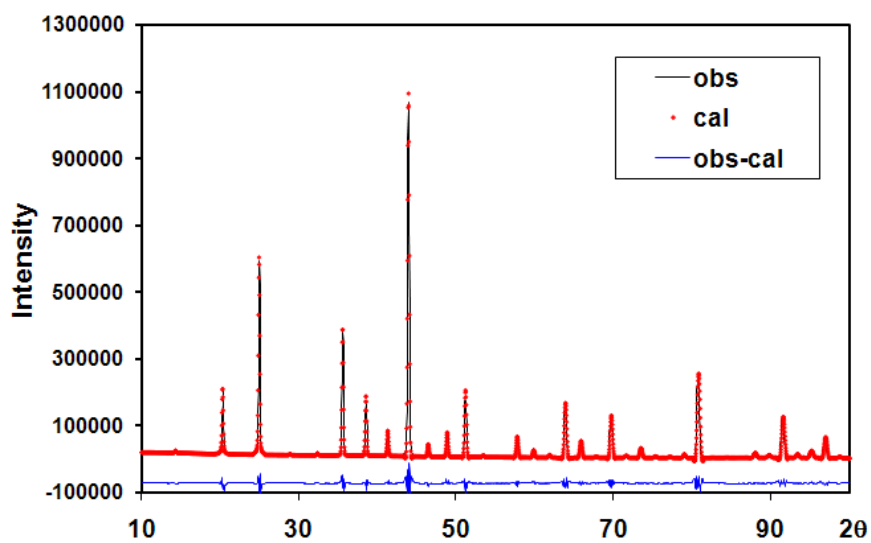


Fig. 4.5 Rietveld refinement on $\text{Re}_3\text{Pb}_{0.06}\text{As}_{6.94}$.

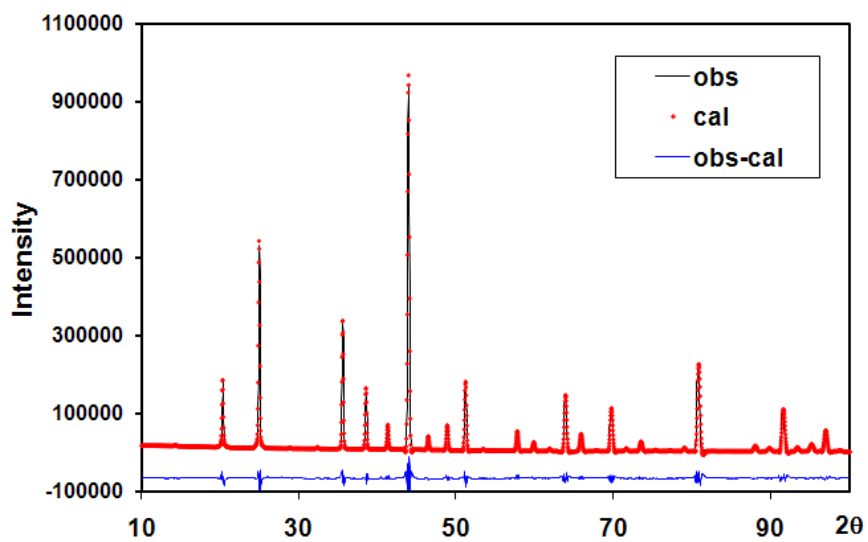


Fig. 4.6 Rietveld refinement on $\text{Mo}_{0.1}\text{Re}_{2.9}\text{As}_7$.

Tab. 4.4 Residual factors and refined E occupancies on preferred site.

Nominal composition	Refined composition	Residual factors and occupancy	Refined values
$\text{Re}_3\text{Si}_{0.1}\text{As}_{6.9}$	$\text{Re}_3\text{Si}_{0.12(4)}\text{As}_{6.88}$	R_p	0.0738
		wR_p	0.0607
		R_F^2	0.0277
		Si on 16 <i>f</i> site	0.03(1)
$\text{Re}_3\text{Pb}_{0.06}\text{As}_{6.94}$	$\text{Re}_3\text{Pb}_{0.09(1)}\text{As}_{6.91}$	R_p	0.0898
		wR_p	0.0668
		R_F^2	0.0957
		Pb on 12 <i>d</i> site	0.033(4)
$\text{Mo}_{0.1}\text{Re}_{2.9}\text{As}_7$	$\text{Mo}_{0.24(3)}\text{Re}_{2.76}\text{As}_7$	R_p	0.0909
		wR_p	0.0663
		R_F^2	0.0535
		Mo on 12 <i>e</i> site	0.08(1)

4.4 Electronic structure calculation

Re_3As_7 presents metallic properties with 56 valence electrons per formula unit. The electronic structure of Re_3As_7 is typical for metals with $\text{DOS} > 0$ at the Fermi level (Fig. 4.7, left). We attempted to vary the number of valence electrons to reach nearly the Fermi level in order to achieve semiconductivity.^{61, 64} According to the Rietveld refinement of $\text{Re}_3\text{Sn}_{1.1(1)}\text{As}_{5.9}$, around 1/3 of the Sn atoms are located on the As1 site and 2/3 on the As2 site. To simplify the calculation of Re_3SnAs_6 , equal amounts of Sn were assigned to both

sites, resulting in the space group $P1$ (with $a = b = c = 7.549 \text{ \AA}$, $\alpha = \beta = \gamma = 109.471^\circ$). This model then has 55 valence electrons per formula unit, and it exhibits a band gap of 0.33 eV at the Fermi level. A drastic reduction of the band gap down to 0.02 eV was observed by introducing Ni atoms into the center of the As2 cubes of this model (Fig. 4.7, right).

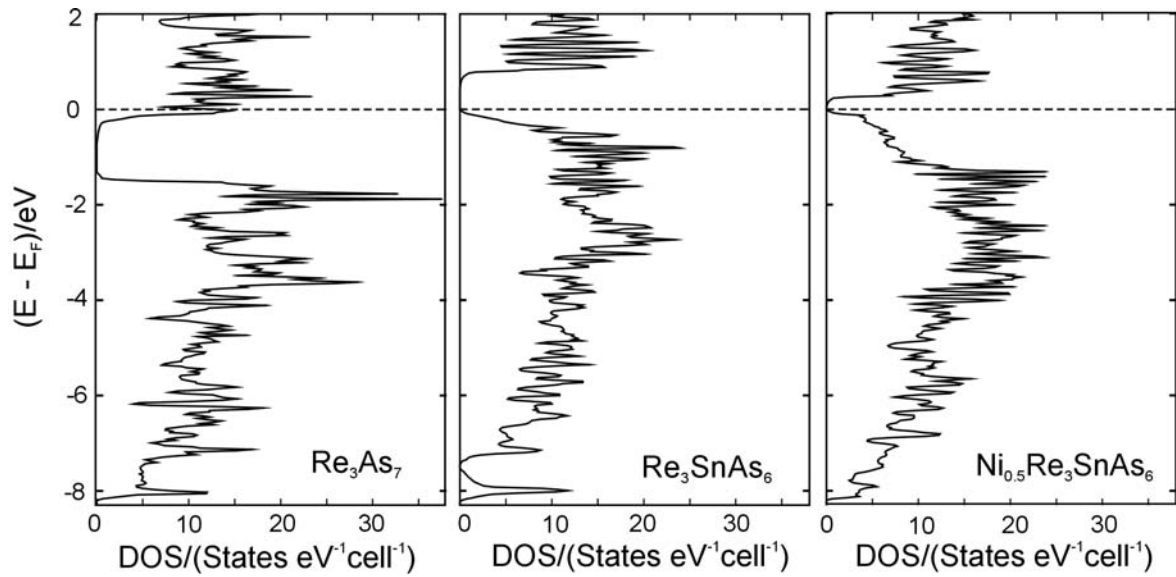


Fig. 4.7 Density of States (DOS) of Re_3As_7 , Re_3SnAs_6 and $\text{Ni}_{0.5}\text{Re}_3\text{SnAs}_6$. The Fermi level E_F (dashed horizontal line) was arbitrarily placed at 0 eV.

Further analysis was conducted on Re_3SnAs_6 . Five different models were calculated based on the structural data of Re_3As_7 (Fig. 4.8). Model I and II have Sn occupying only $E1$ (As1) sites and the models of III–V have Sn on the $E2$ (As2) site (referring to Fig. 4.1). Model I has two neighboring Sn atoms in $E1$ square, whereas the shortest Sn–Sn distance is along the diagonal of $E1$ square in model II. In model III, the Sn atoms form a short Sn–Sn distance between the two neighboring $E2$ cubes. The Sn atoms are interconnected along the As2 cube edge in model IV. In model V, the shortest Sn–Sn distance occurs along the face

diagonal of $E2$ cube. The calculations reveal that the electronic structure strongly depends on the Sn ordering. Model I and II exhibit metallic properties with both pseudo-gaps at the Fermi level. Model III–IV present band gaps of 0.3 eV (III), 0.65 eV (V) and 0.85 eV (IV) (Fig. 4.9). Because semiconducting properties were observed experimentally, we conclude the Sn must preferentially occupy the $E2$ (As2) site, which is also in accordance with our Rietveld refinement results of $\text{Re}_3\text{Sn}_{1.13(7)}\text{As}_{5.87}$.

The electronic structure calculations of the compounds having Pb or Mo atoms are shown in Fig. 4.10. The Pb atoms were placed on $E2$ position and the space group was reduced to $P3m$ and $F2mm$ in $\text{Re}_3\text{Pb}_{0.5}\text{As}_{6.5}$ and Re_3PbAs_6 , respectively. The Mo atoms were only distributed on Re site, resulting in the space group of $I4mm$ ($\text{Mo}_{0.5}\text{Re}_{2.5}\text{As}_7$) and $I4/mmm$ (MoRe_2As_7). Both Re_3PbAs_6 and MoRe_2As_7 are predicted to be semiconductors with band gaps of 0.48 eV (Re_3PbAs_6) and 0.61 eV (MoRe_2As_7). This prediction was confirmed by the physical property measurements experimentally.

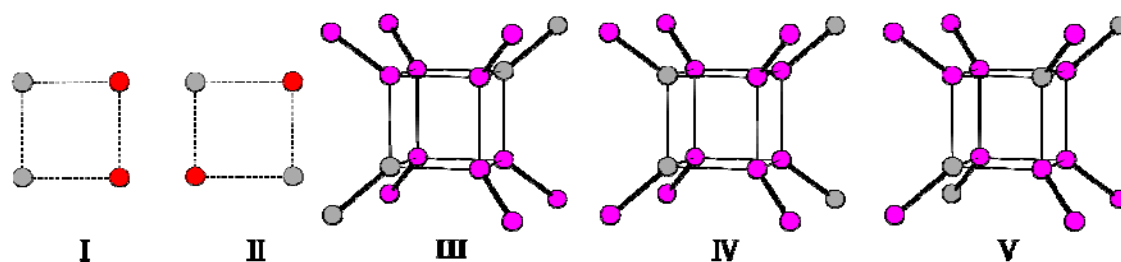


Fig. 4.8 Sn ordering of five models for Re_3SnAs_5 . Sn: grey; As1: red (in model I and II); As2: pink (in model III, IV and V).

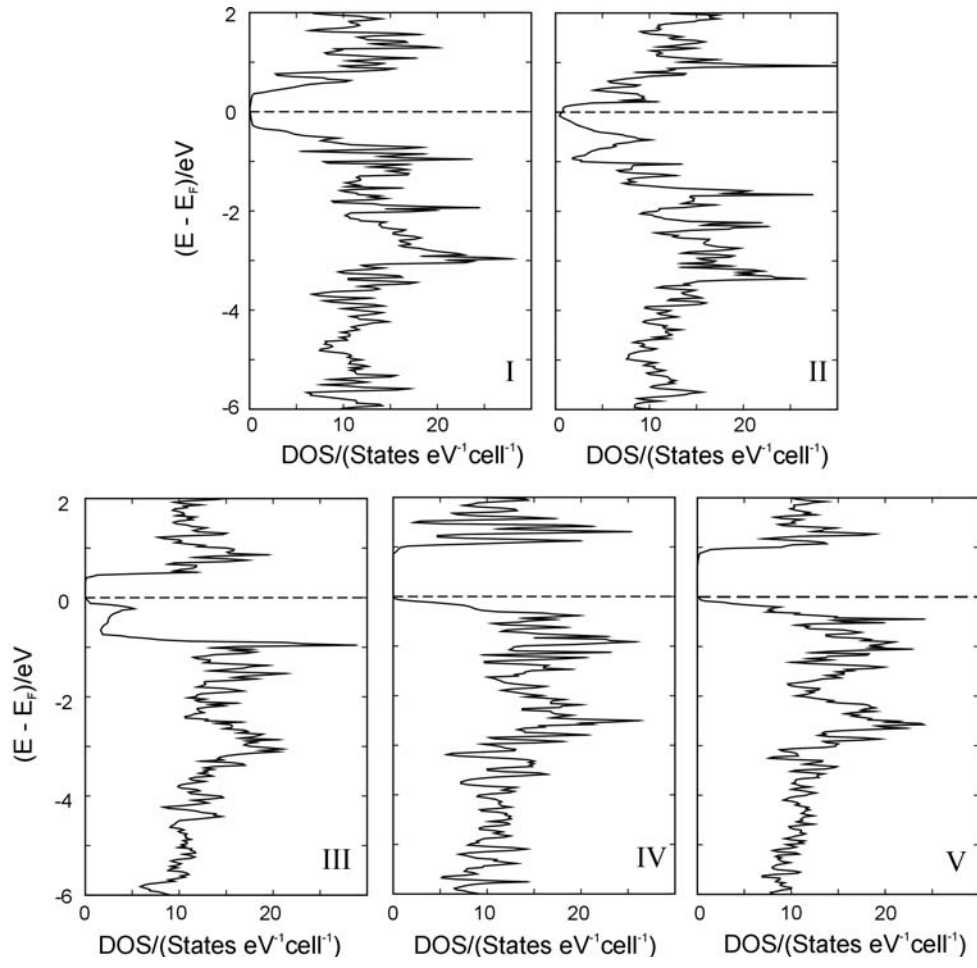


Fig. 4.9 The corresponding density of states of five models for Re_3SnAs_6 .

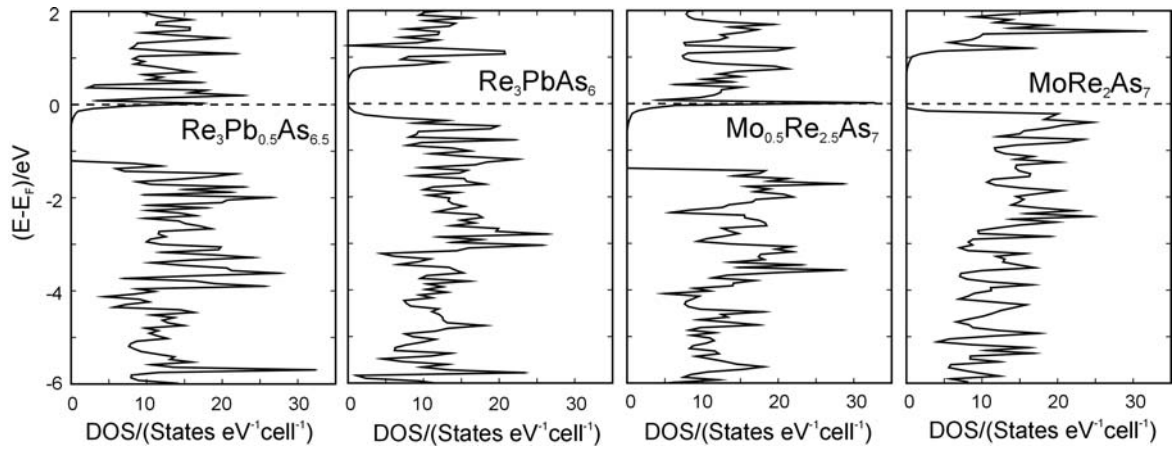


Fig. 4.10 Density of states of $\text{Re}_3\text{Pb}_{0.5}\text{As}_{6.5}$, Re_3PbAs_6 , $\text{Mo}_{0.5}\text{Re}_{2.5}\text{As}_7$ and MoRe_2As_7 .

4.5 Physical property measurements

4.5.1 $\text{Re}_3(\text{Sn,As})_7$ series samples

In contrast to the electron-deficient p -type semiconductor $\text{Mo}_3(\text{Sb,Te})_7$, the electron-rich $\text{Re}_3(\text{Sn,As})_7$ is an n -type semiconductor, like $\text{Re}_3\text{Ge}_x\text{As}_{7-x}$ ($x = 0.6, 1$).⁶⁴ A comparison of the Seebeck coefficient at 300 K measured on cold-pressed and hot-pressed pellets is shown in Tab. 4.5. $\text{Re}_3\text{Sn}_{0.2}\text{As}_{6.8}$ exhibits a larger Seebeck value, compared with the values of $\text{Re}_3\text{Sn}_{0.1}\text{As}_{6.9}$ and $\text{Re}_3(\text{Ge,As})_7$. The Seebeck coefficient of hot-pressed pellets measures to be around 80-85% of Seebeck coefficient of cold-pressed pellets, due to the higher density of hot-pressed pellets. Adding Ni increases the Seebeck coefficient to $(-116) \mu\text{V/K}$, while Co-doping does not demonstrate any improvement. For all samples, a smooth increase of their Seebeck coefficient with elevated temperature can be observed between 300 K and 550 K (Fig. 4.11), typical for degenerate semiconductors. Therefore the presence of a band gap can be assumed, as calculated for Re_3SnAs_6 .

Tab. 4.5 Comparison of Seebeck coefficient and electrical conductivity at 300 K.

Formula	S ($\mu\text{V/K}$) of cold-pressed pellets	S ($\mu\text{V/K}$) of hot-pressed pellets	σ ($\Omega^{-1}\text{cm}^{-1}$) of hot-pressed pellets
$\text{Re}_3\text{Ge}_{0.6}\text{As}_{6.4}$	-88	-72	1100
Re_3GeAs_6	-84	-69	760
$\text{Re}_3\text{Sn}_{0.1}\text{As}_{6.9}$	-85	-	
$\text{Re}_3\text{Sn}_{0.2}\text{As}_{6.8}$	-95	-78	730
$\text{Co}_{0.05}\text{Re}_3\text{Sn}_{0.2}\text{As}_{6.8}$	-86	-	
$\text{Ni}_{0.05}\text{Re}_3\text{Sn}_{0.2}\text{As}_{6.8}$	-116	-	

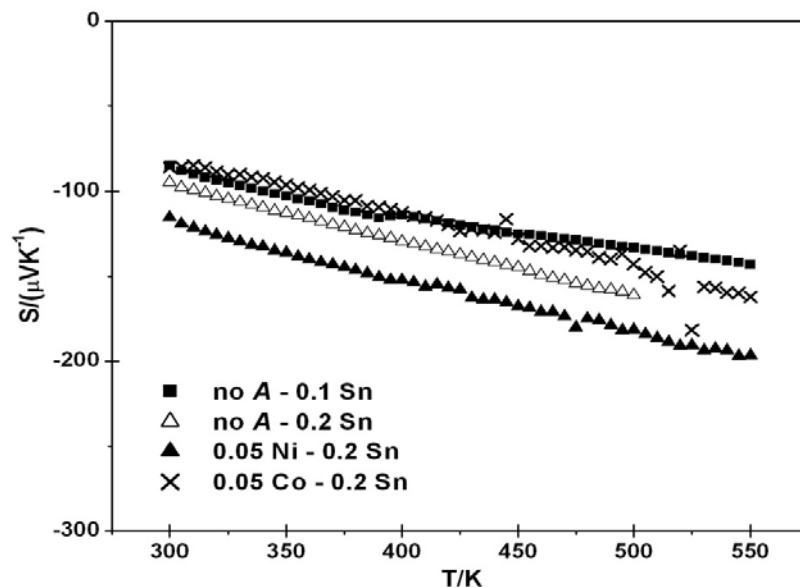


Fig. 4.11 Temperature dependence of the Seebeck coefficient of selected cold-pressed arsenides.

High-temperature Seebeck coefficient and electrical conductivity measurements of hot-pressed $\text{Re}_3\text{Sn}_{0.2}\text{As}_{6.8}$ were completed at Clemson University. The electrical conductivity decreases steadily with increasing temperature, as is expected for a degenerate semiconductor. However the slopes of the Seebeck coefficient and electrical conductivity curves change around 550 K, where the electrical conductivity values start to increase and the Seebeck coefficient starts to decrease (Fig. 4.12). As similar trends were observed in the measurements of $\text{Re}_3(\text{Ge},\text{As})_7$,⁶⁴ we decided to utilize DSC analysis and high-temperature X-ray diffraction to investigate a suspected phase transition. Since we did not have a sufficient amount of $\text{Re}_3\text{Sn}_{0.2}\text{As}_{6.8}$ available, $\text{Re}_3\text{Sn}_{0.3}\text{As}_{6.7}$ was selected for the X-ray experiment, considering the similar compositions of these two compounds.

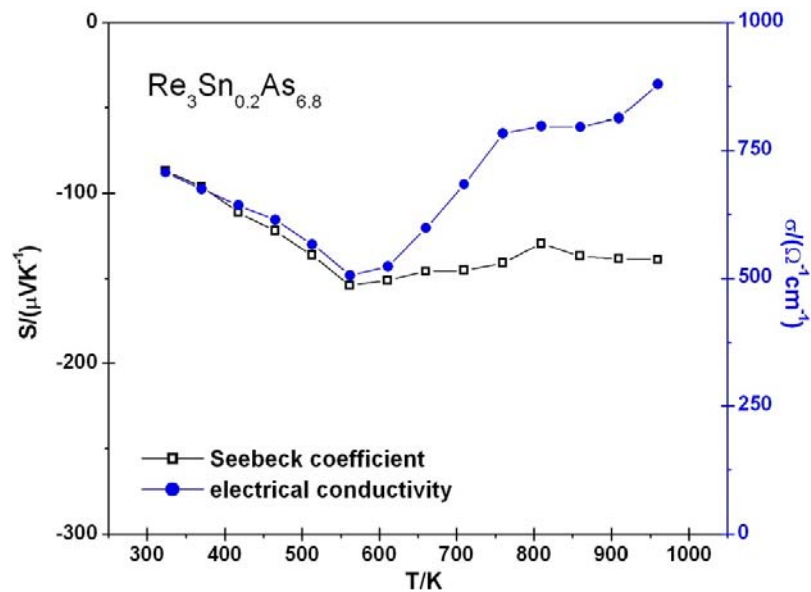


Fig. 4.12 High-temperature measurements of Seebeck coefficient and electrical conductivity of hot-pressed $\text{Re}_3\text{Sn}_{0.2}\text{As}_{6.8}$.

The DSC and TG measurements of $\text{Re}_3\text{Sn}_{0.2}\text{As}_{6.8}$ were carried out simultaneously on a NETZSCH STA 409PC Luxx apparatus between 300 K and 1023 K (Fig. 4.13). The slope of the DSC curve is due to instrument settings, as confirmed by our baseline measurement. No extra peak indicating a phase transition or decomposition can be observed. The TG curve does not reveal any apparent weight loss until the temperature reaches 990 K. This indicates a potential for high temperature thermoelectric applications.

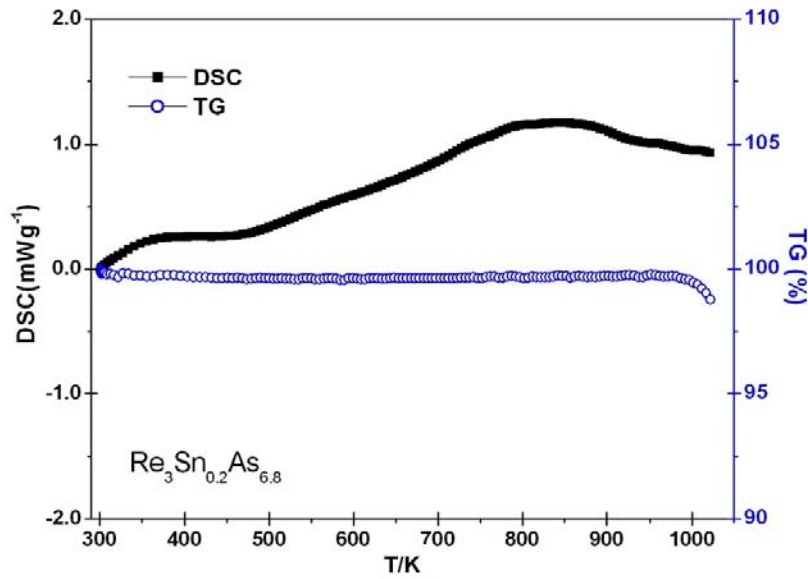


Fig. 4.13 Thermal analysis of $\text{Re}_3\text{Sn}_{0.2}\text{As}_{6.8}$.

A FUR 1400 high temperature furnace with a ceramic (Al_2O_3) sample holder was installed on our INEL diffractometer for high temperature PXRD. A twenty-minute measurement was set for every 20 K, starting at 303 K and rising up to 673 K. For particular observation of the suspected phase transition, 10 K intervals were placed between 523 K and 573 K. XRD patterns of the measurements at 373 K, 523 K and 673 K are stacked for the comparison (Fig. 4.14). No additional peaks were observed and $\text{Re}_3\text{Sn}_{0.3}\text{As}_{6.7}$ remained stable up to 673 K. Thus, we conclude that the turning points in the Seebeck coefficient and electrical conductivity are not due to a crystallographic phase transition. We suppose an increase of the charge carrier concentration (e.g. the excitation of electrons from the valence band) is the real reason behind the turning point. However, this assumption needs to be verified by high temperature Hall measurements.

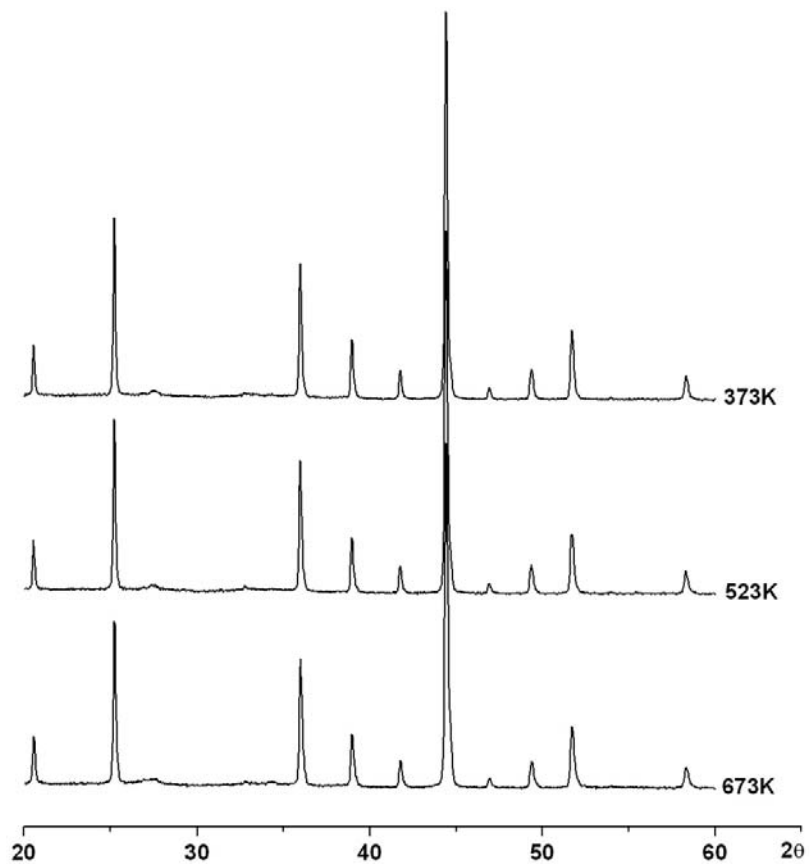


Fig. 4.14 Comparison of high temperature XRD patterns of $\text{Re}_3\text{Sn}_{0.3}\text{As}_{6.7}$.

We calculated the power factor of $\text{Re}_3\text{Sn}_{0.2}\text{As}_{6.8}$ and compared it with the values of $\text{Re}_3(\text{Ge,As})_7$ (Fig. 4.15). $\text{Re}_3\text{Sn}_{0.2}\text{As}_{6.8}$ displays a larger power factor than Re_3GeAs_6 over the whole range, but smaller than $\text{Re}_3\text{Ge}_{0.6}\text{As}_{6.4}$. This is mostly because of the smaller electrical conductivity of $\text{Re}_3\text{Sn}_{0.2}\text{As}_{6.8}$ and Re_3GeAs_6 (Tab. 4.5). The power factors of all three samples increase steadily with increasing temperatures.

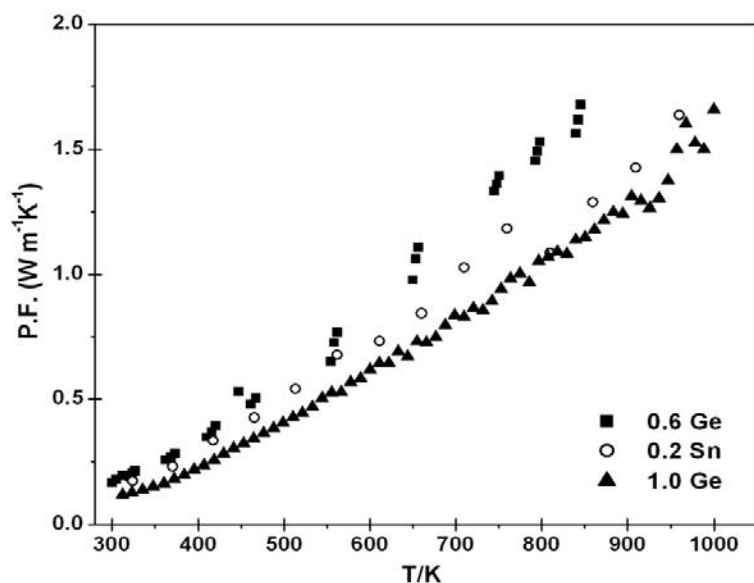


Fig. 4.15 Comparison of power factors of $\text{Re}_3\text{Sn}_{0.2}\text{As}_{6.8}$, Re_3GeAs_6 and $\text{Re}_3\text{Ge}_{0.6}\text{As}_{6.4}$.

Based on the electronic structure calculation, $\text{Re}_3(\text{Sn,As})_7$ should be a semiconductor, which is in accordance with the measured Seebeck coefficient results. The power factor of $\text{Re}_3\text{Sn}_{0.2}\text{As}_{6.8}$ is larger than the value of Re_3GeAs_6 , but smaller than the value of $\text{Re}_3\text{Ge}_{0.6}\text{As}_{6.4}$. Transition metal atoms (Ni, Co) were intercalated into the center of cubic void to optimize the thermoelectric properties. Ni-doping improved the Seebeck coefficient significantly. The bulk samples of $\text{Re}_3(\text{Sn,As})_7$ and $A_x\text{Re}_3(\text{Sn,As})_7$ ($A = \text{Fe, Co, Ni, Cu}$) were prepared and sent to Clemson for high-temperature physical property measurements on the hot-pressed pellets. Rietveld refinement results of these compounds indicate that Sn atoms can occupy both As1 and As2 sites. The site preference depends on the substitution amount and thus on the balance of size effect and electronegative effect.

4.5.2 $\text{Re}_3(\text{Si}, \text{As})_7$, $\text{Re}_3(\text{Pb}, \text{As})_7$ and $(\text{Mo}, \text{Re})_3\text{As}_7$ series samples

Seebeck coefficient measurements of $\text{Re}_3\text{Si}_{0.2}\text{As}_{6.8}$, $\text{Re}_3\text{Si}_{0.4}\text{As}_{6.6}$ and the compounds with added transition metal atoms are shown in Fig. 4.16. $\text{Re}_3\text{Si}_{0.4}\text{As}_{6.6}$ demonstrates a larger Seebeck coefficient compared to $\text{Re}_3\text{Si}_{0.2}\text{As}_{6.8}$, because the less electron-rich compound has fewer n -type charge carriers. The compounds with transition metal atom intercalations exhibit smaller Seebeck coefficient values than the samples without.

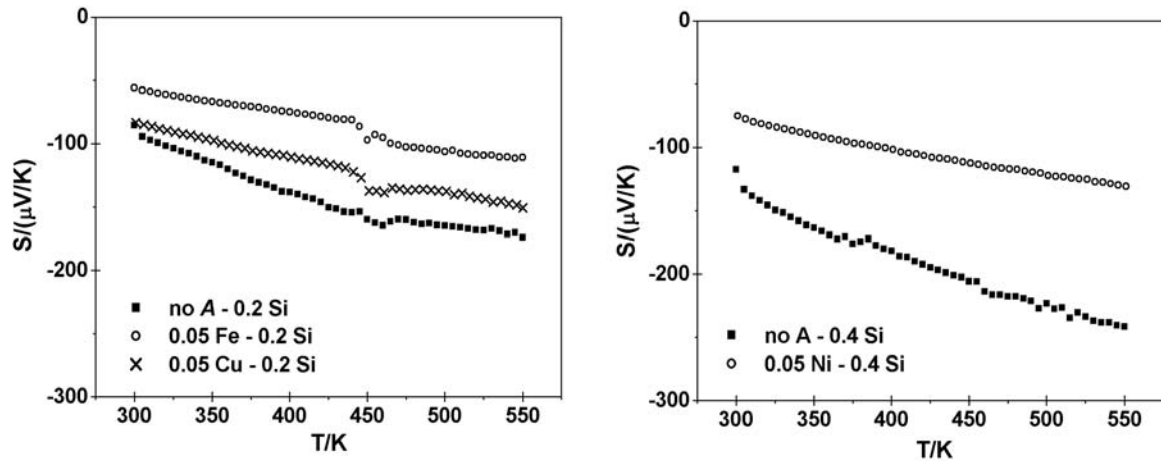


Fig. 4.16 Seebeck coefficient measurement for $\text{Re}_3(\text{SiAs})_7$ variants.

The Seebeck coefficient trends of the $\text{Re}_3(\text{Pb}/\text{As})_7$ series and $\text{Mo}_{0.1}\text{Re}_{2.9}\text{As}_7$ are shown in Fig. 4.17. $\text{Re}_3\text{Pb}_{0.1}\text{As}_{2.9}$ demonstrates a higher Seebeck coefficient than $\text{Re}_3\text{Pb}_{0.06}\text{As}_{2.94}$ for the same reason as discussed above for the $\text{Re}_3(\text{Si}/\text{As})_7$ case. The Ni containing sample, $\text{Ni}_{0.05}\text{RePb}_{0.1}\text{As}_{6.9}$ displayed comparable Seebeck coefficient values with $\text{Re}_3\text{Pb}_{0.06}\text{As}_{6.94}$.

The Seebeck coefficient of $\text{Mo}_{0.1}\text{Re}_{2.9}\text{As}_7$ confirms its semiconductivity. Future research could be focused on the substitution of both cation and anion sites to further optimize the thermoelectric properties of these series materials. Bulk samples of $\text{Re}_3\text{Si}_x\text{As}_{7-x}$,

$\text{Re}_3\text{Sn}_x\text{As}_{7-x}$, $\text{Re}_3\text{Pb}_x\text{As}_{7-x}$, and samples with additional transition metal atoms (Fe, Co, Ni, Cu) have been prepared and sent to Clemson University, where hot-pressed pellets will be made and the physical properties will be measured at the high temperature range.

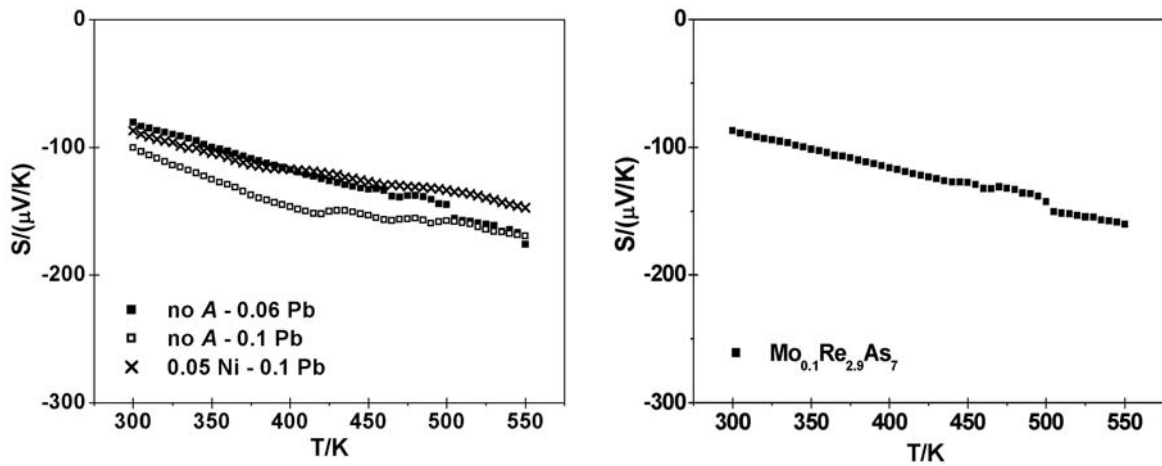


Fig. 4.17 Seebeck coefficient of $\text{Re}_3(\text{PbAs})_7$ variants (left) and $\text{Mo}_{0.1}\text{Re}_{2.9}\text{As}_7$ (right).

5 LaAsSe and LaCu_xAsSe with the distorted square nets

Thermoelectric materials mainly comprise tellurides, antimonides, clathrates and some layered structure oxides. The antimonides, e.g. LaFe₃CoSb₁₂ (filled skutterudite), Yb₁₄MnSb₁₁ (Zintl phase) and Mo₃Sb_{7-x}Te_x (Ir₃Ge₇ type) all have the different types of Sb atom units (see section 1.4). For instance, our research on Mo₃Sb_{7-x}Te_x revealed that eight Sb₂ atoms form an empty cube by interconnecting “hypervalent” Sb₂–Sb₂ bonds. Many planar square nets with “half” bonds exist in pnictides and chalcogenides, which are prone to undergo Peierls distortion. The distortions often induce the formation of superstructures, thereby opening a narrow band gap and inducing semiconducting property, which are favorable for thermoelectric applications.

5.1 Introduction of different structure types

The most common structures exhibiting undistorted square nets include ZrSiS (PbFCl)¹¹⁶ and HfCuSi₂¹³⁸ structure types, as shown in Fig. 5.1. There are over 200 compounds that adopt ZrSiS structure type. ZrSiS comprises the stacking square nets of Si into the Zr–S layers. Zr is coordinated by four Si atoms and four S atoms from the square nets and the fifth bonded S atom exists in the adjacent Zr–S slab. HfCuSi₂ is also called “filled” PbFCl structure type, with the Cu layer inserted in the middle of the unit cell. The Si atoms occupy two different sites with different coordination environment. Si1 atoms have four Hf neighbors and four Si1 atoms forming a square in Si layers. The Si2 atoms are coordinated by four Hf atoms and four Cu atoms in the shape of distorted square antiprism.

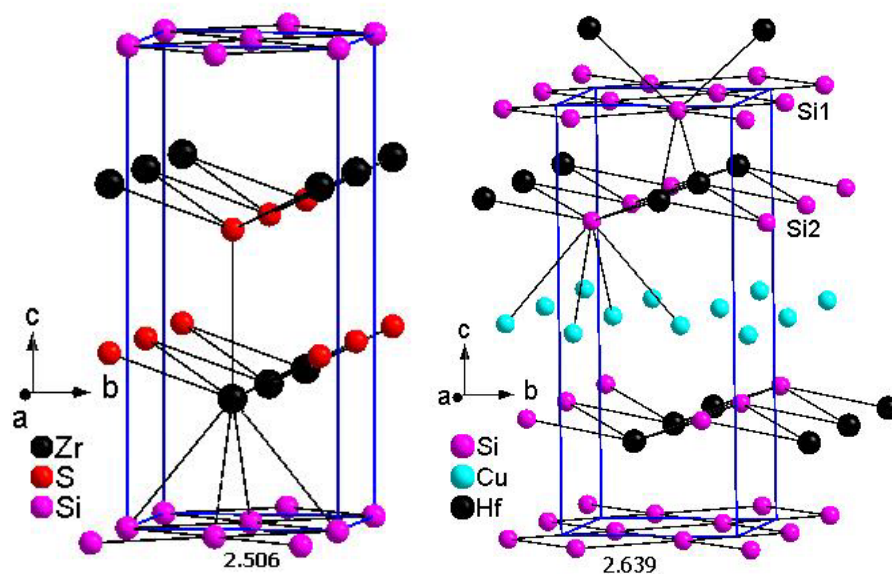


Fig. 5.1 Regular square net structures: ZrSiS (left) and HfCuSi₂ (right).

The compounds comprising distorted square nets often possess one of three structure types, NbPS¹³⁹, CeAsS¹¹⁷ or GdPS¹⁴⁰. NbPS has alternating short and long P–P distances in P chains (Fig. 5.2). If the longer P–P interaction is disregarded, the valence description can be derived as Nb⁴⁺P²⁻S²⁻ because there are no P–S or S–S interactions. Even though the distorted P layer occurs in NbPS, it exhibits metallic property because of the partial filled *d* bands of Nb.¹⁴¹ The pnictogen atom *Q*, such as As in CeAsS and P in GdPS, owns six electrons per atom, corresponding to the formula of RE³⁺*Q*¹⁻S²⁻ (RE: rare earth elements; *Q*: pnictogen atoms). In CeAsS, As atoms form the zigzag chains, while the P atoms form the cis-trans chains in GdPS (Fig. 5.3).

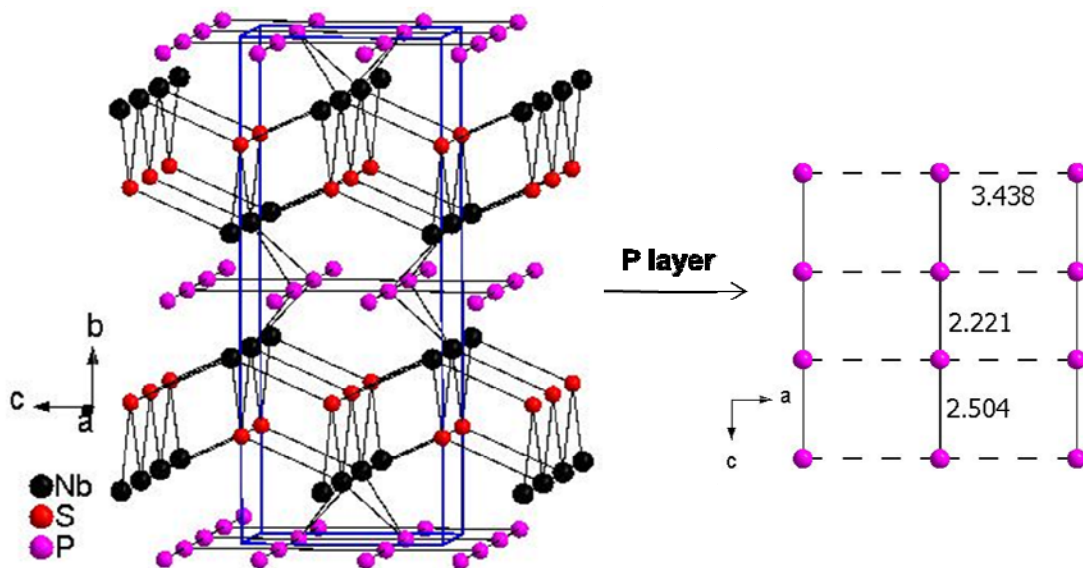


Fig. 5.2 Crystal structure of NbPS with distorted P layers.

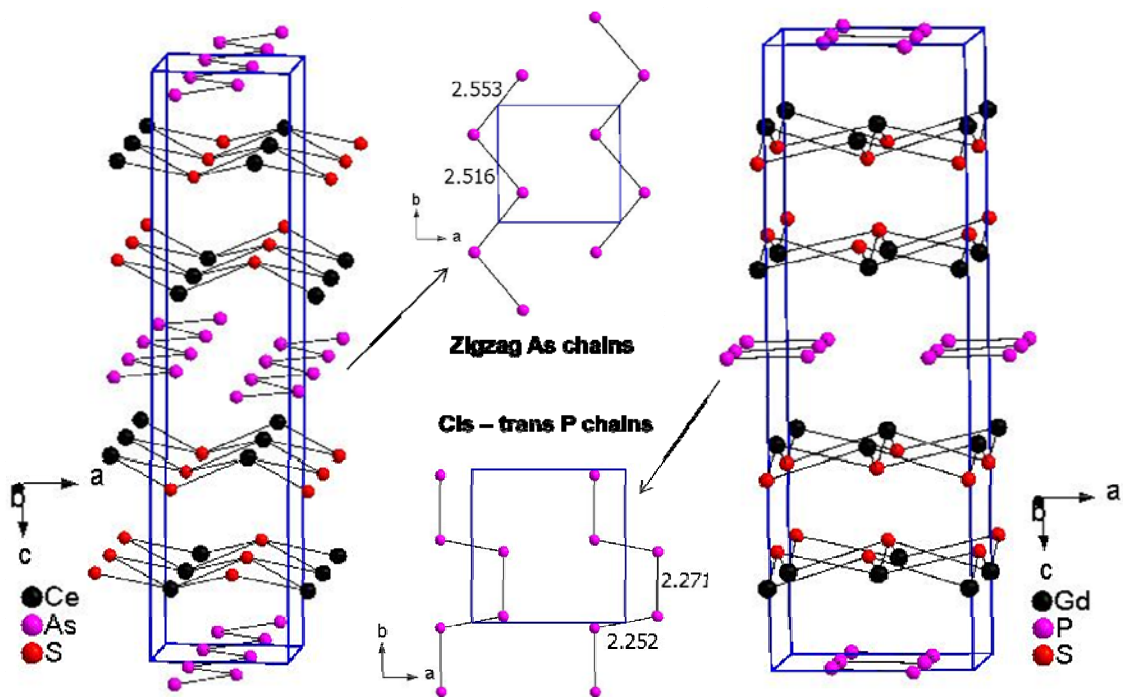


Fig. 5.3 Crystal structure of CeAsS (left) and GdPS (right) with distorted square nets, contacts between Ce-As and Gd-P are not shown for clarity.

CeSbTe was also reported having zigzag Sb chains, similar to the distortion of As chains in CeAsS.¹⁴² However, the ratio of long to short bond distance is smaller than that of CeAsS. Referring to the trend in Tab. 5.1, we can deduce that the heavier elements prefer hypervalent bonding, or less distortion. In fact, the higher group elements substitution will decrease the energy gap between metal *d* states and the valence band. If they do overlap, additional electrons will enter the metal bands instead of the antibonding part of the valence band, therefore an undistorted structure would be preferred.⁶⁵

Tab. 5.1 Comparison of ratios of long to short bond distance in the distorted square nets.

Compound	Long interchain distance (Å)	Short bond distance (Å)	Ratio of long/short
NbPS	3.438	2.221	1.548
GdPS	3.222	2.252	1.431
CeAsS	3.152	2.516	1.253
CeSbTe	3.182	2.986	1.066

The crystal structure and physical properties of ZrSbTe and HfSbTe were reported by the Kleinke group in 2007, both of them adopt NbPS structure type.¹⁴³ The distorted Sb chains lead to a band gap opening within the Sb bands, however the overlap of metal *d* states with Te *p* states leads to metallic properties for both compounds. Therefore, using more electropositive metal atoms could open a band gap.

5.2 Sample preparation

The materials were synthesized from mixtures of the pure elements: arsenic (powder, -20 mesh, 99%), antimony (powder, -100 mesh, 99.5%), tellurium (broken ingot, 99.99%),

selenium (powder, -200 mesh, 99.999%) were purchased from Alfa Aesar. Arsenic powders were purified using the same method described in section 4.1. Lanthanum ingot (99.9%) was acquired from Hefa Rare Earth Canada. The surface of the La ingot was rasped to remove the oxide layer, and then a file was employed to produce coarse powder, which was further ground into fine powder in a mortar in the glove box. Two chloride salts, LiCl (99%, anhydrous, Alfa Aesar) and RbCl (99%, anhydrous, Alfa Aesar) were chosen to grow single crystals by molten salt flux method. The salt mixture was heated in vacuum line to remove the moisture before usage. The desired weighted elements were loaded into a Tamman crucible (Al_2O_3) to prevent tube attack. The loaded Tamman crucible was placed into a silica ampoule in an argon-filled glove box, which was then evacuated, sealed and put into a programmable box furnace. Phase pure compounds were obtained after heating the element mixtures at 1173 K for 5 days. The salt flux of LiCl/RbCl (mole ratio: 55:45) was applied to help growing suitable-sized single crystals. The reaction temperature was reduced to 873 K because of low eutectic point of LiCl/RbCl (~593 K). The sample was kept at 873 K for 3 to 4 days and cooled down to 573 K with 1.5 K/hour. The final product was washed free of chloride salts with water and then dried with acetone under the vacuum.

5.3 Characterization of lanthanum pnictide chalcogenide compounds

5.3.1 Determination of the properties of LaSbTe

Compared with Hf and Zr, La is the more electropositive element. Thus, we decided to explore whether LaSbTe would be a semiconducting material. The crystal structure of LaSbTe was reported in 1996, having distorted zigzag Sb chains.¹⁴⁴ However, the physical

properties have not been examined. Based on our LMTO calculation (Fig. 5.4 left), LaSbTe would be a semimetal because of the slight overlap of the bands near the Fermi level. LaSbTe was synthesized and the Seebeck coefficient was examined (Fig. 5.4 right). The Seebeck coefficient ranges from 22 $\mu\text{V}/\text{K}$ to 38 $\mu\text{V}/\text{K}$ at 300 K and 550 K, which is between the values of HfSbTe and ZrSbTe,¹⁴³ in accordance with the prediction of LMTO calculation. In order to enhance the energy differences between the conduction and the valence band, the elements of the same main group but in the period 4 were chosen, thus the target compound would be LaAsSe.

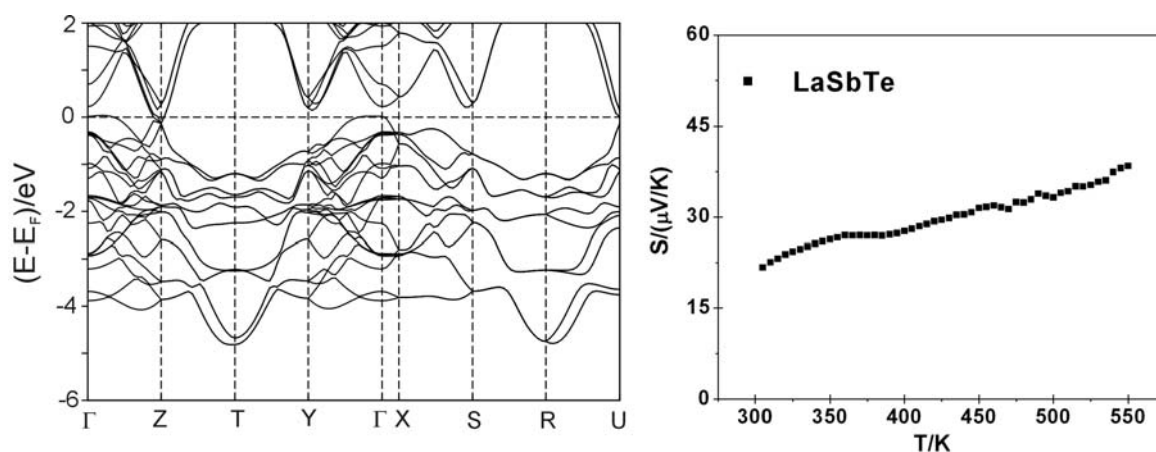


Fig. 5.4 Band structure (left) and Seebeck coefficient (right) of LaSbTe.

5.3.2 LaAsSe

It is difficult to obtain pure ternary LaAsSe if equivalent amounts of each element are used. Trace amounts of La_2Se_3 are always formed. Pure samples were prepared using a slight excess of arsenic (5%). Extra unreacted As crystallized on the wall of the quartz tube and could easily be separated and removed from the powder product. Salt flux LiCl/RbCl was

applied for growing single crystals. Many tiny and thin plate-like crystals were observed after washing and drying the product powder. However, it was hard to pick suitably size crystals for structure determination. Attempts at increasing the size of single crystals failed, such as using different flux medium (LiCl/KCl), slowing down the cooling rate, changing the temperature profile and applying chemical transport reactions with I₂ as a medium. Therefore, Rietveld refinement was employed to determine the structure information based on an appropriate model.

LaAsSe displays a similar powder XRD pattern to the recently published CeAsSe,¹⁴⁵ adopting the GdPS structure type. Hence CeAsSe was chosen as starting model and Ce on 4*c* site was replaced by La. The refinement converged with residual values of $R_p = 0.0303$ and $R_{wp} = 0.0463$. The refinement results are listed in Tab. 5.2. The preliminary refinement revealed the occupancies of all the elements equal to 1 within the range of 3 times standard deviations, thus the refinement was performed based on the fixed occupancy of 1. The crystallographic data in Tab. A.1 indicates the lattice parameters are larger than those of CeAsSe,¹⁴⁵ due to slightly larger radius of La atom.

Tab. 5.2 Atomic positions and displacement parameters (\AA^2) of LaAsSe.

atom	site	<i>x</i>	<i>y</i>	<i>z</i>	U_{eq}
La1	4 <i>c</i>	0.010(1)	0.25	0.3539(2)	0.0138(8)
La2	4 <i>c</i>	0.491(2)	0.25	0.6365(2)	0.0138(8)
Se1	4 <i>c</i>	0.003(3)	0.25	0.1822(5)	0.011(1)
Se2	4 <i>c</i>	0.481(3)	0.25	0.8122(5)	0.011(1)
As	8 <i>d</i>	0.2890(8)	0.0324(8)	0.0034(6)	0.010(2)

LaAsSe crystallizes in GdPS structure type. La and Se atoms form the slabs perpendicular to the c axis. Each La atom is coordinated by 4 As and 5 Se (4 Se atoms from the same layer and 1 Se atom from an adjacent layer), forming a capped distorted square antiprism. As atoms form the infinite cis–trans chains between the slabs (Fig. 5.5). The alternate As bond distances are 2.501(7) Å and 2.536(7) Å with a bond angle of 98.7(2)°, comparable to the single As–As bond distance of 2.52 Å.¹⁴⁶ The long interatomic distances (non-bonding) between the chains are 3.291(7) Å and 3.406(7) Å, thus the ratio of long to short distance is 1.363, between the ratio of CeAsS and GdPS. The interatomic bond distances are listed in Tab. A.2 in Appendix.

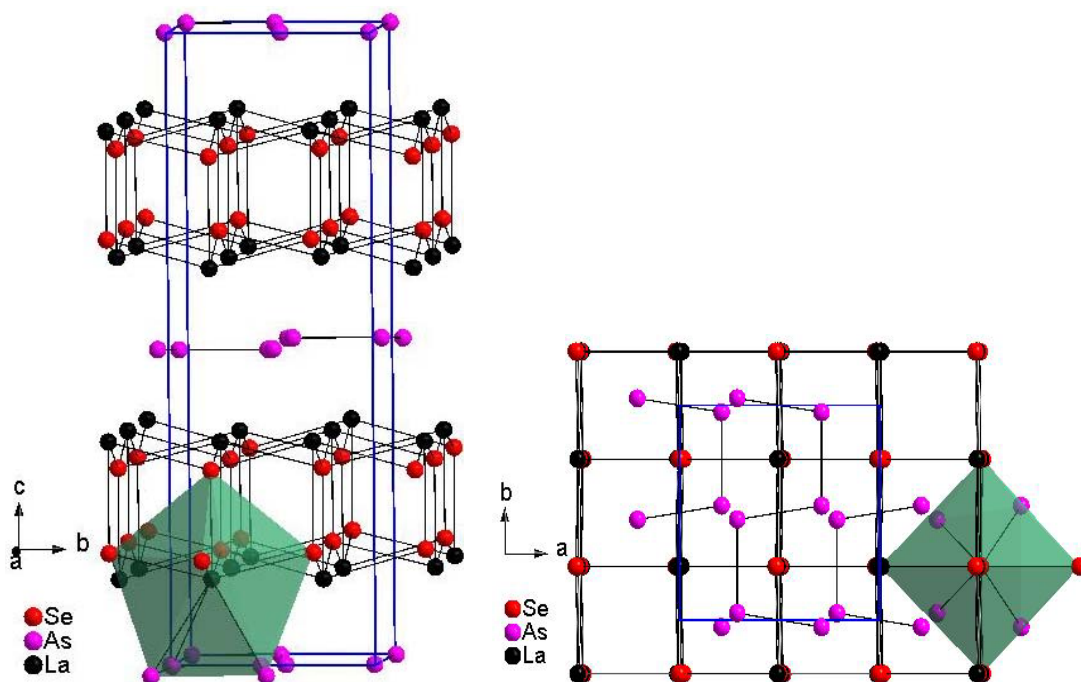


Fig. 5.5 Crystal structure of LaAsSe: left, along a axis; right, along c axis. La coordination environment is shown by the green polyhedron. La–As contacts are removed for clarity.

The LMTO calculation was performed based on the crystal structure information from Rietveld refinement. A band gap of 0.33 eV appears near the Fermi level, indicating semiconductivity, which is further confirmed by Seebeck coefficient measurement (Fig. 5.6 right). LaAsSe exhibits a much larger Seebeck coefficient than LaSbTe, ranges from -237 $\mu\text{V/K}$ to -346 $\mu\text{V/K}$ between 300 K to 550 K. Thus, an obvious band gap is opened by distorted As atoms and semiconductivity is achieved as a consequence.

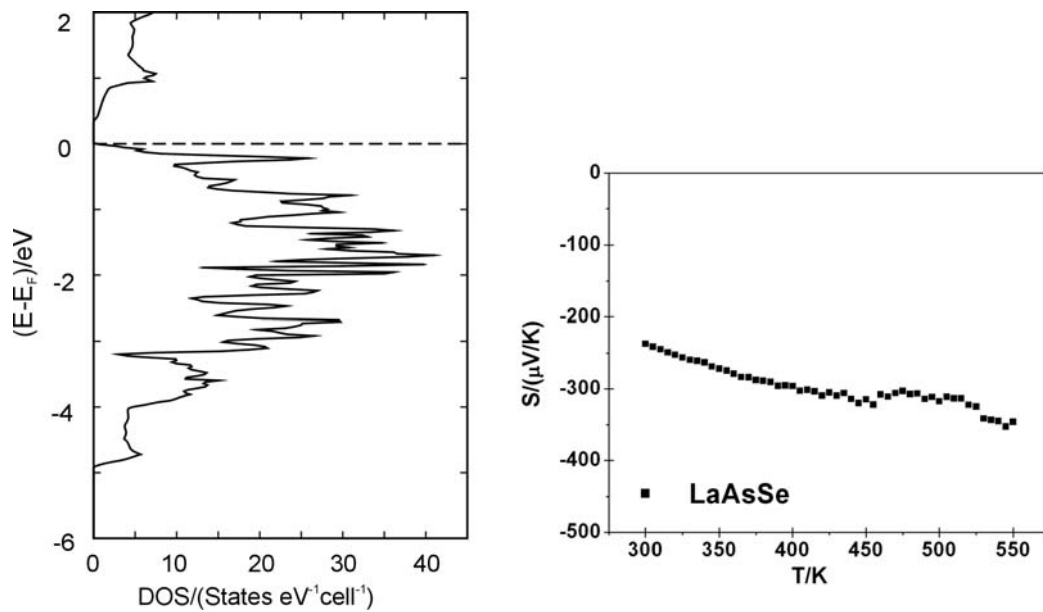


Fig. 5.6 DOS (left) and Seebeck coefficient (right) of LaAsSe.

5.3.3 LaCu_xAsSe

Inspired by the structure of HfCuSi₂, we consider to introduce Cu atoms into the LaAsSe structure to try to explore a new structure. First, equal molar amounts of La, Cu, As, Se were used for the synthesis. However, this led to the formation of a mixture of binary and

ternary compounds (e.g. LaAsSe, La₂Se₃ and Cu₃As). The EDX results showed 5% – 10% Cu content in quaternary LaCu_xAsSe. Thus, the ratio of starting materials was adjusted to La:Cu:As:Se = 1: 0.2: 1:1. The molten salt (LiCl/RbCl) flux method was used as well. Thin plate-like black crystals were obtained and some of them were selected for single crystal structure determination.

The refined formula is LaCu_{0.12(1)}AsSe based on single crystal data information. This new compound adopts a derivative structure of the ZrSiS type with deficient Cu sites inserted between the La and As layers (Fig. 5.7). Hypervalent bonding (bond distance of As–As is 2.94 Å) exists between As-As atoms. *R*₁ and *wR*₂ are 0.0252 and 0.0550, respectively. Because only 10% Cu atoms exist in the structure, equal to 0.1*30 = 3 electrons, it is difficult to refine anisotropic displacement parameters of Cu precisely. Thus, the *U*_{eq} of Cu was fixed to 0.01 to conduct the refinement. Atomic coordinates and displacement parameters are listed in Tab. 5.3. Crystallographic data are shown in Tab. A.3.

Tab. 5.3 Atomic positions and displacement parameters (Å²) of LaCu_{0.12(1)}AsSe (*U*₁₁ = *U*₂₂).

atom	site	<i>x</i>	<i>y</i>	<i>z</i>	<i>U</i> ₁₁	<i>U</i> ₃₃	<i>U</i> _{eq}
La	2 <i>c</i>	0.25	0.25	0.71874(9)	0.0087(3)	0.0181(4)	0.0118(3)
Cu	2 <i>c</i>	0.25	0.25	0.105(2)			0.01
As	2 <i>a</i>	0.75	0.25	0	0.0640(1)	0.0117(7)	0.0466(7)
Se	2 <i>c</i>	0.25	0.25	0.3705(2)	0.0089(4)	0.0121(6)	0.0099(3)

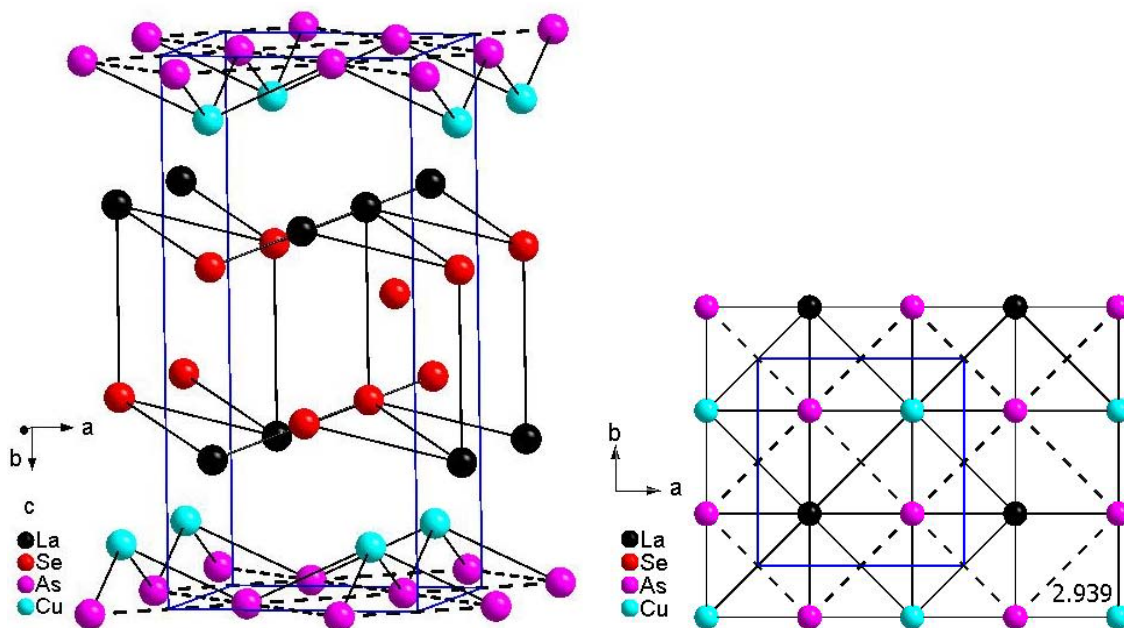


Fig. 5.7 Crystal structure view of $\text{LaCu}_{0.12(1)}\text{AsSe}$: left, along the b axis; right, along the c axis. Dashed lines represent As–As hypervalent bonds.

The As atoms show much larger displacement parameters along a and b than along the c axis. Therefore, the As atom was allowed to deviate from the 4-fold rotation axis, resulting in four split sites. Thereby the residual factors were reduced to 0.0161 and 0.0355 for $R1$ and $wR2$. The crystal structure with As split sites is shown in Fig. 5.8, which shows full Cu occupancy. The comparison of bond distances between these two models is listed in Tab. A.4. For comparison, the U_{eq} of Cu was also set to 0.01 for refinement in the As split sites model. Atomic coordinates and displacement parameters are listed in Tab. 5.4. Compared with U values of As in Tab. 5.3, the difference between U_{11} and U_{33} decreased after introducing As split sites. Attempts were also made to refine at lower symmetry and the space group was changed to $P2_1$. However, the U_{eq} of As remained much larger than the

thermal displacement parameters of the other elements, and residual factors were not improved. Therefore the As split site model in $P4/nmm$ is considered as the most reasonable one.

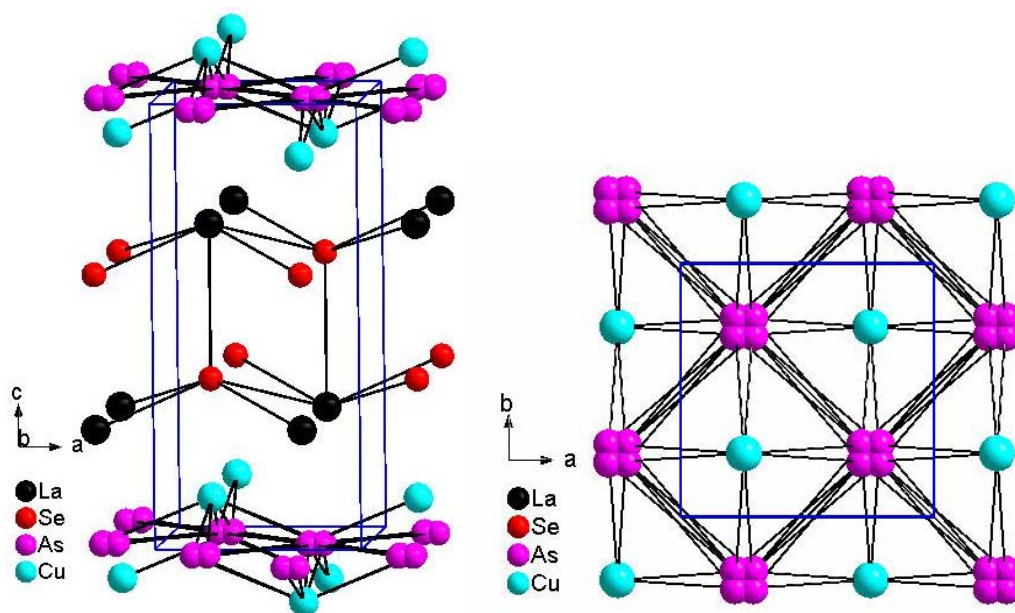


Fig. 5.8 Left: crystal structure view of $\text{LaCu}_{0.12(1)}\text{AsSe}$ with As split sites (along the b axis); right: view of As layer surrounded by Cu atom (along the c axis).

Tab. 5.4 Atomic positions and displacement parameters (\AA^2) of $\text{LaCu}_{0.12(1)}\text{AsSe}$ in As split sites model (U_{22} is equal to U_{11}).

atom	site	x	y	z	U_{11}	U_{33}	U_{eq}
La	$2c$	0.25	0.25	0.71871(6)	0.0086(2)	0.0180(3)	0.0117(2)
Cu	$2c$	0.25	0.25	0.104(2)			0.01
As	$8g$	0.286(2)	0.714(2)	0	0.033(3)	0.0127(5)	0.026(2)
Se	$2c$	0.25	0.25	0.3704(1)	0.0087(3)	0.0120(4)	0.0100(2)

The bond distances between the As atoms vary from 2.51 Å to 2.97 Å because of the split sites. Another consequence is the splitting of the four Cu-As distances of 2.28 Å of the undistorted model into distances of 2.14 Å and 2.42 Å of split sites model, the former being too short in comparison with the single bond radii. Based on this, we tried to generate a hypothetical ordered model (Fig. 5.9). Evidently a large (hypothetical) supercell is required for any such model.

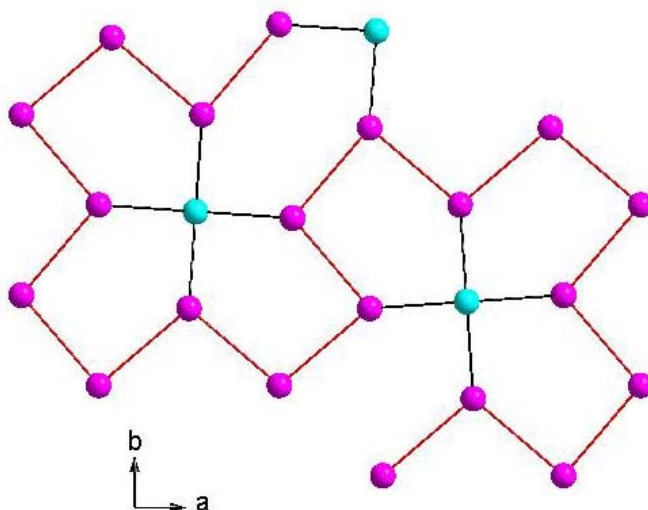


Fig. 5.9 View of a possible ordered As layer with the surrounding Cu atoms along the *c* axis (pink: As atoms; blue: Cu atoms).

Because the single crystal structure solution indicated only around 10% Cu inserted between La and As layers, $\text{LaCu}_{0.1}\text{AsSe}$ was prepared and the Seebeck coefficient was measured, as shown in Fig. 5.10. It has values between $-166 \mu\text{V/K}$ at 300 K and $-261 \mu\text{V/K}$ at 550 K, showing semiconductivity, which also implies the distortion of As square nets.

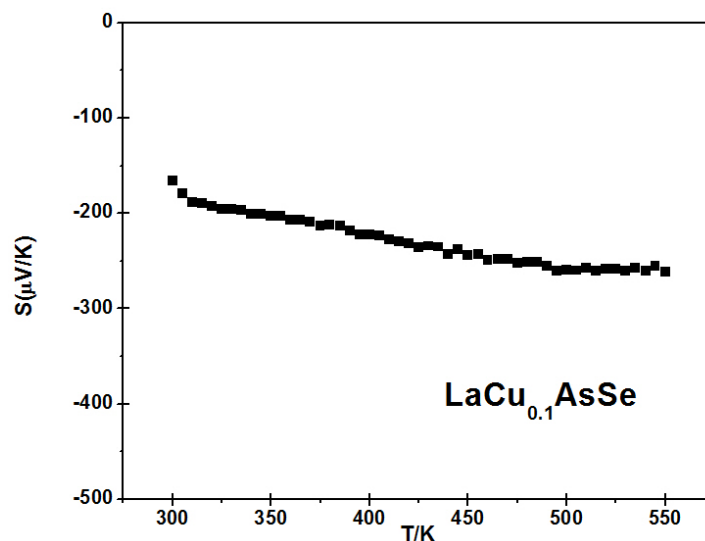


Fig. 5.10 Seebeck coefficient of $\text{LaCu}_{0.1}\text{AsSe}$.

Since Ni has a similar radius to Cu,¹⁴⁷ the synthesis of $\text{LaNi}_{0.1}\text{AsSe}$ and $\text{LaNi}_{0.2}\text{AsSe}$ was also tried. However, EDX detected very low Ni content in $\text{LaNi}_{0.2}\text{AsSe}$, around 0.5 At%, far less than the target 6.25 At% (At% stands for atomic percentage). Therefore we do not believe that Ni atoms can enter the crystal structure of LaAsSe .

LaAsTe , containing As-As single bonds (2.635Å) was investigated previously.¹⁴⁸ In my work, Cu atoms were added to attempt to prepare $\text{LaCu}_{0.2}\text{AsTe}$. Black needle-shape crystals were produced and analyzed. Single crystal data demonstrates they are only LaAsTe with the same structure as Huang *et al* reported,¹⁴⁸ which indicates Cu atoms are not involved in the formation of the crystal structure.

6 Conclusions

There are very few thermoelectric materials with promising ZT values for high temperature applications. Two types (n -type and p -type) of thermoelectric materials, variants of Mo_3Sb_7 and Re_3As_7 , were investigated and optimized for high temperature applications in this thesis. Both of them were metallic and were changed to degenerate semiconductors by altering the number of valence electrons.

In $\text{Mo}_3\text{Sb}_{7-x}\text{Te}_x$ compounds, the best ratio of Sb/Te was 5.4/1.6. Enhanced ZT values can be further achieved by addition of Fe and Ni at the right concentrations. Electronic structure calculations indicated adding Fe partly depopulated the valence band while Ni did not change the electron count.¹¹⁵ After examining various transition metal atoms (Mn, Fe, Co and Ni), $\text{Fe}_{0.05}\text{Mo}_3\text{Sb}_{5.4}\text{Te}_{1.6}$ outperformed the other $A_{0.05}\text{Mo}_3\text{Sb}_{5.4}\text{Te}_{1.6}$ compounds and gave rise to $ZT = 0.31$ at 673 K.¹¹⁴ However, the best thermoelectric properties achieved so far from this series of compounds was $\text{Ni}_{0.06}\text{Mo}_3\text{Sb}_{5.4}\text{Te}_{1.6}$, which had a $ZT = 0.93$ at 1023 K.¹¹⁵ Compared with another leading p -type thermoelectric material $\text{Yb}_{14}\text{MnSb}_{11}$ ($ZT = 0.8$ at 1000 K)⁴³ and the most widely used bulk p -type SiGe ($ZT = 0.5$ at 1100 K)¹³², $\text{Ni}_{0.06}\text{Mo}_3\text{Sb}_{5.4}\text{Te}_{1.6}$ is an absolutely promising candidate for high temperature thermoelectric application. Future work can be focused on the substitution of Mo with some electron-rich transition metal atoms, such as Re and Os, which can also increase the number of valence electrons, thereby changing the band structure near the Fermi level.

A variety of $\text{Re}_3(\text{E}, \text{As})_7$ ($\text{E} = \text{Si}, \text{Sn}, \text{Pb}$) compounds and $\text{Mo}_{0.1}\text{Re}_{2.9}\text{As}_7$ were prepared and studied. Electronic structure calculations predicted that the Sn substitution lowers the Fermi level into the band gap and adding Ni can further decrease the size of band

gap. The cell sizes of $\text{Re}_3\text{Sn}_x\text{As}_{7-x}$ compounds increased linearly with increasing Sn content. Rietveld refinement results showed that Sn demonstrated a site preference (12*d* or 16*f*) depending on the balance of size effect and electronegativity effect.¹³³ Further LMTO calculations based on five different models revealed that the occupancy of the 16*f* site can lead to semiconducting properties.¹⁴⁹ According to the physical property measurements, $\text{Re}_3\text{Sn}_{0.2}\text{As}_{6.8}$ had a comparable power factor value with $\text{Re}_3(\text{Ge,As})_7$.⁶⁴ Ni addition can increase the Seebeck coefficient more, while Co doping did not change anything. However, in the cases of $\text{Re}_3(\text{Si,As})_7$ and $\text{Re}_3(\text{Pb,As})_7$, transition metal atoms doping did not afford any improvement on Seebeck coefficient. The high temperature physical property measurements for hot-pressed samples are in progress at Clemson University.

The compounds with distorted square nets are of great interest because of their potential thermoelectric application. LaAsSe was synthesized and analyzed in this thesis. It adopted GdPS structure type, containing As cis–trans chains. Electronic structure calculation showed a band gap of 0.33 eV and physical property measurement proved a large Seebeck coefficient. A new compound $\text{LaCu}_{0.12(1)}\text{AsSe}$ was prepared and investigated in this thesis as well, which adopted a derivative structure of the ZrSiS type. A single crystal structure determination revealed As split sites. Accordingly, high Seebeck coefficient values – typical for semiconductors – were obtained. Future work can be focused on investigating the phase range and physical properties of LaCu_xAsSe in detail. Furthermore, we also have great interest in exploring new chalcogenides containing different transition metal atoms and distorted pnictogen square nets, such as $\text{Ln}T_x\text{AsS}$ and $\text{Ln}T_x\text{PS}$ (T = transition metal atoms).

New chalcogenides may be developed as thermoelectric materials by controlling the size of band gap and charge carrier concentration.

Appendix A

Tab. A.1 Crystallographic data for LaAsSe.

Formula	LaAsSe
Temperature (K)	298
Wavelength (Å)	1.54056
Space group	<i>Pnma</i>
Cell parameters	
<i>a</i> (Å)	5.8520(6)
<i>b</i> (Å)	5.8263(6)
<i>c</i> (Å)	17.954(2)
<i>V</i> (Å ³)	612.2(2)
No. of formula units per cell	8
Calculated density (g cm ⁻³)	6.127
Range in 2θ (deg)	10–100
R_p, R_{wp}	0.0303, 0.0463

Tab. A.2 Bond distances (Å) of LaAsSe.

Bonds type	No.	Bonding distance (Å)
La1–Se1	1	2.96(2)
La1–Se1	1	3.04(2)
La1–Se1	1	3.08(1)
La1–Se2	2	3.008(3)
La1–As	2	3.14(1)
La1–As	2	3.36(1)
La2–Se1	2	3.027(3)
La2–Se2	1	3.02(2)
La2–Se2	1	3.12(2)
La2–Se2	1	3.15(1)
La2–As	2	3.31(1)
La2–As	2	3.33(1)
As–As	1	2.501(7)
As–As	1	2.536(7)

Tab. A.3 Crystallographic data for LaCu_{0.12(1)}AsSe.

Empirical formula	LaCu _{0.12(1)} AsSe
Temperature (K)	296
Wavelength (Å)	0.71073
Space group	<i>P4/nmm</i>
Cell parameters	
<i>a</i> (Å)	4.1567(4)
<i>c</i> (Å)	8.9702(9)
<i>V</i> (Å ³)	154.99(3)
No. of formula units per cell	2
Calculated density (g cm⁻³)	6.430
Chemical formula weight	300.10
<i>R1, wR2</i>	0.0252, 0.0550

Tab. A.4 Comparison of selected bond distances (Å) of LaCu_{0.12(1)}AsSe in square net model and split site model.

Bonds type	No.	Square net model bond distance (Å)	No.	Split site model bond distance (Å)
La–Se	4	3.0462(5)	4	3.0461(3)
La–Se	1	3.124(2)	1	3.124(1)
La–As	4	3.2688(7)	4	3.179(5)/3.371(5)
Cu–As	4	2.282(7)	4	2.423(9)
As–As	4	2.9392(2)	4	2.51(1)/2.73(1)/2.94(1)/2.97(1)

Bibliography

1. J. Yang and T. Caillat, *Mat. Res. Bull.*, 2006, **31**, 224-229.
2. <http://green.autoblog.com/2009/03/09/bmws-continued-efficient-dynamics-plan-to-include-thermoelectri/>.
3. D. M. Rowe, *CRC Handbook of Thermoelectrics*, CRC Press, Boca Raton, FL, 1995.
4. A. F. Ioffe, *Semiconductor Thermoelements and Thermoelectric Cooling*, Infosearch, London, 1957.
5. W. Thomson, *Proc. Roy. Soc. Edinburgh*, 1851, 91-98.
6. <http://www.mpoweruk.com/semiconductors.htm>.
7. G. J. Snyder and E. S. Toberer, *Nat. Mater.*, 2008, **7**, 105-114.
8. <http://www.themotorreport.com.au/23040/bmw-and-nasa-teaming-up-to-devise-regenerative-exhaust-system/>.
9. <http://availabletechnologies.pnl.gov/technology.asp?id=85>.
10. <http://www2.jpl.nasa.gov/basics/rtg.gif>.
11. A. F. Ioffe, Academic Press, New York City, NY, 1960.
12. F. J. DiSalvo, *Science*, 1999, **285**, 703-706.
13. M. T. Tritt, *Mat. Res. Sci. Bull.*, 2006, **31**, 188-198.
14. D. Greig, *Electrons in metals and semiconductors*, McGraw-Hill, London, UK, 1969.
15. M. T. Tritt, *Mat. Res. Bull.*, 2006, **31**, 188-194.
16. G. A. Slack and V. G. Tsoukala, *J. Appl. Phys.*, 1994, **76**, 1665-1672.
17. B. C. Sales, D. Mandrus and R. K. Williams, *Science*, 1996, **272**, 1325-1328.
18. J. M. Worlock, *Phys. Rev.*, 1966, **147**, 636-643.
19. A. J. Minnich, M. S. Dresselhaus, Z. F. Ren and G. Chen, *Energy Environ. Sci.*, 2009, 466-479.
20. G. Zeng, J. E. Bowers, J. M. O. Zide, A. C. Gossard, W. Kim, S. Singer, A. Majumdar, R. Singh, Z. Bian, Y. Zhang and A. Shakouri, *Appl. Phys. Lett.*, 2006, **88**, 113502/1-113502/3.
21. G. A. Slack, *Solid State Physics*, Academic Press, New York, 1979.
22. G. S. Nolas, J. W. Sharp and H. J. Goldsmid, *Thermoelectrics - Basic Principles and New Materials Developments*, Springer, 2001.
23. D. M. Rowe, *Thermoelectrics Handbook: Macro to Nano*, CRC Press, Taylor & Francis Group, Boca Raton, FL, USA, 2006.
24. P. W. Zhu, L. X. Chen, X. Jia, M. H. A., G. Z. Ren, W. L. Guo, W. Zhang and G. T. Zou, *J. Phys. Condens. Matter*, 2002, **14**, 11269-11273.
25. P. F. P. Poudeu, J. D'Angelo, H. Kong, A. Downey, J. L. Short, R. Pcionek, T. P. Hogan, C. Uher and M. G. Kanatzidis, *J. Am. Chem. Soc.*, 2006, **128**, 14347-14355.
26. P. F. P. Poudeu, J. D'Angelo, A. Downey, J. L. Short, T. P. Hogan and M. G. Kanatzidis, *Angew. Chem.*, 2006, **45**, 3835-3839.

27. A. Gueguen, P. F. P. Poudeu, C.-P. Li, S. Moses, C. Uher, J. He, V. Dravid, K. M. Paraskevopoulos and M. G. Kanatzidis, *Chem. Mater.*, 2009, **21**, 1683-1694.
28. D.-Y. Chung, T. Hogan, P. Brazis, M. Rocci-Lane, C. Kannewurf, M. Bastea, C. Uher and M. G. Kanatzidis, *Science*, 2000, **287**, 1024-1027.
29. D.-Y. Chung, T. P. Hogan, M. Rocci-Lane, P. Brazis, J. R. Ireland, C. R. Kannewurf, M. Bastea, C. Uher and M. G. Kanatzidis, *J. Am. Chem. Soc.*, 2004, **126**, 6414-6428.
30. K. F. Hsu, S. Loo, F. Guo, W. Chen, J. S. Dyck, C. Uher, T. Hogan, E. K. Polychroniadis and M. G. Kanatzidis, *Science*, 2004, **303**, 818-821.
31. E. Quarez, K.-F. Hsu, R. Pcionek, N. Frangis, E. K. Polychroniadis and M. G. Kanatzidis, *J. Am. Chem. Soc.*, 2005, **127**, 9177-9190.
32. H. S. Dow, M. W. Oh, S. D. Park, B. S. Kim, B. K. Min, H. W. Lee and D. M. Wee, *J. Appl. Phys.*, 2009, **105**, 113703/1 -113703/5.
33. B. Wölfing, C. Kloc, J. Teubner and E. Bucher, *Phys. Rev. Lett.*, 2001, **86**, 4350-4353.
34. J. W. Sharp, B. C. Sales, D. G. Mandrus and B. C. Chakoumakos, *Appl. Phys. Lett.*, 1999, **74**, 3794-3796.
35. K. Kurosaki, A. Kosuga, H. Muta, M. Uno and S. Yamanaka, *Appl. Phys. Lett.*, 2005, **87**, 061919/1-061919/3.
36. G. S. Nolas, D. T. Morelli and T. M. Tritt, *Annu. Rev. Mat. Sci.*, 1999, **29**, 89-116.
37. C. Uher, *Semiconductors and Semimetals*, Academic Press, New York, 2000.
38. B. C. Sales, Elsevier Science, Amsterdam, 2002, p. 1.
39. G. S. Nolas, J. L. Cohn, G. A. Slack and S. B. Schujman, *Applied Physics Letters*, 1998, **73**, 178-180.
40. D. T. Morelli, G. P. Meisner, C. B., S. Hu and C. Uher, *Phys. Rev. B.*, 1997, **56**, 7376-7383.
41. G. S. Nolas, M. Kaeser, R. T. I. Littleton and T. M. Tritt, *Appl. Phys. Lett.*, 2000, **77**, 1855-1857.
42. J. S. Dyck, W. Chen, C. Uher, L. Chen, X. Tang and T. Hirai, *J. Appl. Phys.*, 2002, **91**, 3698-3705.
43. S. R. Brown, S. M. Kauzlarich, F. Gascoin and G. J. Snyder, *Chem. Mater.*, 2006, **18**, 1873-1877.
44. E. S. Toberer, S. R. Brown, T. Ikeda, S. M. Kauzlarich and G. Jeffrey Snyder, *Appl. Phys. Lett.*, 2008, **93**, 062110/1-062110/3.
45. S. R. Brown, E. S. Toberer, T. Ikeda, C. A. Cox, F. Gascoin, S. M. Kauzlarich and G. J. Snyder, *Chem. Mater.*, 2008, **20**, 3412-3419.
46. E. S. Toberer, C. A. Cox, S. R. Brown, T. Ikeda, A. F. May, S. M. Kauzlarich and G. J. Snyder, *Adv. Funct. Mater.*, 2008, **18**, 2795-2800.
47. C. A. Cox, E. S. Toberer, A. A. Levchenko, S. R. Brown, G. J. Snyder, A. Navrotsky and S. M. Kauzlarich, *Chem. Mater.*, 2009, **21**, 1354-1360.
48. R. Venkatasubramanian, E. Slivola, T. Colpitts and B. O'Quinn, *Nature*, 2001, **413**, 597-602.
49. T. C. Harman, P. J. Taylor, M. P. Walsh and B. E. LaForge, *Science*, 2002, **297**, 2229-2232.

50. A. I. Hochbaum, R. Chen, R. D. Delgado, W. Liang, E. C. Garnett, M. Najarian, A. Majumdar and P. Yang, *Nature*, 2008, **451**, 163-167.
51. A. I. Boukai, Y. Bunimovich, J. Tahir-Kheli, J.-K. Yu, W. A. I. Goddard and J. R. Heath, *Nature*, 2008, **451**, 168-171.
52. M. S. Dresselhaus, G. Chen, M. Y. Tang, R. Yang, H. Lee, D. Wang, Z. Ren, J.-P. Fleurial and P. Gogna, *Adv. Mater.*, 2007, **19**, 1043-1053.
53. L. E. Bell, *Science*, 2008, **321**, 1457-1461.
54. L. D. Hicks and M. S. Dresselhaus, *Phys. Rev. B*, 1993, **47**, 16631-16634.
55. J. R. Sootsman, R. J. Pcionek, H. Kong, C. Uher and M. G. Kanatzidis, *Chem. Mater.*, 2006, **18**, 4993-4995.
56. J. Androulakis, C.-H. Lin, H.-J. Kong, C. Uher, C.-I. Wu, T. Hogan, B. A. Cook, T. Caillat, K. M. Paraskevopoulos and M. G. Kanatzidis, *J. Am. Chem. Soc.*, 2007, **129**, 9780-9788.
57. B. Poudel, Q. Hao, Y. Ma, Y. Lan, A. Minnich, B. Yu, X. Yan, D. Wang, A. Muto, D. Vashaee, X. Chen, J. Liu, M. S. Dresselhaus, G. Chen and Z. F. Ren, *Science*, 2008, **320**, 634-638.
58. Y. Ma, Q. Hao, B. Poudel, Y. Lan, B. Yu, D. Wang, G. Chen and Z. Ren, *Nano. Lett.*, 2008, **8**, 2580-2584.
59. X. W. Wang, H. Lee, Y. C. Lan, G. H. Zhu, G. Joshi, D. Z. Wang, J. Yang, A. J. Muto, M. Y. Tang, J. Klatsky, S. Song, M. S. Dresselhaus, G. Chen and Z. F. Ren, *Applied Physics Letters*, 2008, **93**, 193121/1-193121/3.
60. G. Joshi, H. Lee, Y. Lan, X. Wang, G. Zhu, D. Wang, R. W. Gould, D. C. Cuff, M. Y. Tang, M. S. Dresselhaus, G. Chen and Z. Ren, *Nano. Lett.*, 2008, **8**, 4670-4674.
61. U. Häussermann, M. Elding-Ponten, C. Svensson and S. Lidin, *Chem. Eur. J.*, 1998, **4**, 1007-1015.
62. E. Dashjav, A. Szczepienowska and H. Kleinke, *J. Mater. Chem.*, 2002, **12**, 345-349.
63. N. Soheilnia, E. Dashjav and H. Kleinke, *Can. J. Chem.*, 2003, **81**, 1157-1163.
64. N. Soheilnia, H. Xu, H. Zhang, T. M. Tritt, I. Swainson and H. Kleinke, *Chem. Mater.*, 2007, **19**, 4063-4068.
65. W. Tremel and R. Hoffmann, *J. Am. Chem. Soc.*, 1987, **109**, 124-140.
66. F. Q. Huang, C. Flaschenriem, P. Brazis, C. R. Kannewurf and J. A. Ibers, *Inorg. Chem.*, 2003, **42**, 3194-3198.
67. S. R. Elliott, *The Physics and Chemistry of Solids*, John Wiley & Sons Ltd, 1998.
68. F. S. Pettit, Randklev, E. H., Felten, E. J., *J. Am. Cer. Soc.*, 1966, **49**, 199-203.
69. M. Granahan, H. M., W. Schulze and R. E. Newnham, *J. Am. Ceram. Soc.*, 1981, **64**, C-68-C-69.
70. R. H. Arendt, Z. H. Rosolowski and J. W. Szymaszek, *Mater. Res. Bull.*, 1979, **14**, 703-709.
71. R. H. Arendt, *J. Solid State Chem.*, 1973, **8**, 339-347.
72. M. G. Kanatzidis, R. Pöttgen and W. Jeitschko, *Angew. Chem. Int. Ed.*, 2005, **44**, 6996-7023.
73. Y. Z. Zheng and M. L. Zhang, *Mater. Lett.*, 2007, **61**, 3967-3969.

74. C. C. Chiu, C. C. Li and S. B. Desu, *J. Am. Ceram. Soc.*, 1991, **74**, 38-41.
75. K. H. Yoon, Y. S. Cho, D. H. Lee and D. H. Kang, *J. Am. Ceram. Soc.*, 2005, **76**, 1373-1376.
76. H. W. Ha, K. H. Jeong and K. Kim, *J. Power Sourc.*, 2006, **161**, 606-611.
77. J. F. Ni, H. H. Zhou, J. T. Chen and X. X. Zhang, *Mater. Lett.*, 2007, **61**, 1260-1264.
78. L. Wen, Q. Lu and G. X. Xu, *Electrochim Acta*, 2006, **51**, 4388-4392.
79. D. G. Porob and P. A. Maggard, *Mat. Res. Bull.*, 2006, **41**, 1513-1519.
80. C.-H. Han, Y.-S. Hong, C. M. Park and K. Keon, *J. Power Sourc.*, 2001, **92**, 95-101.
81. P. C. Canfield and Z. Fisk, *Philos. Mag.*, 1992, **65**, 1117-1123.
82. D. T. Morelli, P. C. Canfield and P. Drymiotis, *Phys. Rev. B*, 1996, **53**, 12896-12901.
83. W. R. Wilcox, *Chemical vapor transport, secondary nucleation, and mass transfer in crystal growth*, M. Dekker, New York, 1976.
84. P. Hagemuller, *Preparative Methods in Solid State Chemistry*, Academic Press, New York and London, 1972.
85. C. Giacovazzo, H. L. Monaco, G. Artioli, D. Viterbo, G. Ferraris, G. Gilli, G. Zanotti and M. Catti, *Fundamentals of Crystallography*, Oxford University Press, Oxford and New York, 2002.
86. P. F. Weller, *Solid State Chemistry and Physics: an introduction*, Marcel Dekker Inc., New York, 1973.
87. W. L. Bragg, *Proc. Camb. Phil. Soc.*, 1913, **17**, 43-57.
88. M. F. C. Ladd and R. A. Palmer, *Structure Determination by X-ray Crystallography*, Plenum Press, New York and London, 1993.
89. L. E. Smart and E. A. Moore, *Solid State Chemistry An Introduction*, Taylor & Francis Group, Boca Raton, London, New York, Singapore, 2005.
90. A. L. Patterson, *Phys. Rev. Lett.*, 1934, **46**, 372-376.
91. J.-J. Rousseau, *Basic Crystallography*, John Wiley & Sons, Chichester, 1998.
92. G. M. Sheldrick, *SHELXTL: Version 5.12*, Siemens Analytical X-ray Systems, Madison, WI, 1995.
93. *SMART: Version 4*, Siemens Analytical X-ray Instruments Inc., Madison, WI, 1995.
94. *SAINT: Version 4*, Siemens Analytical X-ray Instruments Inc., Madison, WI, 1995.
95. A. R. West, *Solid State Chemistry and Its Applications*, John Wiley & Sons, Chichester, New York, brisbane, Toronto, Singapore, 1984.
96. G. M. Sheldrick, Siemens Analytical X-Ray Systems, Madison, WI, 1995.
97. H. M. Rietveld, *J. Appl. Cryst.*, 1969, **2**, 65-71.
98. G. Malmros and J. O. Thomas, *J. Appl. Cryst.*, 1977, **10**, 7-11.
99. L. B. McCusker, R. B. von Dreele, D. E. Cox, D. Louër and P. Scardi, *J. Appl. Cryst.*, 1999, **32**, 36-50.
100. L. C. Larson and R. B. von Dreele, LANSCE, MSH805, Los Alamos National Laboratory, NM 87545, USA, 1995.

101. A. C. Larson and R. B. von Dreele, Los Alamos National Laboratory: Los Alamos, NM, 2000.
102. B. H. Toby, *J. Appl. Crystallogr.*, 2001, **34**, 210-213.
103. U. Mizutani, *Introduction to the Electron Theory of Metals*, Cambridge University Press, 2001.
104. O. K. Anderson, *Phys. Rev. B*, 1975, **12**, 3060-3083.
105. H. L. Skriver, *The LMTO Method*, Springer, Berlin, Germany, 1984.
106. J. C. Slater, *Phys. Rev.*, 1937, **51**, 846-851.
107. P. Hohenberg and W. Kohn, *Phys. Rev.*, 1964, **136**, B864-B871.
108. W. Kohn and L. J. Sham, *Phys. Rev.*, 1965, **140**, A1133-A1138.
109. M. Springborg, *Methods of Electronic-structure Calculations: From Molecules to Solids*, John Wiley & Sons, LTD, 2000.
110. A. R. West, *Basic Solid State Chemistry (Second Edition)*, John Wiley & Sons, LTD, Chichester, New York, Weinheim, Brisbane, Singapore, Toronto, 1999.
111. W. J. Parker, R. J. Jenkins, C. P. Butler and G. L. Abbott, *J. Appl. Phys.*, 1961, **32**, 1679-1684.
112. A. T. Petit and P. L. Dulong, *Annal. Chim. Phys.*, 1819, **10**, 395-413.
113. J. Blumm and E. Kaisersberger, *J. Therm. Anal. and Calorimetry*, 2001, **64**, 385-391.
114. H. Xu, K. M. Kleinke, T. Holgate, D. Rossouw, G. Botton, T. M. Tritt and H. Kleinke, *J. Alloys Comp.*, 2010, **504**, 314-319.
115. H. Xu, K. M. Kleinke, T. Holgate, H. Zhang, Z. Su, T. M. Tritt and H. Kleinke, *J. Appl. Phys.*, 2009, **105**, 053703/1-053703/5.
116. F. Jellinek and H. Hahn, *Naturwiss.*, 1962, **49**, 103.
117. R. Ceolin, N. Rodier and P. Khodadad, *J. Less-Comm. Met.*, 1977, **53**, 137-140.
118. C. Candolfi, B. Lenoir, A. Dauscher, J. Tobola, S. J. Clarke and R. I. Smith, *Chem. Mater.*, 2008, **20**, 6556-6561.
119. H. Zhang, J. He, B. Zhang, Z. Su, T. M. Tritt, N. Soheilnia and H. Kleinke, *J. Electron. Mater.*, 2007, **36**, 727-731.
120. O. K. Andersen, *Phys. Rev. B*, 1975, **12**, 3060-3083.
121. L. Hedin and B. I. Lundqvist, *J. Phys. C*, 1971, **4**, 2064-2083.
122. J. Xu and H. Kleinke, *J. Comput. Chem.*, 2008, **29**, 2134-2143.
123. P. Blaha, K. Schwarz, G. K. H. Madsen, D. Kvasnicka and J. Luitz, *WIEN2k, An Augmented Plane Wave + Local Orbitals Program for Calculating Crystal Properties*, Techn. University, Wien, Austria, 2001.
124. W. R. L. Lambrecht and O. K. Andersen, *Phys. Rev. B*, 1986, **34**, 2439-2449.
125. P. E. Blochl, O. Jepsen and O. K. Andersen, *Phys. Rev. B*, 1994, **49**, 16223-16233.
126. F. Gascoin, J. Rasmussen and G. J. Snyder, *J. Alloys Compd.*, 2007, **427**, 324-329.
127. C. Candolfi, B. Lenoir, A. Dauscher, E. Guilmeau, J. Hejtmánek, J. Tobola, B. Wiendlocha and S. Kaprzyk, *Phys. Rev. B*, 2009, **79**, 035114/1-035114/6.

128. N. F. Mott and H. Jones, *The Theory of the Properties of Metals and Alloys*, Dover Publications, New York, NY, 1958.
129. P. Stadelmann, *JEMS - Java Electron Microscopy Software, version 2.0819W2005*, EPFL, Switzerland, 2001.
130. M. Zelinska, A. Assoud, C. Graf and H. Kleinke, *Inorg. Chem.*, 2010, **49**, 1090-1093.
131. P. Jensen, A. Kjekshus and T. Skansen, *Acta Chem Scand.*, 1966, **20**, 403-416.
132. C. B. Vining, W. Laskow, J. O. Hanson, R. R. Van der Beck and P. D. Gorsuch, *J. Appl. Phys.*, 1991, **69**, 4333-4340.
133. H. Xu, T. Holgate, J. He, Z. Su, T. M. Tritt and H. Kleinke, *J. Electron. Mater.*, 2009, **38**, 1030-1036.
134. L. Pauling, *The Nature of the Chemical Bond*, Cornell University Press, Ithaca, NY, 1948.
135. N. Soheilnia, J. Giraldi, A. Assoud, H. Zhang, T. M. Tritt and H. Kleinke, *J. Alloys Compd.*, 2008, **448**, 148-152.
136. P. Sreeraj, D. Kurowski, R.-D. Hoffmann, Z. Wu and R. Poettgen, *J. Solid State Chem.*, 2005, **178**, 3420-3425.
137. M. Schlüter, U. Häussermann, B. Heying and R. Pöttgen, *J. Solid State Chem.*, 2003, **173**, 418-424.
138. L. S. Andrukhiv, L. A. Lysenko, Y. P. Yarmolyuk and E. I. Gladyshevskii, *Dopov. Akad. nauk Ukr. RSR A*, 1975, 645-648.
139. P. C. Donohue and P. E. Bierstedt, *Inorg. Chem.*, 1969, **8**, 2690-2694.
140. F. Hulliger, R. Schmelzger and D. Schwarzenbach, *J. Solid State Chem.*, 1977, **21**, 371-374.
141. D. A. Keszler and R. Hoffmann, *J. Am. Chem. Soc.*, 1987, **109**, 118-124.
142. Y. C. Wang, K. M. Poduska, R. Hoffmann and F. J. DiSalvo, *J. Alloys Compd.*, 2001, **314**, 132-139.
143. N. Soheilnia, K. M. Kleinke and H. Kleinke, *Chem. Mater.*, 2007, **19**, 1482-1488.
144. E. DiMasi, B. Foran, M. C. Aronson and S. Lee, *Phys. Rev. B*, 1996, **54**, 13587-13596.
145. A. Schlechte, R. Niewa, Y. Prots, W. Schnelle, M. Schmidt and R. Kniep, *Inorg. Chem.*, 2009, **48**, 2277-2284.
146. D. Schiferl and C. S. Barrett, *J. Appl. Cryst.*, 1969, **2**, 30-36.
147. J. C. Slater, *J. Chem. Phys.*, 1964, **41**, 3199-3204.
148. F. Q. Huang, P. Brazis, C. R. Kannewurf and J. A. Ibers, *Inorg. Chem.*, 2000, **39**, 3176-3180.
149. H. Xu, N. Soheilnia, T. M. Tritt and H. Kleinke, *Mat. Res. Soc. Proc.*, 2008, **1044**, 459-467.